Characterization of the adhesion of coatings by surface acoustic waves generated and detected by laser sources

Mustapha Baher

PhD Thesis
Submitted for the degree of Doctor of Philosophy from UNIVERSITÉ POLYTECHNIQUE HAUTS-DE-FRANCE And INSA HAUTS-DE-FRANCE

Speciality: Acoustics

Presented by: Mustapha BAHER

Doctoral school: École Doctorale Polytechnique Hauts-de-France (ED PHF)

Research team, Laboratory: TPIA Group, Institut d'Electronique de Microélectronique et de Nanotechnologie - IEMN UMR CNRS 8520, Site de Valenciennes

---

Characterization of the adhesion of coatings by surface acoustic waves generated and detected by laser sources

---

JURY

Jury President
Pr Gilles DESPAUX, Professor at Université de Montpellier

Reviewers
Pr Gilles DESPAUX, Professor at Université de Montpellier
Pr Nicolas WILKIE-CHANCELLIER, Professor at CY Cergy Paris Université, site de Neuville

Examiners
Dr Hossep ACHDJIAN, Associate Professor at INSA Centre Val de Loire

Thesis Director
Pr Frédéric JENOT, Professor at UPHF.

Thesis Co-Director
Pr Mohammadi OUAFTOUH, Professor at UPHF.

Co-supervisor
Dr Meriem CHRIFI ALAOUI, Associate Professor at UPHF.

Date and place of the defense
Tuesday 15, October 2024, at IEMN, site de Valenciennes.

Thèse de doctorat
Pour obtenir le grade de Docteur de l'UNIVERSITÉ POLYTECHNIQUE HAUTS-DE-FRANCE et de l'INSA HAUTS-DE-FRANCE

Spécialité : Acoustique

Présentée et soutenue par Mustapha BAHER

Ecole doctorale : École Doctorale Polytechnique Hauts-de-France (ED PHF n°635)

Equipe de recherche : Equipe TPIA, Institut d'Electronique de Microélectronique et de Nanotechnologie - IEMN UMR CNRS 8520, Site de Valenciennes

---

Caractérisation de l'adhérence des revêtements par ondes acoustiques de surface générées et détectées par sources laser

---

JURY

Président de jury
Pr Gilles DESPAUX, Professeur à l'Université de Montpellier

Rapporteurs
Pr Gilles DESPAUX, Professeur à l'Université de Montpellier
Pr Nicolas WILKIE-CHANCELLIER, Professeur à CY Cergy Paris Université, site de Neuville

Examinateurs
Dr Hossep ACHDJIAN, Maître de Conférences à l'INSA Centre Val de Loire

Directeur de thèse
Pr Frédéric JENOT, Professeur à l'UPHF.

Co-directeur de thèse
Pr Mohammadi OUAFTOUH, Professeur à l'UPHF.

Co-encadrant
Dr Meriem CHRIFI ALAOUI, Maître de Conférences à l'UPHF.

Date et lieu de la soutenance
Le Mardi 15, Octobre 2024, à l'IEMN, site de Valenciennes.

Acknowledgements

My profound gratitude to Professor Gilles Despaux and Professor Nicolas Wilkie-Chancellier for honoring me by serving as the rapporteurs of this work. I would also like to sincerely thank Doctor Hossep Achdjian, who accepted to be part of the jury and for his invaluable feedback on this work.

This doctoral thesis was done at the Institute of Electronics, Microelectronics, and Nanotechnology (IEMN) site de Valenciennes, Université Polytechnique Hauts-de-France, CNRS, Université de Lille, UMR 8520.

I would like to express my deepest gratitude to all those who have supported me throughout the journey of my Ph.D. This thesis would not have been possible without the guidance, support, and patience of many individuals.

First, I would like to thank my supervisor, Dr. Meriem Chrifi Alaoui, for her guidance in refining my research direction. I am also appreciative to my thesis directors, Prof. Frédéric Jenot and Prof. Mohammadi Ouaftouh, for offering me the opportunity to advance my career, as well as for providing their expertise and advice not only in the thesis subject but also in the field of research. I am deeply grateful for their gracious hospitality in welcoming me into the laboratory and allowing me to undertake this project. I also appreciate Mr. Frédéric Rivart for his availability and assistance whenever needed.

My warm thanks to Prof. Stephan Guerin for his extraordinary efforts as the director of the Physics, Photonics, and Nanotechnology (PPN) master's program at Université Bourgogne Franche-Comté, Dijon. Completing this program marked the first step in my academic journey. I also owe a debt of gratitude to Prof. Vincent Boudon and Prof. Cyril Richard for their invaluable guidance during my Master's internship. Their deep expertise and insights into theoretical physics have been instrumental in shaping my research career. It is with great respect and appreciation that I acknowledge these professors for their pivotal role at this stage.

I particularly express my warm gratitude to my friend Victory Elias for all his moral support. Our coffee breaks and the numerous, enriching discussions across various topics have been a source of strength and inspiration for me. I am equally grateful to my doctoral twin Samir Al-Mohammed, who started this journey with me. Sharing both our successes and challenges has been encouraging me.

I was lucky enough to have crossed paths with remarkable friends during this journey, especially Rachelle Al-Hajj, Majd Ghazaleh, Yara Bayssari, Wissam Alaji, Mahdi Saab, Zaher Bitar, Charbel Semaan, Ali Al-Mazbouh, Halim Wehbe, Amr Hecham, Maha Karam, Elissa Akiki, Abbas Hamade, Mohammad Masarra, Ahmad Jaber, Mohammad Akil, Hassan Al-Husseini, Marwa Sawan, and Abbas Salhab. Each one of them has contributed to this experience in a unique way.

I would also like to mention my friends and cousins: Afif Shoughri, Hussein Baher, Mohammed Baher, Mohammad Ghadboun, Fatima Dayekh, Ali Obied, Ahmad Youssef, Hassan Nasser, Ali Yaakoub, Rida Yaakoub, Haidar Maluelein, Fadel Saleh, and Jad Ezzedine. Our connection despite the distance has meant a great deal to me. The thought of reuniting with them fills me with anticipation and joy, and I cherish the hope that our paths will cross again soon.

My final thoughts are with my family: my lovely mother, Hala Baher, and my supportive father, Imad Baher, along with my sisters, Sarah, Lamis, Yusra, and Assil, with a heartfelt "thank you" to my fiancée, Taghrid, for her standing beside me during all the difficult moments. I also extend my love to my relatives and family members in Germany: Hussein, Batoul, Ali, and Hassan.

Finally, I would like to dedicate this thesis to my dear friend and twin brother in spirit, Mohammed Darwish, who tragically could not witness the ending of my academic journey. Despite his unexpected departure during this period, he was always there encouraging me. Rest in peace.

"Pain and suffering are always inevitable for a large intelligence and a deep heart. The really great men must, I think, have great sadness on earth."

– Fyodor Dostoevsky

Contents

List of Figures

List of Tables

Acronyms

2DFFT two-dimensional Fourier transform 93

Al Aluminum 24

AOM Acousto-Optic Modulator 27

Au Gold 66

BS Beam Splitter 27

CO_2 Carbon Dioxide 23

Cu Copper 118

CVD Chemical Vapor Deposition 5

CW continuous-wave 21

DC Direct Current 126

DT Destructive Testing 13

EA Electro-Adhesion 20

FEM Finite Element Method 84

FWHM full-width half maximum 87

LaSAT Laser Shock Adhesion Test 19

MAE Mean Absolute Error 137

Nd:YAG Neodymium-doped Yttrium Aluminum Garnet 23

NDT Non-Destructive Testing 14

PBS Polarization Beam Splitter 27

PML Perfectly Matched Layer 86

PVC Polyvinyl Chloride 35

PVD Physical Vapor Deposition 5

SAW Surface Acoustic Wave 4

SCOE surface center of expansion 87

Si Silicon 68

SiO_2 Fused Quartz 66

W Tungsten 69

ZnO Zinc Oxide 68

General Introduction

Studying thin films and their properties is important in nanotechnology due to their applications in modern technologies. Some films are deposited on substrates to enhance material strength and resistance to environmental factors such as corrosion and mechanical stresses. This thesis aims to characterize the adhesion pattern generated from an electric field source and the interaction of surface acoustic waves with different adhesion levels generated and detected by Laser-Ultrasonics as a non-destructive non-contact testing method.

Adhesion refers to the capability of different materials to bond at their interfaces. The adhesion quality of films to the substrate is an important factor that improves the durability of the devices. Our study employs Laser-Ultrasonics to characterize the adhesion quality of a polyvinyl chloride film adhered to an aluminum substrate. When using testing methods that involve elastic waves, it is necessary to maintain a uniform thickness of the deposited layer due to the sensitivity of these waves to the layer thickness variation. Therefore, the intermediate adhesive layer is avoided in this work.

Many theories describe the adhesion phenomenon which can be controlled by specific parameters such as the temperature in diffusion, surface roughness in mechanical interlocking and voltage in electro-adhesion. This latter is one of the methods used in many applications through an electro-adhesive device made of electrode layers glued to the dielectric material. However, this could be challenging in testing structures using ultrasonics due to the elastic parameters of the electrode layer, its adhesive quality with the dielectric and its thickness that affects the elastic waves. Therefore, a non-contact Electro-Adhesion (EA) pad consisting of sharp tip electrodes is used and can create a potential difference between the tips and a conductor substrate. The electric field generated can

modify the adhesion between the dielectric layer and the substrate by controlling the voltage loaded to the electrodes.

Different adhesion levels are obtained using this EA device and the highest level is considered of a uniform adhesion strength according to the measurements. A frequency-doubled Nd:YAG pulsed laser is used to generate elastic waves and a Mach-Zehnder heterodyne interferometer detects the normal displacement on the substrate surface. Two configurations are considered for generating surface waves. The first one allows the surface wave to propagate along the interface, demonstrating the impact of the adhesion levels for a constant propagation distance. The second configuration enables the experimental acquisition of the structure dispersion curves by generating multiple surface waves at the interface, facilitated by the transparent PVC film.

The effect of the theoretical adhesion parameters is important to optimize the adhesion quality of coatings. Therefore, a program is developed to numerically solve the surface modes dispersion relation. Moreover, the finite element method is necessary for our study to simulate the wave propagation with theoretical expectations under varying adhesion conditions and is then modified to model the resulting adhesion levels obtained experimentally.

The first chapter introduces chemical and physical vapor deposition techniques, along with the theories of adhesion such as diffusion, chemical, mechanical interlocking, electrostatics, and Van der Waal's forces. Moreover, the differences between the destructive and non-destructive techniques in characterizing adhesion with the state of the art of adhesion characterization. Additionally, it explains the principles of generating elastic waves by laser pulse for linear sources and the interferometry mechanism for detecting the normal displacement signal. Finally, the elastic parameters of the materials used in the experiments are presented.

After that, the second chapter shows the derivation of the dispersion relation of surface waves in a multilayered structure. Indeed, it is necessary for adhesion strength estimation using ultrasounds through inverse problem solving. It begins with the theory of elasticity and progresses to the solutions for the propagation equations of bulk and surface acoustic waves in an isotropic medium. This chapter focuses particularly on deriving the dispersion relations for Lamb waves and Rayleigh

waves, considering the influence of adhesion between the thin film and the substrate. This theoretical model shows how variations in bonding strength affect the dispersion curves.

Then, the third chapter presents the finite element method developed to characterize the adhesion pattern and to analyze the propagation and interaction of surface acoustic waves across the film-substrate interface. The sensitivity of these waves to parameters such as film thickness and adhesion strength can be analyzed through the model. Indeed, it can approach different studies such as uniform and non-uniform adhesion interfaces, adhesion strength, thickness of the film and other material properties.

The last chapter introduces the experimental setup of Laser-Ultrasonics used in the experiment and discusses the challenges of generating different adhesion strengths from an electric field source. Different adhesion levels are generated and their patterns are observed. The dispersion curves of each adhesion level are obtained experimentally providing an analysis of the thin film behavior and its interaction with the surface wave. The adhesion level for which the film is fully adhered to the substrate is considered uniform and the inverse problem is solved to estimate the adhesion strength. Therefore, the adhesion parameters obtained are included in the finite element model to investigate the influence of the non-uniform adhesion interface on the propagation and the dispersion of surface acoustic waves.

Chapter I

Adhesion in thin film technology and its characterization methods

Introduction

The physical properties of solid-state materials change with their thickness. Thin films are considered when the thickness of the solid material is reduced to vary in the range of nanometers up to a few micrometers deposited on a relatively semi-infinite substrate. They are used to strengthen a structure and make it more resistant to corrosion or cracks. Thin films have already been used in semiconductor devices, multilayer capacitors, computer chips and other technologies [1]. The high sensitivity of thin films to external stresses makes them a useful applicant for sensors (temperature, pressure, chemical measurements...).

In this chapter, we will present, in the first part, different deposition techniques. In the second, we will discuss adhesion testing methods, focusing on ultrasonic methods and difficulties encountered in characterization of adhesion phenomena according to the state of the art. In the third, the mechanisms of Laser-Ultrasonics are explained with the principles of generating and detecting Surface Acoustic Wave (SAW). In the final part, we will show the physical characteristics of the materials needed for this study.

1 Thin film coating characteristics

Acquiring a better coating quality lies in the characterization of the parameters that are responsible for its high performance and lifetime prolong. This quality deals with thickness variations, porosities or inclusions created during deposition, thermomechanical stress defects presented in the sample at its creation (cracks, layer delaminations) as well as adhesion defects. Figure I.1, illustrates different types of defects for thin film deposition on a substrate.

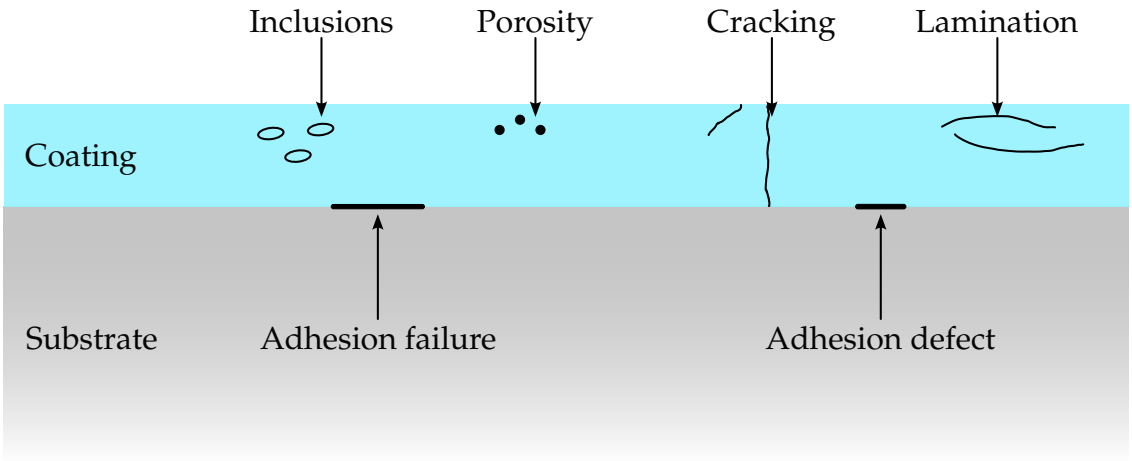

Figure I.1: A diagram illustrating the various types of defects that may be present in a thin layer [2].

Nanotechnology involves the use of nanoscale materials such as nanoparticles, nanotubes, nanoclusters and nanorobots. In thin film technology, thin layers of thickness in the scale of nanometers to micrometers, are deposited on a substrate to enhance their surface properties and to include modifications [3]. Two types of thin film deposition processes can be used:

- Physical Vapor Deposition (PVD): This method uses the condensation of a vaporized material typically created by an evaporation or a sputtering process. PVD processes can create a variety of thin film materials such as metals, dielectrics and semiconductors.

- Chemical Vapor Deposition (CVD): This method implies a chemical reaction between a reactant gas and a substrate surface. The reactant gas is created by the chemical decomposition of a specific material. CVD processes can also be used for different coating materials such as metals, dielectrics, semiconductors and polymers.

1.1 Coating deposition by PVD

Three main PVD methods are presented in the following:

a) Thermal evaporation

It is one of the main methods of vacuum evaporation. The material to be evaporated is placed in a vacuum chamber and heated. It is then deposited onto a substrate placed inside the vacuum chamber. The substrate may be heated to facilitate the deposition process. Thermal vapor deposition is a highly precise process that allows control over the thickness, composition and properties of the deposited material due to the vacuum medium at low pressure and the rectilinear trajectory of the particles of limited collisions. Figure I.2 illustrates the thermal evaporation technique, with two different sources leading to a flexible thickness control [2, 4, 5, 6].

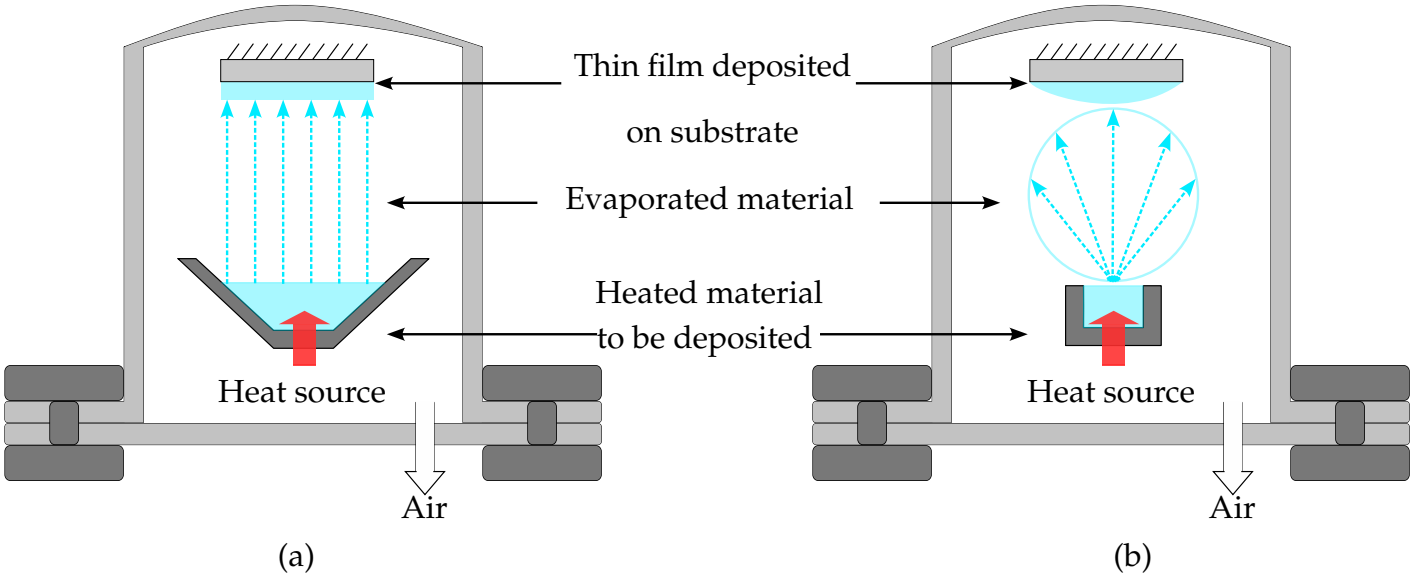

Figure I.2: Thermal evaporation in a vacuum chamber with an extended source (a) and a point source (b) [7].

b) Sputter deposition

In sputter deposition, the material to be vaporized is placed in a vacuum chamber and is subjected to a high-energy ion beam. The ions collide with the material, causing its vaporization and deposit onto a substrate.

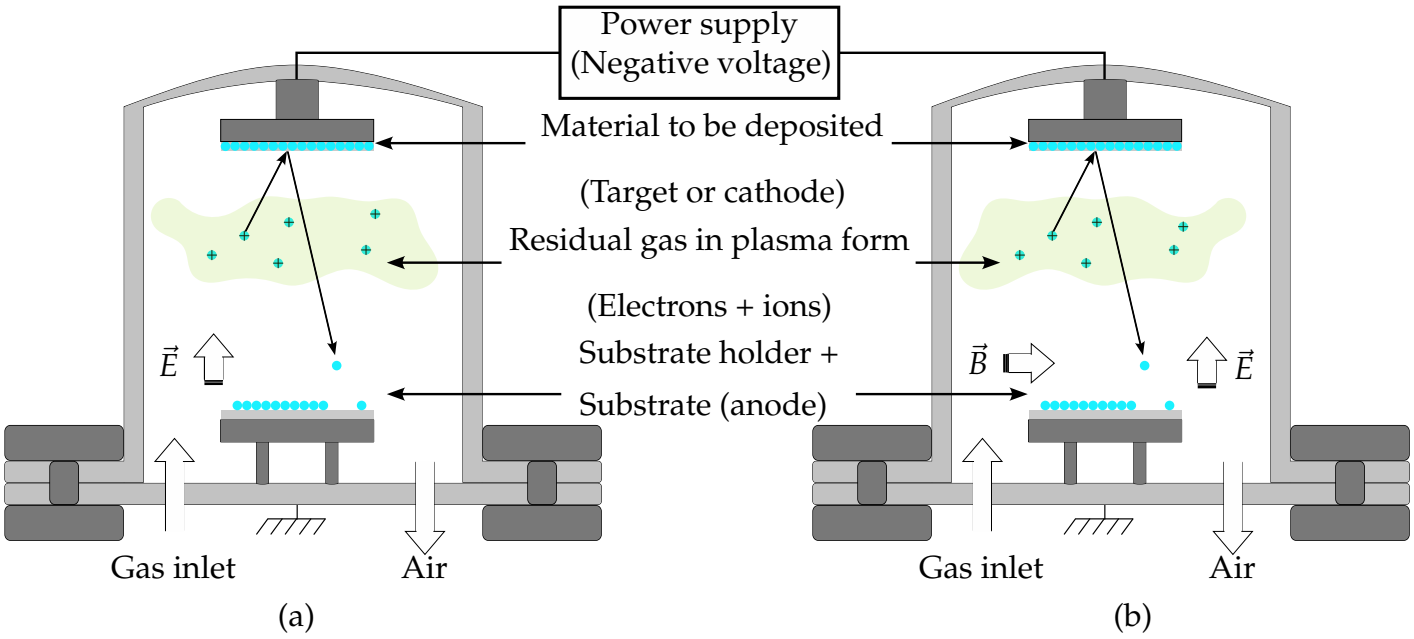

Figure I.3: Sputtering in a vacuum chamber with the process using electric field (a) and process using a magnetic field (b) [7].

The sputtering target is located on the cathode side of the system while the substrate is attached to the anode placed a few centimeters away from the cathode. To begin the process, the enclosure is vacuumed and a specific amount of argon gas is introduced. An electrical voltage is then applied between the two electrodes, as shown in figure I.3 (a). If the voltage is strong enough, the atmosphere becomes ionized and a glow discharge plasma is created. The positive ions in the residual gas are attracted to the negatively charged target and collide with it at high speeds. These collisions and transfer of momentum cause atoms from the target to be ejected, as well as secondary electrons that sustain the plasma. These ejected atoms then condense on nearby surfaces and form the deposit [4, 6, 8].

The magnetron process, presented in figure I.3 (b), has significantly improved this technique. Indeed, the addition of the magnetic field causes the path of the electrons near the cathode to lengthen, leading to a higher rate of ionization and a more efficient sputtering and deposition process. In this case, the plasma is also confined closer to the target, resulting in a lower substrate temperature than traditional sputtering [4].

c) Ionic deposition

The ionic deposition is often used in the production of electronic devices and other industrial applications. The material to be deposited is vaporized and ionized using heat or plasma. The ions are then attracted and deposited onto the substrate by an electric field. The process can be used to deposit a wide range of materials, including metals, alloys and ceramics implying a high level of purity and good adhesion to the substrate. Figure I.4 illustrates the system of this technique.

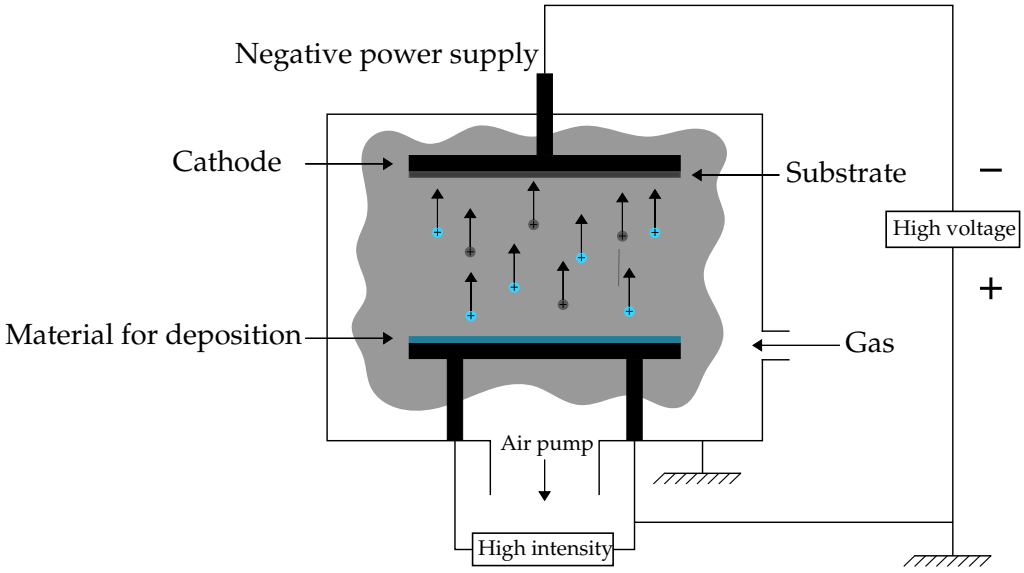

Figure I.4: System of ionic deposition [9].

During the ionic deposition process, the substrate is constantly bombarded with high-energy particles, which causes the deposited layer to be continually sputtered. This means that the deposition rate must be high enough to compensate for the sputtering and to allow the film's thickness to increase. An ion gun is often used to bombard the negatively polarized substrate, which becomes the target for positive ions from the plasma. If an evaporation source is placed near the system, the evaporated atoms will be deposited on the substrate. The source is typically bombarded with electrons to achieve a high evaporation rate [9, 10].

The energy from the bombardment during ionic deposition can cause modifications to the deposited layer. These changes can improve the adhesion of the layer to the substrate and its compactness through the density and the homogeneity of the layers.

1.2 Coating deposition by CVD

Chemical vapor deposition processes are classified into dynamic and static methodologies.

a) Static CVD process

The static method involves a closed reaction chamber where gases remain contained during the process. The component intended for coating is positioned inside a sealed chamber. It interacts with a combination of a source material and a particular reactive agent [11]. This combination undergoes a reaction when heated to a certain temperature, forming a gaseous compound essential for the coating procedure. This method is particularly effective for depositing protective layers of materials like chromium, aluminum or silicon onto steels and alloys, mainly to avoid corrosion and oxidation at high temperatures. It offers the advantage of treating several substrates at once, although it might not yield the highest purity in the resulting coated layer [4].

b) Dynamic CVD process

In the dynamic approach, the reaction chamber is kept open, allowing gases to be continuously evacuated and replaced. The component intended for coating is converted into a gaseous state and combined with a different gas, which acts as a catalyst for the chemical reaction. This reaction on the surface material can be initiated through various methods such as heating, gas ionization via electric discharge to create plasma, or exposure to light. As a result, a new layer forms on the surface as the reactant gases combine, the deposit material transits to a solid state and the catalyzing gas remains in its gaseous form. The resulting thin films are known for their strong adhesion, quick formation and exceptional purity. However, the high temperatures of this method can cause deformations in the sample and the process may involve the use of hazardous materials [4, 12].

1.3 Deposition methods comparison

Each technique presents its own set of benefits and complexity related to specific applications. CVD coatings are recognized for their good adhesion and purity. However, hazardous materials and high operational temperatures are required. Conversely, PVD involves less risk in terms of harmful materials and does not necessitate high temperatures but it may result in weaker adhesion between the coating and the substrate [4, 5]. This comparison is summarized in table I.1.

Characteristic	**Evaporation**	**Sputtering**	**Ion plating**	**CVD**
Thickness deposition rate	0.1 to 100 μm/h	0.01 to 0.1 μm/h	1 to 100 μm/h	0.1 to 100 μm/h
Porosity	Very low	Very low	Very low	Very low
Adherence	Moderate	Good	Very Good	Very Good
Coverage ability	Good to Low	Good	Good	Good
Deposited materials	Metals, alloys, ceramics	Metals, alloys, ceramics	Metals, alloys, ceramics	Metals, alloys, ceramics
Covered materials	Metals, alloys, plastics	Metals, alloys, plastics	Metals, alloys, plastics	Chemically & thermally resistant materials.
Deposition environment	10^{-1} to 10^{-7} Torr	10^{-1} to 10^{-3} Torr	10^{-3} to 10^{-5} Torr	$<$ atmospheric pressure
Treatment temperature	Low	100-150 °C	100-150 °C	600-1400 °C
Coating purity	Very high (if $<$ 10^{-6} Torr)	Increases with lower pressure	Gases used may be included with the coating	Generally very pure

Table I.1: Comparative overview of PVD and CVD deposition processes [4].

2 Adhesion theories and its characterization techniques

In thin film technology, adhesion consists in bonding two surfaces together. The film adhesion to the substrate is essential for ensuring the reliable performance of the device. Common techniques used to improve adhesion include chemical treatment of the substrate, chemical or physical surface modification of the film and the use of adhesion promoters and bonding agents.

2.1 Theories of adhesion

Adhesion is an interfacial phenomenon caused by inter-molecular interactions of dissimilar molecules at the adherend-adherate interface. When two materials adhere to each other, the thinner one is called the adherate (the film) and the thicker one is the adherend (the substrate) [13]. Adhesion phenomena are due to plenty of factors that can be described by several theories in physics and chemistry [14]:

a) Mechanical interlocking

This theory depends on the roughness of the substrate, more roughness degree gives more bonded area that leads to a better adhesion strength. However, the increase of roughness may lead to a weak adhesion due to the creation of some voids causing uncoated areas, hence this theory needs to have an intimated contact between the film and the substrate [14].

b) Diffusion

This method diffuses the adherate into the adherend by raising the temperature. Such method is mainly applied to polymeric adhering systems and not to rigid solids like metals or glass due to their high melting temperature condition [14].

c) Chemical adhesion

These adhering systems undergo a chemical reaction at the interface to form chemical bonds. According to Lewis's theory, a chemical bond involves sharing or transfer of electrons to attain stable electron configurations for the bonding atoms. If the electrons are transferred, the bond is ionic. If they are shared, the bond is covalent [14, 15].

d) Electrostatic adhesion

When two dissimilar conducting surfaces face each other at a very small distance, an electrostatic force is created by applying a potential difference between both surfaces and the system can be compared to a capacitor [14].

e) Van der Waals forces

The main characteristic differentiating these forces is the type of interaction that gives rise to them: Keesom forces result from the interaction between permanent dipoles, London dispersion forces arise from the fluctuating dipole moments of all atoms and molecules and Debye forces are the result of the interaction between induced and permanent dipoles [16].

- Keesom forces:

  Also known as Keesom interactions, they are attractive or repulsive forces that exist between molecules that have permanent dipoles. These forces are named after the Dutch physicist Willem Hendrik Keesom, who first described them in the early 20th century. Keesom forces are relatively weak compared to other intermolecular forces.

- Debye (permanent–induced dipoles) force:

  Also known as the Debye-Hückel force, it is an attractive or repulsive force that exists between charged particles in a solution. This force is the result of the interaction between the induced dipole moment of one particle and the permanent dipole moment of another one. It is named after the Dutch physicist Peter Debye, who first described it in the early 20th century. The

strength of the Debye force depends on the magnitude of the dipole moments of the interacting particles and the distance between them.

- London dispersion forces (fluctuating dipole–induced dipole interaction):

  These are attractive forces that exist between all atoms and molecules. They are the result of the fluctuating dipole moments that occur due to the movement of electrons. London dispersion forces are important because they are present in all types of matter. They are responsible for the behavior of non-polar molecules, which do not have a permanent dipole moment but can still experience London dispersion forces.

Adhesion characterization is the process of evaluating the strength and durability of the bond between two layers. It can be done through a variety of methods, either destructive or non-destructive. In the following sections, we will present both method types.

2.2 Adhesion evaluation by Destructive Testing (DT)

Destructive Testing (DT) techniques are methods that physically damage the samples. In adhesion evaluation, these techniques result in breaking the bond between two materials by applying a force to the bond until it fails and measuring this force. Examples mentioned below are found in [17]:

a) Scratching test

Scratching the surface of a material allows one to measure the force needed to cause the bond to fail, using a stylus to apply a load on the film while moving it relative to the substrate. The load on the stylus is gradually increased until the film is separated from the substrate. The load at which this separation occurs is referred to as the critical load and indicates the adhesion strength of the film.

b) Peeling test

It consists in peeling a material apart in a parallel direction to the surface and measuring the adhesive strength by adding a certain mass of water to a graduated cylinder connected to one side

of a balance. The other side of the balance has the tape or film being tested. As the mass of water is increased, the point at which the adhesive bond between the tape/film and the substrate fails is determined. This test is limited to measuring the adhesive strength of the tape or film, which must be stronger than the bond between the film and the substrate.

c) Pulling or tensile test

It consists in pulling a material apart in the perpendicular direction to the surface. It is a method of measuring adhesive strength by using cylindrical steel studs that are glued to the film while the sample is mounted under an electronic force gauge. This method is used as a way to control the applied force to measure the force that caused the failure.

2.3 Adhesion Non-Destructive Testing (NDT) using ultrasonic methods

In the context of adhesion characterization, Non-Destructive Testing (NDT) approaches focus on evaluating the quality of the bond between materials through indirect measurements. Many studies have reported the use of ultrasonics NDT to characterize various parameters associated with adhesion. Usually, these techniques use the following methods [18]:

a) Resonant-Ultrasound Spectroscopy

It is based on the measurement of the resonant frequency of a material. By measuring this frequency and comparing it to the material's known properties, it is possible to determine some mechanical properties such as elastic modulus and Poisson's ratio [19].

b) Reflection and transmission coefficients of bulk waves

The contact conditions at the interface greatly affect wave reflection and transmission between two materials. Hence, this is a good technique for measuring adhesion. However, it only allows for local testing of the samples and requires exact positioning of the transmitter-receiver pair.

Acoustic microscopy uses high-frequency ultrasonic transducers to direct bulk waves toward the material interface, where receivers are positioned to capture either reflected or transmitted waves, depending on the measurement setup [20, 21]. Reflection and transmission coefficients can be calculated by examining these waves' amplitude and phase characteristics. Similar measurements are made using laser-generated ultrasonic waves in Laser-Ultrasonics, providing detailed information about adhesion quality. High reflection coefficients could imply poor adhesion [22, 23].

c) Surface and guided waves propagation analysis

It is a crucial technique for adhesion measurements, as it allows the examination of relatively large areas. By analyzing the dispersion curves of guided or surface acoustic waves, which are sensitive to the properties of the material, it is possible to characterize the adhesion at the interface [5].

Indeed, all these previous ultrasonic methods are powerful in the characterization of adhesion. The basic principle behind ultrasonics is analyzing the frequency, amplitude and phase of the reflected or transmitted ultrasound waves that propagate through a material. For adhesion characterization, ultrasonics can be used to evaluate the strength of the bond between a film and a substrate, as well as the presence of defects at the interface. In this section, we will focus on the state-of-the-art techniques of ultrasonics and Laser-Ultrasonics for the characterization of adhesion.

2.4 State of the art of studying adhesion by ultrasonics

To characterize the adhesion between a coating and a substrate, either a transducer or a laser can be used to generate SAW that propagate along the surface of the film. The wave propagation is sensitive to the mechanical properties and the adhesion of the film to the substrate.

2.4.1 Ultrasonic waves generated and detected by piezoelectric transducers

According to the study of Puthillath and Rose, the Lamb modes would be a good determination for poor adhesion by detecting the large in-plane displacement at the interface [24]. In their experimental setup, the 18th mode of Lamb was found to be the most suitable. It was then generated and

observed after being passed through an area with various levels such as good adhesion, mediocre adhesion with the addition of Teflon and total detachment through the introduction of an air bubble. The weaker is the grip, the lower is the received wave's amplitude, as it more strongly attenuates the highest frequencies.

In a study conducted by Bourse et al. four different coating thicknesses were tested, each with a unique adhesion defect [21]. The roughness of the substrate was varied locally to create these defects. The "$V(z)$" method was used to determine the reflection and transmission coefficients of the longitudinal and shear waves by analyzing the acoustic signature. The reflection coefficient was calculated using the displacement jumps model, taking into consideration the angle of incidence and the wave frequency in order to determine the value of the tangential interface stiffness K_t (assuming the influence of the interface normal stiffness K_n was insignificant). The results were then verified through destructive indentation tests, which showed that the value of K_t was lower in cases of poor adhesion and that the quality of the interface was related to the roughness of the substrate.

In their evaluation of metallic thin film interface adhesion, Juarez et al. utilized picosecond acoustics [25]. They created fingerprints on various substrates and deposited layers of nickel through sputtering or evaporation. The fingerprints were considered as contaminants to the surface and were expected to result in weaker adhesion. The acoustic cartography revealed that the contaminated areas had higher reflection coefficients, which corresponded well with the shape of the fingerprints.

Choi et al. worked on evaluating the adhesion strength of a titanium layer on a silicon substrate using surface acoustic wave dispersion [26]. They used the Thomson-Haskell transfer matrix model to theoretically observe the influence of adhesion strength on the dispersion curves of surface acoustic waves depending on the tangential and normal stiffnesses K_t and K_n respectively. They had 5 different levels of adhesion strengths, modifying the DC power from 28.8 W to 144 W during the magnetron sputtering deposition. Scanning electron microscopy measured the error of the titanium uniform thickness that was about 4.5 % with respect to 600 nm. Ultra-high frequency scanning acoustic microscope by $V(z)$ method was employed to measure the SAW velocity of each sample and a scratch test was used to measure the critical load. Finally, the results satisfied the dispersion curves

according to the measured velocity values and then linked the K_n and K_t to the critical load.

2.4.2 Ultrasonic waves generated and detected by lasers

The study by Xiao et al. focuses on the adhesion of a thin film on a substrate system. They use a combination of laser-generated surface acoustic waves and piezoelectric transducers to detect the signals and obtain the dispersion curve of a Rayleigh mode [27, 28]. The results are then compared with theoretical calculations based on the Cohesive Zone Model, which determines the maximum stress applied to the interface before an adhesive failure occurs. The normal stiffness at the interface is expressed as $K_n = \frac{\sigma_m}{\delta_n}$, where σ_m is the maximum normal stress and δ_n the distance between the layer and the substrate. The results show that the adhesion value of the porous film is lower than that of the dense film and that the waves propagating on the porous film are slower and of lower amplitude.

Schneider et al. conducted research on the effect of adhesion on the propagation of surface acoustic waves in thin films of titanium nitride deposited on a steel substrate [29, 30]. To manipulate the adhesion of the films, the substrate was cleaned for varying durations of time prior to the film deposition by sputtering. Samples cleaned for a longer period were considered to have good adhesion, while the others were considered to have poor one, which was confirmed through destructive tests. The results showed that the phase velocity of the Rayleigh mode generated in the structure was slightly impacted by the cleaning time of the substrate, with longer cleaning time resulting in higher velocity, or a "stiffening" configuration. However, an increase in layer thickness had a greater effect on the dispersion curves, similar to increasing the substrate cleaning time. The authors attributed this to micro-defects within the film that affect its adhesion and, consequently, its Young's modulus. They also found that a shorter substrate cleaning time led to a lower Young's modulus.

The research conducted by Cho et al. investigated the quality impact of the weld joint between a steel sheet and a carbon steel sheet on the spread of Rayleigh modes in the structure [31]. To simulate various levels of adhesion, samples were created with varying weld quality. As it decreased (and thus the adhesion), the initial Rayleigh mode in the structure showed an increasing tendency

towards the Lamb mode in the steel sheet. The experimental results showed a trend consistent with the analytical model of displacement jumps when adhesion decreased.

In their study, Wu and Chen examined the effect of a separated zone in a copper plate–epoxy–aluminum block assembly on the surface and guided waves' propagation [32]. When the generation and detection are performed in the bonded zone, the waves measured correspond to the Rayleigh modes in the three-layer structure. They found that ignoring the thickness of the adhesive leads to a large discrepancy between the experimental and analytical dispersion curves, demonstrating the significant impact the glue thickness has on the propagation of surface acoustic waves. When the generation and detection took place in the separated zone, the signals corresponded to the Lamb waves (mode A_0) in the copper plate. By alternating between generating in a stuck zone and detecting in an unglued zone or vice versa, Wu and Chen obtained signals with group velocity dispersion curves between those of the Lamb modes in the copper layer and those of the Rayleigh modes in the copper-epoxy-aluminum structure. They then proposed a theoretical model to calculate the group speed of the wave, which is dependent on the path taken by the wave in the separated or glued zone. The predictions of the model align well with the experimental results.

In Bruno's thesis, the focus was on determining the features of the adhesive joint and the adhesion strength of a bonded structure by analyzing the Lamb modes with zero group velocity [33]. The findings suggest template–epoxy–aluminum assembly can be determined by analyzing the frequency shift of the zero-speed modes with an understanding of the mechanical properties of the adhesive, particularly its thickness profile. By doing so, the stiffnesses of K_n and K_t can be retrieved.

Zhang and Zhou determined the location of a complete separation, caused by a lack of bonding, in a lead-epoxy-steel structure by analyzing the magnitude of particle displacement caused by Lamb waves [34]. They noted that the amplitude of the detected displacement was higher when the wave travelled for an extended period over a detached portion of the sample.

Zhang, Li and Zhou, proposed the ultrasonic technique with pulse-echo mode for accurate detection of disbonds in multi-layer bonded structures [35]. The research involves analyzing the characteristics of Laser-Ultrasonics reflected waves and the interaction of the waves with disbonds in

adhesive bonds. The experiments conducted verify the theoretical results and Laser-Ultrasonics C-scans based on reflected shear waves were used to identify the profiles of disbonds. A quantitative method based on relative sensitivity was proposed to evaluate the sizes of disbonds and the results obtained were in good agreement with the actual values. The combination of Laser-Ultrasonics C-scans based on reflected shear waves and the quantitative method allows for on-line and accurate inspection of disbonds in multi-layer metal bonded composites.

The study of Kowalczyk et al. aimed to determine the correlation between the strength of adhesive joints made with additive technology and ultrasonic wave parameters [36]. The study suggests that additive manufacturing technologies offer cost-effective opportunities for manufacturing complex geometries and further research on ultrasonic wave propagation in adhesive joints with different properties would extend the database of results for assessing joint strength without damage.

Kanamori et al. used the Laser Shock Adhesion Test (LaSAT) to evaluate the adhesion strength and durability of a Ni-P coating on a carbon steel substrate [37]. The effects of post-heat treatment on adhesion were investigated. It was found that heat treatment improved hardness, adhesion strength and durability of the coating. The LaSAT was shown to be a useful method for quick measurement of adhesion durability and could shed light on quality control of surface coatings. Overall, the study suggests that LaSAT is a valuable tool for evaluating the adhesion of coatings and may be useful in developing better ones.

In her study, Fourez observed that as the laser's incident energy gradually increased, staying within the thermoelastic regime, the amplitude of the initial Rayleigh mode traveling on a weakly attached layer was lower than when the layer was strongly attached [4]. Additionally, the ablation threshold for the layer was lower in cases of poor adhesion. This was brought about by removing the chromium adhesion layer, which had a negligible thickness, located between a gold layer and silicon substrate when adhesion was strong.

In another study, Robin employed an Nd:YAG laser doubled in frequency to generate elastic waves and an interferometer to detect SAW [5]. He used three different patterns to apply Teflon molecules as an antiadhesive and found that a larger Teflon surface resulted in weaker adhesion.

The adhesion measurement was conducted using signal processing methods of Wigner-Ville distribution through the detection of dispersive Rayleigh waves at different adhesion levels.

In this Ph.D. we aim to study the Electro-Adhesion (EA) effect generated from a specific device using surface acoustic waves generated by an Nd:YAG laser doubled in frequency and detected by a Mach Zhender heterodyne interferometer. In the following section, the mechanism of the electro-adhesion is introduced.

2.5 Mechanism of electro-adhesive pads

Electro-adhesion is used to improve the adhesion quality between two materials [38]. A strong electric field is created between two electrodes within an EA pad when a high voltage, usually ranging from 1 to 6 kV, is applied to generate electrostatic forces that enhance the interface quality between both surfaces [39]. Figure I.5 illustrates the mechanism of the electro-adhesion.

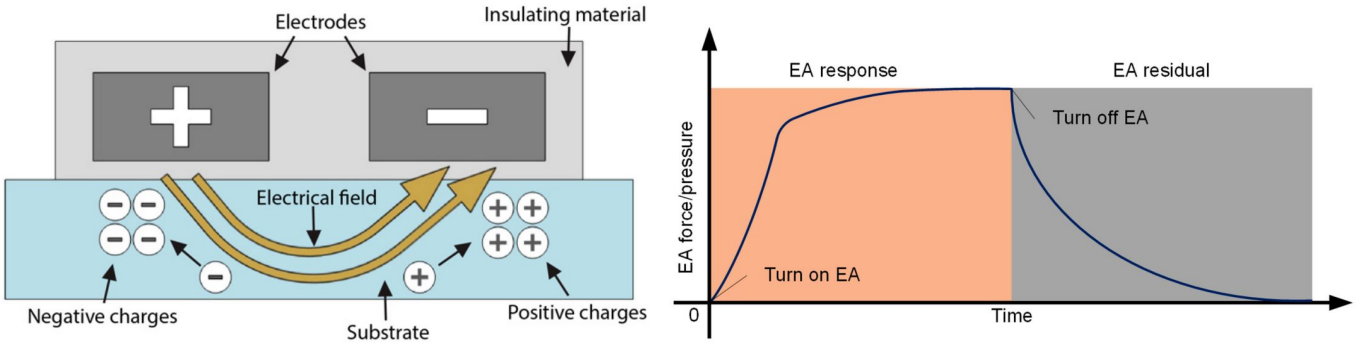

(a) (b)

Figure I.5: Schematic representation of EA pads mechanism (a) [40] and its corresponding response versus time (b) [39].

If an insulating surface enters the range of the applied electric field, it results in the orientation and electrical polarization of the insulating material, causing an attraction between the charges within the induced dipoles. The buildup of the force takes a finite amount of time, which depends on the electric properties of the material and the magnitude of the applied potential. Similarly, the decay of the adhesive force also takes a finite amount of time, ranging from seconds to hours, depending on

the type of materials and their interface conditions. This build-up and decay time can significantly impact the adhesion/de-adhesion cycle [41, 42].

2.6 Constraints of electro-adhesion

Although EA has many useful applications in robotics and electronics, it is important to note that there are limitations to consider for its measurement. These constraints may vary depending on the specific application and the electric characteristics of the material. However, these are the main challenges associated to this technology [39, 43, 44]:

- EA technology complexity and high cost, especially for large-scale applications,
- Inability to adhere to specific surfaces,
- Low and unstable adhesive force,
- High voltage requirements inducing health and safety risks if used on living organisms.

2.7 Aim of the thesis

Due to the sensitivity of the SAW to the thickness of the thin film, a non-contact EA device is used. Studies are performed on materials based on their EA response regarding the influence on surface acoustic wave propagation. The aim is to obtain several adhesion levels to evaluate the adhesion quality and model their impact on the Rayleigh wave by the finite element method.

The main objective of this work lies in the ability to obtain different adhesion levels using an electro-adhesion technique. Then, we aim to characterize these levels and their influence on the propagation of surface acoustic waves using Laser-Ultrasonics as a non-destructive testing technique.

3 Laser-Ultrasonics

The Laser-Ultrasonics method involves using a pulsed laser to generate acoustic waves and a continuous-wave (CW) laser interferometer for their detection. It can produce surface and bulk

waves in solid materials. The type of wave observed depends on the detection technique.

3.1 Pulsed laser mechanism

Various types of lasers have different amplifying mediums, including gaseous, solid-state and semiconductor lasers. Semiconductor lasers are unsuitable for ultrasonic applications due to their shorter coherence lengths, less well-collimated beams and lower power than gas or solid-state lasers [45]. Figure I.6 illustrates the basic operating principle of a laser amplifier.

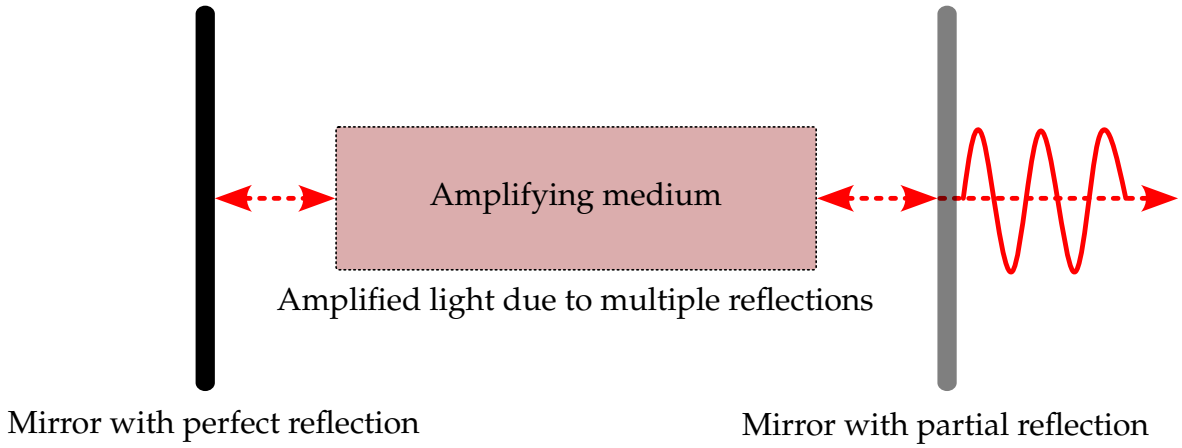

Figure I.6: Mechanism of the light amplification in a laser [46].

Photons generated from connected flashing lamps are redirected through a network of mirrors toward the amplifying medium, facilitating the pumping process. One of the mirrors is partially reflective, allowing the amplified light to escape as a laser beam. To generate this latter, the photons must be coherent and directed in the stimulating medium using the mirrors. As light bounces in random directions inside the cavity, the photons not aligned with the desired direction are absorbed by opaque walls [46].

Increasing the cavity losses to achieve a high laser oscillation initiation threshold generates a laser beam in the pulsed mode. This is accomplished by temporarily masking one of the cavity mirrors with an optical gate, allowing a significant population inversion without oscillation. When pumping reaches an adequate level, the gate opens and the laser beam initiates within a few passes through the cavity. This results in a powerful short pulse, typically in the order of tens of nanoseconds, enabling

high peak powers (exceeding 1 MW). The laser wavelength selection is based on the material's absorptivity at the intended frequency [4, 47]. Table I.2 presents some types of pulsed lasers.

Active Medium	Wavelengths (μm)	Pulse Duration	Repetition Rate (Hz)	Energy (J)
Argon-Fluor	0.193	5.5 ns – 25 ns	< 500	< 0.6
Ruby	0.694	15 ns – 3 ms	< 120	< 400
Krypton-Fluor	0.248	30 ps – 200 ns	< 500	< 1.5
CO_2	10.6	6 ns – 1100 μs	$< 10^4$	< 2200
Nd:YAG	1.06, 0.532*, 0.355*, 0.266*	30 ps – 20 ms	$< 5 \times 10^4$	< 150

*: Harmonic frequencies of the fundamental frequency.

Table I.2: Characteristics of pulsed lasers used for ultrasound generation [45].

Moreover, the laser pulse duration is a critical parameter in ultrasonic wave generation. The Neodymium-doped Yttrium Aluminum Garnet (Nd:YAG) and Carbon Dioxide (CO_2) lasers cover a broad frequency spectrum and are among the most commonly used sources. The next section will briefly explain the generation of acoustic waves by a laser pulse [47].

3.2 Generating acoustic waves by laser on solid structure

In the pulsed laser mode, energy can be emitted in a single pulse or as series of repetitive pulses. These short-duration laser pulses induce a localized temperature increase in the structure, leading to laser-material interaction phenomena responsible for generating elastic waves.

The absorption of laser radiation is limited to a certain thickness δ of the material called the skin depth, defined by equation 1.1. This thickness depends on the electrical and magnetic properties of the material as well as the wavelength of the generation laser [48].

$$\delta = \left(\frac{\lambda_0}{\pi \cdot \sigma \cdot c \cdot \mu} \right)^{1/2} \tag{1.1}$$

Where λ_0: Wavelength of the laser, σ: Electrical conductivity of the material, c: Speed of light in vacuum and μ: Magnetic permeability of the material. Equation 1.2 presents the absorption coefficient A [47, 48]:

$$A = \frac{I_a}{I_i} = 4 \cdot \left(\frac{\pi}{\sigma \cdot c \cdot \mu_0 \cdot \lambda_0} \right)^{1/2} \tag{1.2}$$

Where μ_0 is the magnetic permeability of the vacuum. The absorption coefficient, inversely proportional to the wavelength, is defined by the ratio of the absorbed intensity I_a over the incident optical intensity I_i. For an Aluminum (Al) sample and a laser wavelength of 532 nm, the skin depth is 3.4 nm and the absorption coefficient is around 8%.

An incident laser beam on a solid material generates ultrasonic waves either by the thermoelastic or the ablation regime. In general, each material has an ablation threshold corresponding to an absorbed power density depending on the material's characteristics and the duration of the generated laser pulse. The ablation threshold is defined by equation 1.3 [45, 47, 48].

$$I_S = \left(\frac{\pi \cdot K \cdot \rho \cdot C}{4\Delta t} \right)^{\frac{1}{2}} \cdot (T_v - T_i) \tag{1.3}$$

Where K: Thermal conductivity, ρ: Density, C: Specific heat capacity, Δt: Laser pulse duration, T_v and T_i: Vaporization and initial temperature. In the case of an aluminum sample and for a pulsed laser with a duration $\Delta t = 10$ ns, the ablation threshold is $I_S = 50\ \mathrm{MW/cm^2}$.

For an absorbed power density lower than the threshold value ($I_a < I_S$), ultrasonic waves are generated in the thermoelastic mode. This regime does not deform or affect the material and it allows more efficient generation of surface acoustic waves, as presented in figure I.7. In thermoelastic mode, laser radiation penetrates the skin depth of the material and produces localized heating which induces thermal expansion of the sample and the generation of stresses.

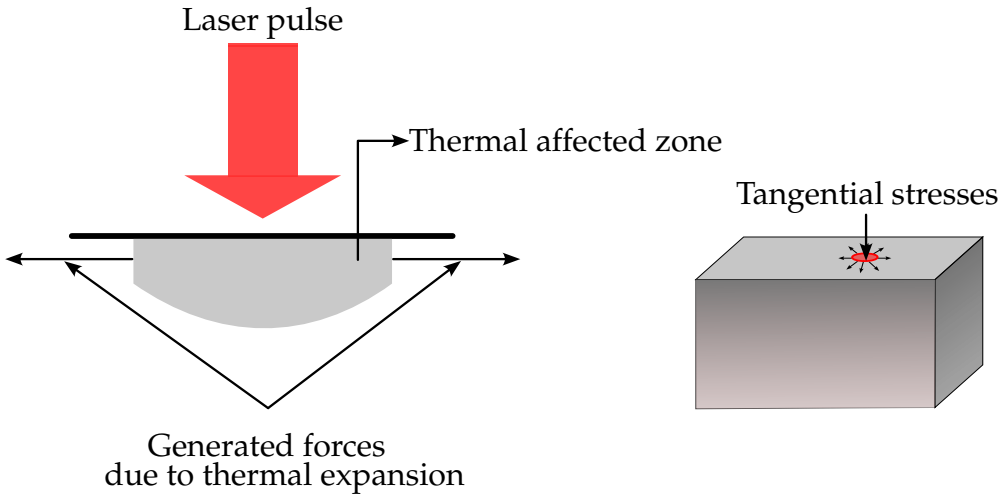

Figure I.7: Thermoelastic regime.

In contrast, for an absorbed power density greater than the threshold value ($I_a > I_S$), ultrasonic waves are generated in the ablation mode, at which some particles are vaporized and ejected from the material surface as illustrated in figure I.8.

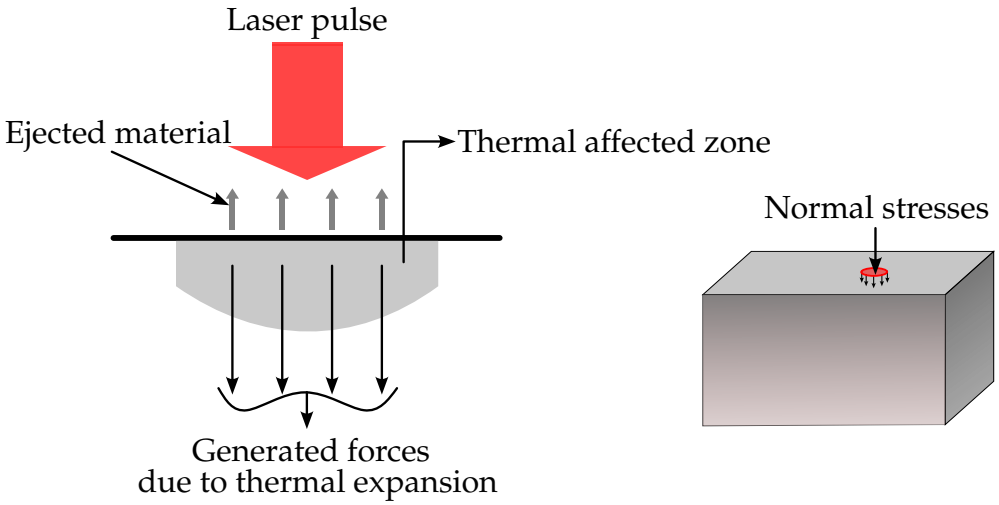

Figure I.8: Ablation regime.

This regime is produced by a momentum transfer phenomenon with forces directed predominantly toward the interior of the material causing degradation and deformation of the material. It is also possible to deposit an absorbing layer on the surface of the sample to be inspected to generate ultrasonic waves in ablation mode without damaging the material.

3.3 Acoustic wave detection methods

There are two categories of optical detection techniques:

- Non-interferometric methods that depend on the reflection of the incident laser beam as the surface acoustic wave passes. For example, the phase grating technique and the knife-edge technique are commonly used [45]. These methods are relatively precise and straightforward to implement, but they are highly sensitive to the surface condition of the sample, which must be as reflective and polished as possible [49, 50].
- Interferometric methods that depend on the interferences generated between multiple coherent waves interacting with each other [4].

Interferometry is based on the concept of superimposing light waves to analyze differences in their paths. Essentially, it splits a single light beam in two: one corresponds to a reference while the other interacts with the sample. The interference pattern of these two beams is analyzed to measure changes in the distance of the sample surface.

Interferometric devices are classified into two main types. In a homodyne interferometer, the detection is based on the interaction between a probe beam and a reference beam, both oscillating at the same frequency. On the other hand, heterodyne interferometry is known by employing two beams that oscillate at different frequencies, maintaining a constant difference. The process of heterodyning is characterized by adjusting the frequency of one or both of these beams to facilitate the analysis of the interference patterns produced [4, 11, 51, 52].

3.3.1 Heterodyne interferometry

Figure I.9 illustrates the principle of the heterodyne interferometer that D. ROYER and E. DIEULESAINT developed [47]. This system features a compact and asymmetric structure of the Mach-Zehnder type which is used in this thesis.

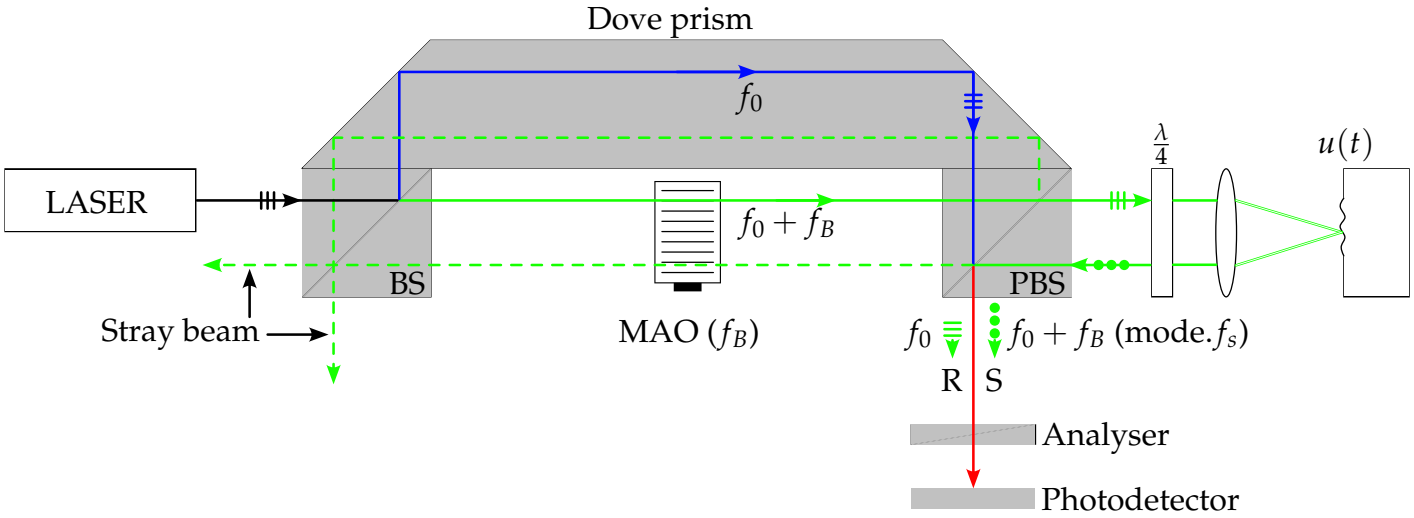

Figure I.9: Principle of heterodyne interferometry [53].

The horizontally polarized source beam of frequency f_0 is split using a cube (or prism) Beam Splitter (BS) into a reference beam (R) and a probe beam (S). The reference beam is then directed through a Dove prism towards a polarization beam splitter Polarization Beam Splitter (PBS). This cube is designed to almost completely transmit a horizontally polarized beam and reflect a vertically polarized beam. Thus, the reference beam continues its path towards the photodetector [4].

The probe beam, on the other hand, is frequency-shifted by 70 MHz through an Acousto-Optic Modulator (AOM) and is in turn transmitted by the PBS [54]. Its polarization becomes circular when passing through the quarter-wave plate ($\frac{\lambda}{4}$) before being focused by a lens on the vibrating surface of the sample. Thus, it interacts with the acoustic wave of frequency f_s propagating at the surface and undergoes phase modulation. Moreover, its polarization is reversed on its second passage through the quarter-wave plate and becomes vertical. Hence, the beam is then reflected toward the photodetector. After the PBS, the probe beam and the reference beam, having different polarizations cannot interfere. Therefore, an analyzer oriented at an angle of $\frac{\pi}{4}$ to the incident polarizations, is used to allow them to interfere. The beam obtained on the photodetector consequently corresponds to the sum of the projections along the axis of the analyzer [4, 47]. Since the polarizations are orthogonal, the components of each beam cancel out to leave only the components of the probe beam. The normal displacement of the acoustic wave is known as:

$$u(t) = A \cdot \cos(2\pi f_s t + \Phi) \tag{1.4}$$

Where A, Φ and f_s are the amplitude, the phase and the frequency of the surface acoustic wave respectively. Moreover, the phase shift of the reflected laser probe beam from the surface of the sample is written as a function of $u(t)$ with $k = \frac{2\pi}{\lambda}$, the wavenumber of the beam:

$$\Delta\varphi_P = 2ku(t) \tag{1.5}$$

The useful information is thus contained in the form of phase modulation. The interference of the probe and reference beams on the photodetector generates frequency components f_B and $f_B \pm f_s$. An electronic signal processing device is present at the output of the photodiode to provide an electrical signal directly proportional to the normal displacement of the sample. For this, a part of the current is taken, filtered at the frequency f_B and phase-shifted by $\frac{\pi}{2}$, thus recombined with the non-taken part. The two output currents from the photodetector can be expressed as [11, 47, 55]:

$$I_1(t) \propto \cos(2\pi f_B t + \Delta\varphi_{PR} + \frac{\pi}{2}) \tag{1.6}$$

$$I_2(t) \propto \cos(2\pi f_B t + \Delta\varphi_{PR} + \Delta\varphi_P) \tag{1.7}$$

where $\Delta\varphi_{PR} = \varphi_P - \varphi_R$ corresponds to the phase difference between the probe beam φ_P and the reference beam φ_R. Finally, the current at the output of the multiplier is written as:

$$I_M(t) = I_1(t) \cdot I_2(t) \propto \sin(\Delta\varphi_P) + \sin(2(2\pi f_B t + \Delta\varphi_{PR})) + \Delta\varphi_P \tag{1.8}$$

Then the signal passes through a low-pass filter to remove the $4\pi f_B$ component. For the SH-140 interferometer, with its detection depending on the filter's cutoff frequency, the signal $I_M(t)$, when acoustic displacement is small compared to the wavelength of the probe beam, simplifies to [4, 11, 47, 55]:

$$I_M(t) \propto 2kA \cdot \cos(2\pi f_s t + \Phi) \tag{1.9}$$

The final electrical signal is thus directly proportional to the normal displacement of the surface of the sample. This technique is very effective for flat and polished surfaces. However, its performance is reduced when the surface of the structure is rough. Indeed, if a rough material reflects the probe beam, it will present a deformed wavefront and the sensitivity will decrease [55].

3.3.2 Holographic interferometry

D. Gabor discovered the principle of holography in 1947, it is based on interference and diffraction phenomena [56]. In the 1960s, K. A. Stetson, R. L. Powell, along with other investigators, contributed significantly in the development of holographic interferometry [57]. The subject has been studied particularly for its use in non-contact/non-destructive testing processes that enable the measurement of surface displacements.

The process starts with holographic recording of an interference pattern onto a two-dimensional medium. It develops a network of fringes resulting from interference between two laser beams: reference beam and probe beam diffracted by the object. This medium where this interference pattern is stored is known as a hologram. During the reconstruction phase (the second phase), this replicated hologram gets illuminated by using the same reference beam that was positioned during the recording stage and thereby images of the object are restored. Interference patterns observed indicate displacements measured at submillimeter scales on objects [4, 55]. In order to calculate such displacements, these observed interferences can be measured accurately only if they are used and they do not require any calibration.

The kinds of holographic interferometry include the following instances [55, 58, 59]:

- Hologram: Recording is done with the object at rest. The reference beam illuminates the same hologram during reconstruction. The interferences in such images show changes in real-time between the present condition of an object and its still state.

- Digital Holography Vibrometry: Successive holograms are made for a vibrating body. Each recording's time interval is set but different from that of the vibration of an object.

Some devices which detect ultrasonic waves operate on principles of holographic interferometry. These have a dynamic hologram recorded in a photorefractive crystal as depicted in figure I.10. The interference pattern is caused by the interaction between the probe beam and the reference beam [4, 60, 61].

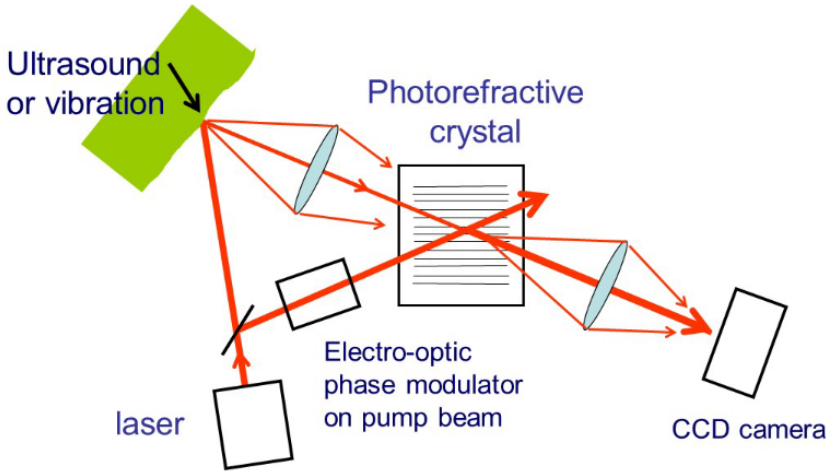

Figure I.10: Principle of holographic interferometry in ultrasonic vibration detection [61].

3.4 Directivity diagrams of Rayleigh waves for a linear source

Directivity diagrams provide an understanding of how a source emits energy across different directions. They enable the generation of acoustic waves at specific frequencies and the focusing of acoustic energy within precise regions of a sample [5, 53]. Rose used Green's function to derive the particle displacement equations associated with the "Surface Center Of Expansion" model in the case of a point source for longitudinal and shear waves for thermoelastic generation [62].

When generating ultrasonic waves in a thermoelastic regime, the shape of the laser is necessary for the directivity and amplitude of the resultant acoustic waves. The propagation of Rayleigh modes from a point laser source causes the energy associated with the surface acoustic wave to be distributed uniformly around the source [63]. However, the generated Rayleigh wave has a low amplitude due to the acoustic energy distributed in all directions from the circular source, leading to

weaker signals detected at any specific position. In this section, we will present these diagrams in the case of a linear source.

To concentrate the acoustic energy and enhance the amplitude of the signals, a cylindrical lens can be applied to focus the laser pulse, giving the beam a linear geometry that results in more directed surface acoustic waves propagating in a coherent direction [64]. Equation 1.10 expresses the directivity function of Rayleigh waves for a linear laser source in a thermoelastic regime [64].

$$D_R(\theta) = \frac{\sin\left(\frac{\pi l f}{c_R}\sin(\theta)\right)}{\frac{\pi l f}{c_R}\sin(\theta)}, \tag{1.10}$$

Where l is the length of the thermoelastic linear source, θ is the angle relative to the normal to the line source, f is the frequency of the surface acoustic wave and c_R the velocity of the Rayleigh wave in the given material.

Figure I.11 shows the directivity diagrams of the Rayleigh wave for several line source lengths (1 mm, 3 mm and 6 mm), for a Rayleigh wave velocity in aluminum of $c_R = 2844$ m/s and a frequency of $f = 2$ MHz. The diagrams demonstrate that the longer the line source, the more directive the Rayleigh wave becomes.

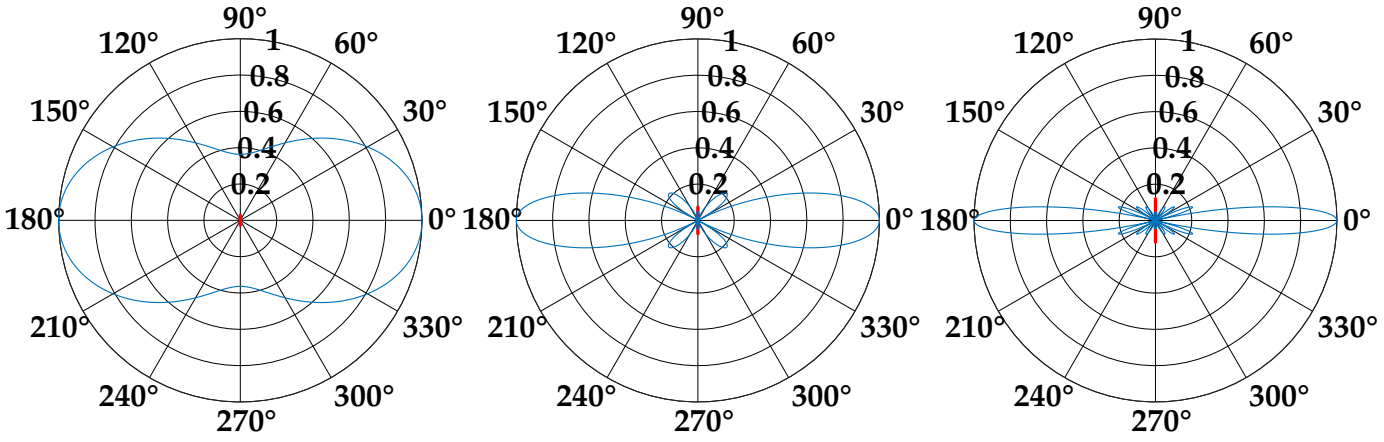

(a) $l = 1$ mm (b) $l = 3$ mm (c) $l = 6$ mm

Figure I.11: Directivity diagrams of Rayleigh waves for a linear source on an aluminum substrate for different lengths: (a) $l = 1$ mm, (b) $l = 3$ mm and (c) $l = 6$ mm.

4 Characteristics of the materials

This section outlines the essential material properties relevant to this thesis. Characterization of the substrate properties is based on direct measurements. However, the properties of the film are derived from existing literature, that is due to the film's flexible composition and microscale dimensions.

4.1 Measurements and uncertainty method

The square-shaped aluminum block has a width and length of 9.8 $\pm$ 0.05 cm and a height of 4.4 $\pm$ 0.05 cm. The block's mass 1.232 kg is determined using a balance with an accuracy of $\pm$ 1 g. This yields a calculated density of $\rho = 2915 \pm 39\ \mathrm{kg/m^3}$.

The uncertainty is calculated using the fundamental principles. This approach is used in the field of experimental physics and is useful in determining the uncertainties in derived quantities based on the uncertainties in the measured quantities. According to Bevington and Robinson [65], the propagation of uncertainty for a function f of several variables $x_1, x_2, \ldots, x_n$ is expressed as:

$$\sigma_f = \sqrt{\left(\frac{\partial f}{\partial x_1}\sigma_{x_1}\right)^2 + \left(\frac{\partial f}{\partial x_2}\sigma_{x_2}\right)^2 + \ldots + \left(\frac{\partial f}{\partial x_n}\sigma_{x_n}\right)^2} \tag{1.11}$$

The uncertainty of the volume is calculated using equation 1.11 as follows:

$$\sigma_V = V\sqrt{\left(\frac{\sigma_l}{l}\right)^2 + \left(\frac{\sigma_w}{w}\right)^2 + \left(\frac{\sigma_h}{h}\right)^2} = 5.7 \times 10^{-6}\ \mathrm{m^3}$$

where l, w and h are the length, width and height, σ_l, σ_w and σ_h, are their corresponding uncertainties respectively. The uncertainty of the mass is $\sigma_m = 0.001$ kg. Therefore σ_ρ is calculated by:

$$\sigma_\rho = \rho\sqrt{\left(\frac{\sigma_m}{m}\right)^2 + \left(\frac{\sigma_V}{V}\right)^2} = 39\ \mathrm{kg/m^3}$$

4.2 Measurement of the longitudinal wave velocity

To determine the velocity of longitudinal waves c_l, a piezoelectric probe with a frequency of 5 MHz is used. This probe generates longitudinal waves that travel through the aluminum substrate along its height (4.4 cm). Upon reaching the substrate's bottom, these waves reflect to the surface, where the same probe detects their reflection. We can calculate the wave's propagation velocity by calculating the duration it takes for the longitudinal wave to travel the substrate's length twice. A smoothed version of the noisy measured signals is presented. Figure I.12 displays the detected signals: the first (a) corresponds to the longitudinal wave used as a reference and the second (b) is its reflection following a single round trip.

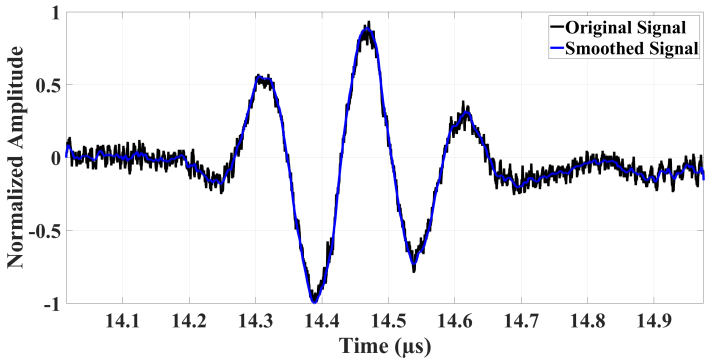

(a) Reference longitudinal wave detected.

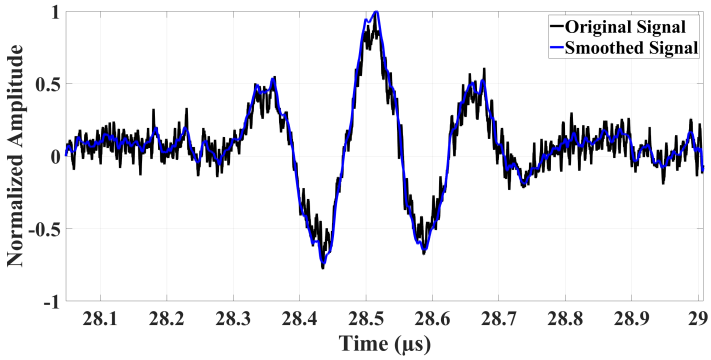

(b) Second reflection of the signal.

Figure I.12: Single round trip of the longitudinal wave traveling through the length of the substrate.

The longitudinal wave velocity v is given by $v = \frac{2 \cdot h}{\Delta t}$, where h is the height of the block and Δt is the time difference for the round trip. Given $h = 4.4$ cm, $\Delta t = 14.02$ μs, and uncertainties $\sigma_h = 0.05$ cm

and $\sigma_t = 0.05$ μs, the velocity is calculated as $v \approx 6276$ m/s. Using the uncertainties formula, $\sigma_v = v\sqrt{\left(\frac{\sigma_h}{h}\right)^2 + \left(\frac{\sigma_t}{\Delta t}\right)^2}$, and substituting the values, we get $\sigma_v = 6276\sqrt{(0.01136)^2 + (0.00357)^2} \approx 75$ m/s. Therefore, the longitudinal wave velocity is $v = 6276 \pm 75$ m/s.

4.3 Measurement of the shear wave velocity

Similar to the previous measurements, a 5 MHz probe, designed for shear waves, is used. A single round trip along the block's length is detected. Figure I.13 displays the signals for two reflections. The first signal (a) corresponds to the reference signal of the shear wave and the second signal (b) is its reflection after a round trip along the length direction of the aluminum block.

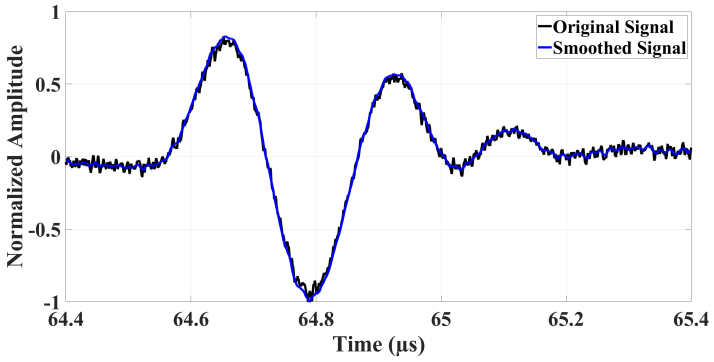

(a) Reference shear wave detected.

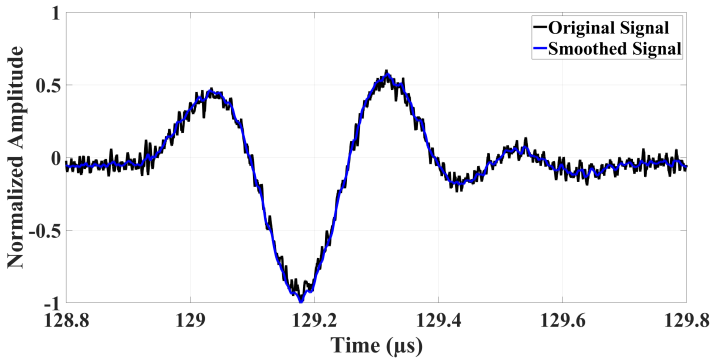

(b) Second reflection of the signal.

Figure I.13: Single round trip of the shear wave traveling through the length of the substrate.

The shear wave velocity v is given by $v = \frac{2 \cdot l}{\Delta t}$, where l is the length of the block and Δt is the time difference for the round trip. Given $l = 9.8$ cm, $\Delta t = 64.39$ μs, and uncertainties $\sigma_l = 0.05$ cm and

$\sigma_t = 0.05$ μs, the velocity is calculated as $v \approx 3044$ m/s. Using the propagation of uncertainties formula, $\sigma_v = v\sqrt{\left(\frac{\sigma_l}{l}\right)^2 + \left(\frac{\sigma_t}{\Delta t}\right)^2}$, and substituting the values, we get $\sigma_v = 3044\sqrt{(0.0051)^2 + (0.00078)^2} \approx 16$ m/s. Therefore, the shear wave velocity in aluminum is calculated to be 3044 ± 16 m/s with a time uncertainty value of 0.05 μs and $\Delta t = 64.39$ μs.

The parameters of the materials are summarized in table I.3, where the properties of the Polyvinyl Chloride (PVC) film were previously measured by M. Robin [5].

	ρ (kg/m^3)	c_t (m/s)	c_l (m/s)	h (μm)
PVC	1300	760	1900	215
Al	2915	3044	6276	-

Table I.3: PVC and Aluminum parameters.

Conclusion

In this chapter, first, the deposition of thin films and their applications in different fields were discussed providing a comparison analysis. Then, in the second section, we explained the different theories that describe the adhesion phenomenon and the methods used to measure and study it, both by destructive and non-destructive testing. Additionally, focusing on the application of ultrasounds in characterizing adhesion, we discussed the corresponding current state-of-the-art techniques including Laser-Ultrasonics.

In the third section, the mechanism of a pulsed laser was explained with its principle for generating ultrasonic waves. Moreover, the interferometric technique was presented as well as the directivity diagrams of the Rayleigh wave using linear sources.

Finally, in the last section, the necessary properties of the materials used experimentally were presented. In the next chapter, the theoretical representation of surface acoustic wave propagation is presented as well as the adhesion effect in a multilayered structure on the surface dispersion.

Bibliography of Chapter I

[1] MC Rao and MS Shekhawat. "A brief survey on basic properties of thin films for device application". In: *International Journal of Modern Physics: Conference Series*. Vol. 22. World Scientific. 2013, pp. 576–582.

[2] Gérard BERANGER and Henri MAZILLE. "Revêtements et traitements de surface. Approche technologique". In: *Techniques de l'ingénieur. Matériaux métalliques* M1426 (2005).

[3] Hartmut Frey. "Applications and developments of thin film technology". In: *Handbook of Thin-Film Technology*. Springer, 2015, pp. 1–3.

[4] Sabrina Fourez. "Caractérisation de couches minces par ondes de surface générées et détectées par sources lasers". PhD thesis. Université de Valenciennes et du Hainaut-Cambresis, 2013.

[5] Martin Robin. "Contribution à l'étude de l'adhérence des structures du type couche sur substrat par modes de Rayleigh générés et détectés par sources laser". PhD thesis. Université de Valenciennes et du Hainaut-Cambresis, 2019.

[6] Michel Massénat. "Circuits en couches minces: Couches minces traditionnelles". In: *Techniques de l'ingénieur. Electronique* 5.E3365 (2003), E3365–1.

[7] Fabien Lefevre. "Caractérisation de structures du type plaque par ondes guidées générées et détectées par laser". PhD thesis. Université de Valenciennes et du Hainaut-Cambrésis, 2010.

[8] J-J Bessot. "Dépôts par pulvérisation cathodique". In: *Métallurgie*. 1985, pp. 1–24.

[9] Christian Manasterski. *La pulvérisation cathodique industrielle*. PPUR presses polytechniques, 2005.

[10] Jean Machet. *Dépôts ioniques*. Ed. Techniques Ingénieur, 1986.

[11] Frédéric Jenot. "Génération et détection d'ondes élastiques par sources lasers: applications au contrôle non destructif". PhD thesis. Valenciennes, 2003.

[12] Sylvain AUDISIO. "Dépôts chimiques à partir d'une phase gazeuse". In: *Techniques de l'ingénieur. Matériaux métalliques* M1660 (1985), pp. M1660–1.

[13] KL Mittal. "The role of the interface in adhesion phenomena". In: *Polymer Engineering & Science* 17.7 (1977), pp. 467–473.

[14] KL Mittal. "Adhesion aspects of metallization of organic polymer surfaces". In: *Journal of vacuum science and technology* 13.1 (1976), pp. 19–25.

[15] N.J. Tro. *Introductory Chemistry*. Pearson Education, 2011. ISBN: 9780321830500. URL: `https://books.google.fr/books?id=abEsAAAAQBAJ`.

[16] Fabio L Leite et al. "Theoretical models for surface forces and adhesion and their measurement using atomic force microscopy". In: *International journal of molecular sciences* 13.10 (2012), pp. 12773–12856.

[17] TR Hull, JS Colligon, and AE Hill. "Measurement of thin film adhesion". In: *Vacuum* 37.3-4 (1987), pp. 327–330.

[18] S Gholizadeh. "A review of non-destructive testing methods of composite materials". In: *Procedia Structural Integrity* 1 (2016), pp. 50–57.

[19] N Nakamura et al. "Resonant-ultrasound spectroscopy for studying annealing effect on elastic constant of thin film". In: *Ultrasonics* 50.2 (2010), pp. 150–154.

[20] Thomas Monnier. "Microscopie acoustique". In: (2014).

[21] Gérard Bourse et al. "Interfacial adhesion characterization of plasma coatings by V (z) inversion technique and comparison to interfacial indentation". In: *NDT & E International* 45.1 (2012), pp. 22–31.

[22] H Wang, ML Qian, and W Liu. "Laser ultrasonic characterization of adhesive bonds between epoxy coating and aluminum substrate". In: *Ultrasonics* 44 (2006), e1349–e1353.

[23] DM Profunser, J Vollmann, and Jürg Dual. "Determination of the material properties of microstructures by laser based ultrasound". In: *Ultrasonics* 42.1-9 (2004), pp. 641–646.

[24] Padmakumar Puthillath and Joseph L Rose. "Ultrasonic guided wave inspection of a titanium repair patch bonded to an aluminum aircraft skin". In: *International Journal of Adhesion and Adhesives* 30.7 (2010), pp. 566–573.

[25] Alejandro Vital Juarez, Arnaud Devos, and Jean-Michel Desmarres. "Quantification of the adhesion of metal thin film interfaces by picosecond acoustics". In: *Forum Acusticum*. 2020, pp. 2833–2834.

[26] Yu Min Choi et al. "Evaluation of Adhesion Properties of Thin Film Structure through Surface Acoustic Wave Dispersion Simulation". In: *Materials* 15.16 (2022), p. 5637.

[27] X Xiao, Y Sun, and X-M Shan. "Nondestructive determination of interfacial adhesion property of low-k/Si by the surface acoustic waves". In: *Surface and Coatings Technology* 207 (2012), pp. 240–244.

[28] Xia Xiao et al. "Study on the interfacial adhesion property of low-k thin film by the surface acoustic waves with cohesive zone model". In: *Applied Surface Science* 388 (2016), pp. 448–454.

[29] D Schneider, H Ollendorf, and Th Schwarz. "Non-destructive evaluation of the mechanical behaviour of TiN-coated steels by laser-induced ultrasonic surface waves". In: *Applied Physics A* 61.3 (1995), pp. 277–284.

[30] H Ollendorf et al. "Non-destructive evaluation of TiN films with interface defects by surface acoustic waves". In: *Surface and Coatings Technology* 74 (1995), pp. 246–252.

[31] Hideo Cho, Shingo Ogawa, and Mikio Takemoto. "Non-contact laser ultrasonics for detecting subsurface lateral defects". In: *NDT & E International* 29.5 (1996), pp. 301–306.

[32] T-T Wu and Y-Y Chen. "Wavelet analysis of laser-generated surface waves in a layered structure with unbond regions". In: *Journal of applied mechanics* 66.2 (1999), pp. 507–513.

[33] François Bruno. "Optimisation des modes de Lamb à vitesse de groupe nulle engendrés par laser et évaluation locale de structures collées". PhD thesis. Université Sorbonne Paris Cité, 2017.

[34] Kuanshuang Zhang and Zhenggan Zhou. "Quantitative characterization of disbonds in multi-layered bonded composites using laser ultrasonic guided waves". In: *NDT & E International* 97 (2018), pp. 42–50.

[35] Kuanshuang Zhang, Shicheng Li, and Zhenggan Zhou. "Detection of disbonds in multi-layer bonded structures using the laser ultrasonic pulse-echo mode". In: *Ultrasonics* 94 (2019), pp. 411–418.

[36] Jakub Kowalczyk et al. "Adhesive Joints of Additively Manufactured Adherends: Ultrasonic Evaluation of Adhesion Strength". In: *Materials* 15.9 (2022), p. 3290.

[37] Kohei Kanamori et al. "Evaluation of adhesion durability of Ni–P coating using repeated Laser Shock Adhesion Test". In: *Surface and Coatings Technology* 396 (2020), p. 125953.

[38] Alfred Johnsen and Knud Rahbek. "A physical phenomenon and its applications to telegraphy, telephony, etc." In: *Journal of the Institution of Electrical Engineers* 61.320 (1923), pp. 713–725.

[39] Jianglong Guo, Jinsong Leng, and Jonathan Rossiter. "Electroadhesion technologies for robotics: A comprehensive review". In: *IEEE Transactions on Robotics* 36.2 (2019), pp. 313–327.

[40] Qiyang Wu et al. "Regulating surface traction of a soft robot through electrostatic adhesion control". In: *2017 IEEE/RSJ international conference on intelligent robots and systems (IROS)*. IEEE. 2017, pp. 488–493.

[41] Xinquan Liang et al. "Delicate manipulations with compliant mechanism and electrostatic adhesion". In: *2016 6th IEEE International Conference on Biomedical Robotics and Biomechatronics (BioRob)*. IEEE. 2016, pp. 401–406.

[42] Gareth J Monkman. "An analysis of astrictive prehension". In: *The International Journal of Robotics Research* 16.1 (1997), pp. 1–10.

[43] Jianglong Guo et al. "Optimization and experimental verification of coplanar interdigital electroadhesives". In: *Journal of Physics D: Applied Physics* 49.41 (2016), p. 415304.

[44] Wei Liu, Xinfeng Tang, and Jeff Sharp. "Low-temperature solid state reaction synthesis and thermoelectric properties of high-performance and low-cost Sb-doped Mg2Si0. 6Sn0. 4". In: *Journal of Physics D: Applied Physics* 43.8 (2010), p. 085406.

[45] Christopher B Scruby and Leslie E Drain. *Laser ultrasonics techniques and applications*. CRC press, 1990.

[46] Catherine Schwob and Lucile Julien. "Le laser: principe de fonctionnement". In: *Reflets de la physique* 21 (2010), pp. 12–16.

[47] Daniel Royer and Eugene Dieulesaint. *Elastic waves in solids II: generation, acousto-optic interaction, applications*. Springer Science & Business Media, 1999.

[48] Betty Isabelle Bleaney, Betty Isabelle Bleaney, and Brebis Bleaney. *Electricity and Magnetism, Volume 2*. Vol. 2. Oxford University Press (UK), 2013.

[49] RL Whitman and A Korpel. "Probing of acoustic surface perturbations by coherent light". In: *Applied Optics* 8.8 (1969), pp. 1567–1576.

[50] D Karabacak et al. "Optical knife-edge technique for nanomechanical displacement detection". In: *Applied physics letters* 88.19 (2006).

[51] D Royer, M-H Noroy, and M Fink. "Optical generation and detection of elastic waves in solids". In: *Le Journal de Physique IV* 4.C7 (1994), pp. C7–673.

[52] Daniel Royer. "Génération et détection optiques d'ondes élastiques". In: *Techniques de l'ingénieur. Electronique* 6.E4415 (1996), E4415–1.

[53] Frédéric Faëse. "Génération d'ondes acoustiques de surface par différentes sources lasers: applications à la caractérisation sans contact de défauts". PhD thesis. Université de Valenciennes et du Hainaut-Cambresis, 2013.

[54] Dieulesaint Royer and Eugène Dieulesaint. "Optical detection of sub-angstrom transient mechanical displacements". In: *IEEE 1986 Ultrasonics Symposium*. IEEE. 1986, pp. 527–530.

[55] Sébastien de Rossi. "Etude et réalisation d'un vibromètre holographique". PhD thesis. Université Pierre et Marie Curie-Paris VI, 2001.

[56] Dennis Gabor. "A new microscopic principle." In: (1948).

[57] Robert L Powell and Karl A Stetson. "Interferometric vibration analysis by wavefront reconstruction". In: *JOSA* 55.12 (1965), pp. 1593–1598.

[58] Paul SMIGIELSKI. *Holographie optique Interférométrie holographique*. Ed. Techniques Ingénieur, 1998.

[59] Ioana Theodora Nistea. "Développement des techniques optiques et acoustiques de mesure de champs orientées vers la vibroacoustique". PhD thesis. INSA de Rouen, 2010.

[60] B Pouet et al. "Laser Ultrasonic Inspection Based on In-Plane Detection and Shear Wave Generation". In: *1st International Symposium on Laser Ultrasonics: Science, Technology and Applications*. 2008.

[61] Jean-Pierre Monchalin. "Laser-ultrasonics: principles and industrial applications". In: *Ultrasonic and advanced methods for nondestructive testing and material characterization*. World Scientific, 2007, pp. 79–115.

[62] LRF Rose. "Point-source representation for laser-generated ultrasound". In: *The Journal of the Acoustical Society of America* 75.3 (1984), pp. 723–732.

[63] Mathieu Perton. "Ultrasons rayonnés par une source laser ponctuelle dans des milieux isotropes transverses et applications à la mesure du tenseur d'élasticité de cylindres et de couches minces". PhD thesis. Université Sciences et Technologies-Bordeaux I, 2006.

[64] AM Aindow, RJ Dewhurst, and SB Palmer. "Laser-generation of directional surface acoustic wave pulses in metals". In: *Optics communications* 42.2 (1982), pp. 116–120.

[65] Philip R. Bevington. *Data Reduction and Error Analysis for the Physical Sciences*. First. McGraw Hill, 1969.

Chapter II

SAW propagation along a multilayered structure

Introduction

The experimental study of any natural behavior needs to be approached by mathematical derivation models. In this chapter, we present the derivation of the theoretical background that describes the propagation of SAW through a multilayered structure.

Surface acoustic waves are influenced by the film and the substrate characteristics. The bonding strength between the layer and the substrate affects also the behavior of these waves. When the bonding forces are weak, the interaction between the SAW and the layer is reduced and there will be no interaction if the layer is completely detached. Conversely, stronger bonding forces increase interaction between the waves and the layer.

This chapter is divided into four sections. The first provides a review of the theory of elasticity. In the second section, solutions to the equation of propagation of bulk and surface acoustic waves for an isotropic medium are presented. Then, the third section focuses on the derivation of the dispersion relation of Lamb waves. Finally, the fourth one discusses the dispersion of Rayleigh waves in a multilayered structure, including the effects of bonding parameters.

1 Theory of elasticity

The theory of elasticity studies how solid materials are deformed in response to external forces in macroscopic physics (higher than atomic scale). It uses mathematical models to predict the behavior of materials under different loads [1].

1.1 Hooke's Law

Hooke's Law is a fundamental principle in the field of elasticity, which relates the stress (force per unit area) applied to a material to the resulting deformation (strain) that occurs. In the linear elasticity regime, this relation can be expressed mathematically as [1, 2, 3]:

$$\sigma_{ij} = C_{ijkl}\varepsilon_{kl} \tag{2.1}$$

where σ_{ij} are the stress tensor components of $[\sigma]$ in the i direction applied to the outgoing normal surface j, ε_{kl} are the strain tensor components of $[\varepsilon]$ in the k direction applied to the outgoing normal surface l and C_{ijkl} are known as the elastic constant tensor components of $[C]$, which depends on the material properties of the studied system.

This relation is only valid in the linear elasticity regime, which means that the deformation must be small enough so that the material can be considered linearly elastic. Outside of this regime, more complex relations between stress and strain can arise.

The tensor $[C]$ exhibits a particular symmetry due to those of the stress tensor $[\sigma]$ and strain tensor $[\varepsilon]$. Specifically, $[C]$ is symmetric with respect to i and j and k and l, such that $C_{ijkl} = C_{jikl} = C_{ijlk} = C_{jilk}$. Furthermore, for energy considerations, $[C]$ also displays symmetry under exchanging the first two and last two indices, such that $C_{ijkl} = C_{klij}$ [3]. This symmetry reduces the number of independent elastic constants in $[C]$ to 21 in the most general case. The number of independent components can be further reduced depending on the crystalline structure of the material, with isotropic materials having only two independent components in $[C]$.

In this context, it is worth noting that the Einstein convention is used, which implies a summation

across the indices k and l in equation 2.1, where k and $l \in [1,3]$. By expressing the strains as a function of the particle displacement u_i in the direction i in equation 2.2, it is possible to establish a relation between stress and particle displacement, since $C_{ijkl} = C_{ijlk}$.

$$\begin{cases} \varepsilon_{ij} = \frac{1}{2}\left(\frac{\partial u_i}{\partial x_j} + \frac{\partial u_j}{\partial x_i}\right) \\ \sigma_{ij} = \frac{1}{2}C_{ijkl}\left(\frac{\partial u_k}{\partial x_l} + \frac{\partial u_l}{\partial x_k}\right) = C_{ijkl}\frac{\partial u_k}{\partial x_l} \end{cases} \tag{2.2}$$

1.2 Newton's second law and the equation of propagation

The fundamental principle of dynamics derived by Newton's second law is expressed as follows:

$$\mathrm{div}([\sigma]) + \vec{f_v} = \rho\frac{\partial^2 \vec{u}}{\partial t^2} \tag{2.3}$$

where div represents the divergence operator, $\vec{f_v}$ denotes the body forces (such as weight), ρ is the mass density of the solid under consideration and $\vec{u}$ is the particle displacement vector. In the presence of external forces, represented by f_{vi}, the fundamental equation of dynamics becomes equation 2.4:

$$\frac{\partial \sigma_{ij}}{\partial x_j} + f_{vi} = \rho\frac{\partial^2 u_i}{\partial t^2} \tag{2.4}$$

The propagation equation (equation 2.5) can be derived using Newton's second law in equation 2.4 and with Hooke's law in equation 2.2. The solutions of equation 2.5 allow us to determine the displacement of particles that characterizes the propagation of an elastic wave. In this case, the loads are assumed to have no impact on the wave propagation and the elastic constants, contained in the rigidities tensor, are uniform and do not vary with the position.

$$\rho\frac{\partial^2 u_i}{\partial t^2} = C_{ijkl}\frac{\partial^2 u_l}{\partial x_k x_j} \tag{2.5}$$

1.3 Bulk waves

The following equation of propagation is the Christoffel equation that is considered for any homogeneous solid, whether isotropic or anisotropic of propagation [4, 5]:

$$\rho V_\phi^2 P_i = C_{ijkl} n_j n_k P_l \tag{2.6}$$

This equation 2.6 explains the effect of elastic properties on wave velocity and displacement in materials so that their propagation through different media can be better understood.

The Christoffel tensor denoted by Γ_{il}, is a second-order tensor obtained by taking the product of the tensor components of the rigidities C_{ijkl} with the direction of wave propagation coordinates $n_j n_k$ in equation 2.6. Then we get:

$$\Gamma_{il} = C_{i11l} n_1^2 + C_{i22l} n_2^2 + C_{i33l} n_3^2 + (C_{i12l} + C_{i21l}) n_1 n_2 + (C_{i13l} + C_{i31l}) n_1 n_3 + (C_{i23l} + C_{i32l}) n_2 n_3 \tag{2.7}$$

To simplify the notation in equation 2.7, the indices of the tensor components of rigidities are converted into matrix notation, such that $a = ij$, $b = kl$ and hence [1]:

$$11 \to 1, 22 \to 2, 33 \to 3, 32 = 23 \to 4, 31 = 13 \to 5, 21 = 12 \to 6$$

The Christoffel tensor is symmetric, since $C_{ijkl} = C_{klij} = C_{lkji}$, then $\Gamma_{il} = C_{ijkl} n_j n_k = C_{lkji} n_k n_j = \Gamma_{li}$ [1]. As a result, the previous Christoffel equation 2.6 can also be expressed as:

$$\rho V_\phi^2 P_i = \Gamma_{il} P_l \tag{2.8}$$

Thus, we can conclude that ρV_ϕ^2 is the eigenvalue of the Christoffel tensor, denoted by Γ_{il} and P_i is its corresponding eigenvector, given by $P_i = P_l \delta_{il}$, where δ_{il} is the Kronecker delta ($\delta_{il} = 1$ if $i = l$ and $\delta_{il} = 0$ if $i \neq l$). The propagation equation can then be expressed as:

$$\left[\Gamma_{il} - \rho V_\phi^2 \delta_{il}\right] P_l = 0 \tag{2.9}$$

The non-trivial solution (where not all components P_l are zero) of this equation occurs when the determinant of the matrix is zero:

$$\left|\Gamma_{il} - \rho V_\phi^2 \delta_{il}\right| = 0 \tag{2.10}$$

For a given direction of propagation, there are three roots to this equation which correspond to three distinct waves and consequently three different phase velocities V_ϕ. Each velocity gives rise to a corresponding eigenvector, the polarization vector $\vec{P}$ which represents the direction of vibration of the particles.

The equations given earlier can be applied to any homogeneous solid, whether isotropic or anisotropic. To simplify the calculations, we will now consider an isotropic solid, where the speed of waves is the same in all directions. In the following, we assume that the waves are propagating in the x_3 direction, with $\vec{n} = \vec{e}_{x_3}$, where $\vec{e}_{x_3}$ is the unit vector corresponding to the x_3 axis. The laser pulse generates different wave types in an isotropic medium. Figure II.1 illustrates these waves [6].

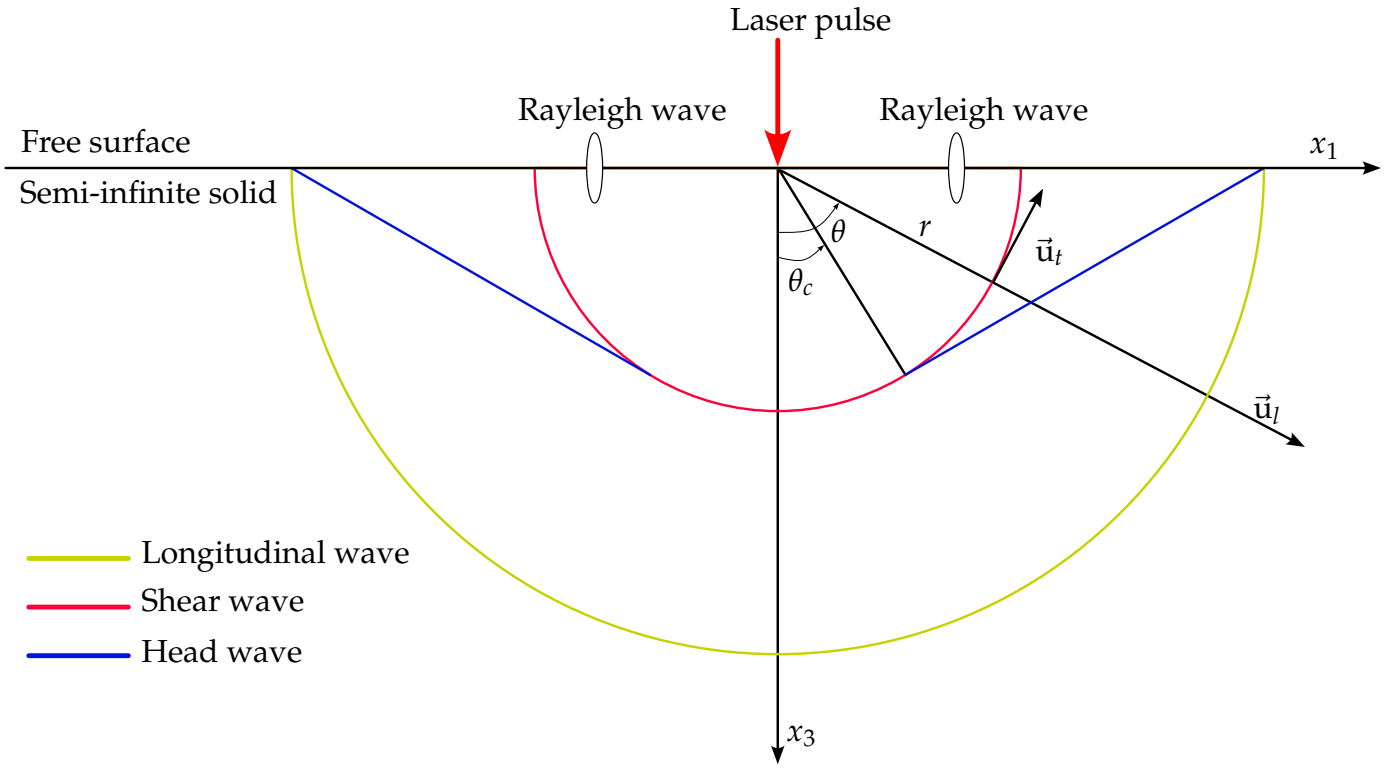

Figure II.1: Wavefronts generated by a laser source in a semi-infinite isotropic solid.

We can summarize the various mechanical disturbances observed at a point $M(r, \theta, t)$ in the case of a free surface-solid interface. The longitudinal wave propagates at the speed c_l and a shear wave propagates at the speed c_t $\left(c_t < \frac{1}{\sqrt{2}} c_l\right)$. Moreover, a surface acoustic wave propagates at the speed c_R, known as Rayleigh wave, with elliptical polarization. This wave has both a longitudinal component and a transverse component, phase-shifted by 90°, lying in the sagittal plane formed by the wave vector and the normal to the surface. The Head wave exists when the point M is at an angle θ such that $|\theta| > \theta_c$, where:

$$\theta_C = \sin^{-1}\left(\frac{c_t}{c_l}\right), \tag{2.11}$$

In this case (isotropic medium), Γ_{il} in the propagation equation 2.9 is written as:

$$\Gamma_{il} = C_{i33l} n_3 n_3 = C_{i33l} \tag{2.12}$$

Hence,

$$[\Gamma] = \begin{bmatrix} C_{55} & C_{54} & C_{53} \\ C_{45} & C_{44} & C_{43} \\ C_{35} & C_{34} & C_{33} \end{bmatrix} \tag{2.13}$$

Only two independent elastic constants, C_{11} and C_{12}, are required to describe the characteristics of an isotropic solid in the stiffness matrix where the only nonzero terms are as follows [7]:

$$\begin{cases} C_{12} = C_{23} = C_{13} = \lambda \\ C_{11} = C_{22} = C_{33} = \lambda + 2\mu \\ C_{44} = C_{55} = C_{66} = \mu = \frac{C_{11} - C_{12}}{2} \end{cases} \tag{2.14}$$

where λ and μ are the 1^{st} and 2^{nd} Lamé constants respectively. The solution represented by equation 2.10, is developed in the following:

$$\begin{vmatrix} \frac{C_{11}-C_{12}}{2} - \rho V_\phi^2 & 0 & 0 \\ 0 & \frac{C_{11}-C_{12}}{2} - \rho V_\phi^2 & 0 \\ 0 & 0 & C_{11} - \rho V_\phi^2 \end{vmatrix} = 0 \tag{2.15}$$

The first two waves have phase velocities of $V_{\phi_1} = V_{\phi_2} = \sqrt{\frac{\mu}{\rho}} = c_t$. The third wave has a phase velocity of $V_{\phi_3} = \sqrt{\frac{\lambda+2\mu}{\rho}} = c_l$. To determine their polarizations, the matrix is projected onto the polarization vector. The projection shows that the first and second waves are polarized in the directions of x_1 and x_2, respectively, while the third wave is polarized in the direction of propagation, x_3.

The first two waves are the transverse waves or shear waves, as their polarization is perpendicular to the direction of wave propagation. The third wave, on the other hand, is referred to as a longitudinal wave or compression wave due to its polarization being parallel with the direction of wave propagation. The equation for wave propagation in an isotropic solid can be written as [8, 3]:

$$\frac{\partial^2 \vec{u}}{\partial t^2} = \frac{(\lambda + 2\mu)}{\rho} \Delta \cdot \vec{u} - \frac{\mu}{\rho} \vec{\nabla} \times (\vec{\nabla} \times \vec{u}) \tag{2.16}$$

where $\times$ is the cross product, $\Delta = \vec{\nabla} \cdot \vec{\nabla} = \nabla^2 = \sum_{i=1}^{3} \frac{\partial^2}{\partial x_i^2}$ and $\vec{\nabla} = \sum_{i=1}^{3} \frac{\partial}{\partial x_i} \vec{e}_{x_i}$.

This equation shows that in an isotropic medium, the displacement vector $\vec{u}$ can be decomposed into a sum of a scalar potential ϕ and a vector potential $\vec{\psi}$, which is not possible in an anisotropic medium where waves are not purely longitudinal or purely shear and cannot be described using purely scalar or vector potential. This decomposition is given by:

$$\vec{u} = \vec{\nabla} \cdot \phi + \vec{\nabla} \times \vec{\psi} = \vec{u}_L + \vec{u}_T \tag{2.17}$$

where $\vec{u}_L$ is the particle displacement of longitudinal waves and $\vec{u}_T$ is the particle displacement of shear waves. These potentials satisfy two properties:

$$\begin{cases} \vec{\nabla} \times \vec{\nabla} \phi = \vec{0} \\ \vec{\nabla} \cdot (\vec{\nabla} \times \vec{\psi}) = 0 \end{cases} \tag{2.18}$$

The wave equation can be separated into two equations using the scalar and vector potentials respectively:

$$\begin{cases} \Delta\phi - \frac{1}{c_l^2}\frac{\partial^2\phi}{\partial t^2} = 0 \\ \Delta\vec{\psi} - \frac{1}{c_t^2}\frac{\partial^2\vec{\psi}}{\partial t^2} = \vec{0} \end{cases} \tag{2.19}$$

where $\Delta\vec{\psi} = \vec{\nabla}\cdot\vec{\nabla}\cdot\vec{\psi} - \vec{\nabla}\times\vec{\nabla}\times\vec{\psi}$. Therefore, $\vec{\nabla}\cdot\vec{\nabla}\times\vec{\psi} = \vec{0}$.

Solving these two equations separately using the method of variable separation results the expressions for $\phi(x_1, x_2, x_3, t)$ and $\vec{\psi}(x_1, x_2, x_3, t)$ and thus for $\vec{u}(\phi, \vec{\psi})$ and $[\sigma(\vec{u})]$. The solutions for ϕ and $\vec{\psi}$ are [4]:

$$\begin{aligned}\phi = \left[A_{t\phi}e^{-i\zeta_{1\phi}c_l t} + B_{t\phi}e^{+i\zeta_{1\phi}c_l t}\right]\left[A_{x_1\phi}e^{-i\zeta_{2\phi}x_1} + B_{x_1\phi}e^{+i\zeta_{2\phi}x_1}\right]\left[A_{x_2\phi}e^{-i\zeta_{3\phi}x_2} + B_{x_2\phi}e^{+i\zeta_{3\phi_2^x}}\right] \\ \left[A_{x_3\phi}e^{-i\zeta_{4\phi}x_3} + B_{x_3\phi}e^{+i\zeta_{4\phi}x_3}\right]\end{aligned} \tag{2.20}$$

and

$$\begin{aligned}\vec{\psi} = \left[\vec{A}_{t\psi}e^{-i\zeta_{1\psi}c_t t} + \vec{B}_{t\psi}e^{+i\zeta_{1\psi}c_t t}\right]\left[\vec{A}_{x_1\psi}e^{-i\zeta_{2\psi}x_1} + \vec{B}_{x_1\psi}e^{+i\zeta_{2\psi}x_1}\right]\left[\vec{A}_{x_2\psi}e^{-i\zeta_{3\psi}x_2} + \vec{B}_{x_2\psi}e^{+i\zeta_{3\psi}x_2}\right] \\ \left[\vec{A}_{x_3\psi}e^{-i\zeta_{4\psi}x_3} + \vec{B}_{x_3\psi}e^{+i\zeta_{4\psi}x_3}\right]\end{aligned} \tag{2.21}$$

A_{mn} and B_{mn} represent the amplitudes of the forward and return going waves, respectively and ζ_{mn} represents the wavenumber. The subscript m can take on the values t, x_1, x_2, or x_3, representing the temporal and spatial components of the magnitudes ϕ and $\vec{\psi}$. The subscript n can take on the values ϕ or $\vec{\psi}$.

The physical meaning of time components only exists when one of the amplitudes is zero, indicating that the wave propagates only along a time dimension. The choice of the temporal direction taken by the wave is merely a convention and the one followed here is $e^{i\omega t}$.

The constant $\zeta_{1\phi}c_l$ should be expressed in $rad.s^{-1}$ or the dimension of a pulse which is denoted

as $\omega = \zeta_{1\phi} c_l = \zeta_{1\psi} c_t$. It is assumed that the same source produces both types of waves and thus has the same oscillation frequency. Similarly, the constant $\zeta_{2,3,4\phi,\psi}$ should be measured as $rad.m^{-1}$, which is the dimension of a wave number, denoted as $\vec{k_t} = \sum_{i=1}^{3} \zeta_{(i+1)\psi} \vec{e}_{x_i} = \sum_{i=1}^{3} k_{ti} \vec{e}_{x_i}$ for the shear waves whose norm is expressed in equation 2.22. Similarly, $\vec{k_l} = \sum_{i=1}^{3} \zeta_{(i+1)\phi} \vec{e}_{x_i} = \sum_{i=1}^{3} k_{li} \vec{e}_{x_i}$ is the wave vector of the longitudinal waves whose norm is expressed in equation 2.23. Finally, we can use equation 2.17 to derive the expressions for particle displacement and equation 2.2 to obtain the stresses.

$$||\vec{k_t}|| = \sqrt{k_{t1}^2 + k_{t2}^2 + k_{t3}^2} = \frac{\omega}{c_t} \tag{2.22}$$

$$||\vec{k_l}|| = \sqrt{k_{l1}^2 + k_{l2}^2 + k_{l3}^2} = \frac{\omega}{c_l} \tag{2.23}$$

2 Surface and guided waves

Acoustic waves, such as surface and guided waves, are widely used for the NDT of materials due to their sensitivity to surrounding properties. Modeling surface acoustic waves, using a mathematical approach to obtain dispersion curves, is important to understand the behavior of these waves while propagating through a structure. This section covers the fundamental concepts related to Rayleigh waves, Lamb waves and the propagation model in layered structures.

2.1 Rayleigh waves

The Rayleigh wave is an elastic wave that propagates on the surface of a semi-infinite medium, implying a thickness much greater than the wavelength of the Rayleigh wave. It exhibits elliptical polarization in the sagittal plane and travels at a slightly slower speed than shear waves. The wave results from a superposition of the longitudinal and shear waves with components phase shifted by $\frac{\pi}{2}$ at the free surface boundary of the solid. The velocity of the Rayleigh wave is calculated using a two-dimensional space described by the density ρ and the Lamé constants λ and μ. Figure II.2

illustrates the two-dimensional space with the origin of the orthonormal coordinate system semi-infinite in x_2 and infinite in x_1 at the surface of the solid.

Figure II.2: Diagram showing the coordinate system on a semi-infinite solid structure described by ρ, λ and μ.

In three-dimensional space, the problem is considered along x_1 and x_2 and variations with respect to x_3 can be neglected. Therefore, the equations for u_1 and u_2 are:

$$\begin{cases} u_1 = \frac{\partial \phi}{\partial x_1} + \frac{\partial \psi_3}{\partial x_2} - \frac{\partial \psi_2}{\partial x_3} = \frac{\partial \phi}{\partial x_1} + \frac{\partial \psi_3}{\partial x_2} \\ u_2 = \frac{\partial \phi}{\partial x_2} + \frac{\partial \psi_1}{\partial x_3} - \frac{\partial \psi_3}{\partial x_1} = \frac{\partial \phi}{\partial x_2} - \frac{\partial \psi_3}{\partial x_1} \end{cases} \tag{2.24}$$

The equations only depend on the component ψ_3 of the vector $\vec{\psi}$ along x_3. For simplicity, this component is denoted as ψ. For a Rayleigh wave, of angular frequency ω and phase velocity c_R, that propagates on the surface of a solid along x_1, its wavenumber k is given by:

$$k = \frac{\omega}{c_R} \tag{2.25}$$

Considering only the forward-going wave along x_1, as there is no returning wave in the $-x_1$ direction due to the medium being infinite in the x_1 direction, thus the amplitudes of the returning waves of ϕ and $\vec{\psi}$ are zero:

$$B_{x_1\phi} = B_{x_1\psi} = 0 \tag{2.26}$$

The Rayleigh wave travels along the surface of a solid medium and only causes particle displacement at a small depth, approximately the same as the wavelength [9]. Consequently, the dependence

of the wave on x_2 can be replicated through an exponential decay function, which indicates an inhomogeneous component of the wave. Therefore, k_{l2} and k_{t2} are purely imaginary.

$$\begin{cases} k_{l2} = -i\sqrt{k^2 - \frac{\omega^2}{c_l^2}} = -ik\sqrt{1 - \frac{c_R^2}{c_l^2}} = k\beta_1 \\ k_{t2} = -i\sqrt{k^2 - \frac{\omega^2}{c_t^2}} = -ik\sqrt{1 - \frac{c_R^2}{c_t^2}} = k\beta_2 \end{cases} \tag{2.27}$$

And the Rayleigh wave's particle displacements that can be expressed as:

$$\begin{cases} u_1 = \left[A_1 e^{-ik\beta_1 x_2} + A_2 e^{ik\beta_1 x_2} + \beta_2 \left(A_3 e^{-ik\beta_2 x_2} - A_4 e^{ik\beta_2 x_2}\right)\right] e^{i(\omega t - k x_1)} \\ u_2 = \left[\beta_1 \left(A_1 e^{-ik\beta_1 x_2} - A_2 e^{ik\beta_1 x_2}\right) - A_3 e^{-ik\beta_2 x_2} - A_4 e^{ik\beta_2 x_2}\right] e^{i(\omega t - k x_1)} \\ \begin{cases} A_1 = -ikB_{t\phi} A_{x_1\phi} A_{x_2\phi} \\ A_2 = -ikB_{t\phi} A_{x_1\phi} B_{x_2\phi} \\ A_3 = -ikB_{t\psi} A_{x_1\psi} A_{x_2\psi} \\ A_4 = -ikB_{t\psi} A_{x_1\psi} B_{x_2\psi} \end{cases} \end{cases} \tag{2.28}$$

Equation 2.2 is used to obtain the expressions for the normal and tangential stresses, σ_{22} and σ_{12}, assuming zero body forces:

$$\sigma_{12} = -ik\left[2\beta_1\left(A_1 e^{-ik\beta_1 x_2} - A_2 e^{ik\beta_1 x_2}\right) + (\beta_2^2 - 1)\left(A_3 e^{-ik\beta_2 x_2} + A_4 e^{ik\beta_2 x_2}\right)\right]\rho c_t^2 e^{i(\omega_t - k x_1)} \tag{2.29}$$

$$\sigma_{22} = -ik\left[(\beta_2^2 - 1)\left(A_1 e^{-ik\beta_1 x_2} + A_2 e^{ik\beta_1 x_2}\right) - 2\beta_2\left(A_3 e^{-ik\beta_2 x_2} - A_4 e^{ik\beta_2 x_2}\right)\right]\rho c_t^2 e^{i(\omega_t - k x_1)} \tag{2.30}$$

Therefore, equations 2.28, 2.29 and 2.30 can be expressed in matrix form as:

$$\begin{pmatrix} u_1 \\ u_2 \\ \sigma_{12} \\ \sigma_{22} \end{pmatrix} =$$

$$\begin{pmatrix} \cos(P_{x_2}) & -i\sin(P_{x_2}) & -i\beta_2\sin(Q_{x_2}) & \beta_2\cos(Q_{x_2}) \\ -i\beta_1\sin(P_{x_2}) & \beta_1\cos(P_{x_2}) & -\cos(Q_{x_2}) & i\sin(Q_{x_2}) \\ -2k\beta_1\sin(P_{x_2})\rho c_t^2 & -i2k\beta_1\cos(P_{x_2})\rho c_t^2 & -ik\left[\beta_2^2-1\right]\cos(Q_{x_2})\rho c_t^2 & -k\left[\beta_2^2-1\right]\sin(Q_{x_2})\rho c_t^2 \\ -ik\left[\beta_2^2-1\right]\cos(P_{x_2})\rho c_t^2 & -k\left[\beta_2^2-1\right]\sin(P_{x_2})\rho c_t^2 & 2k\beta_2\sin(Q_{x_2})\rho c_t^2 & i2k\beta_2\cos(Q_{x_2})\rho c_t^2 \end{pmatrix}$$

$$\cdot \begin{pmatrix} A_1 + A_2 \\ A_1 - A_2 \\ A_3 + A_4 \\ A_3 - A_4 \end{pmatrix} e^{i(\omega t - kx_1)} \tag{2.31}$$

where k is the wavenumber, ρ is the density, c_t is the shear wave speed, β_1 and β_2 are coefficients, t, x_1, u_1, u_2, σ_{12} and σ_{22} are variables, A_1, A_2, A_3 and A_4 are constants. Equation 2.31 represents a system of equations that can be solved simultaneously to determine the values of u_1, u_2, σ_{12} and σ_{22} for given values of the constants and variables, $P_{x_2} = P(x_2) = k\beta_1 x_2$ and $Q_{x_2} = Q(x_2) = k\beta_2 x_2$.

Due to the fact that the medium is semi-infinite in the $+x_2$ direction, any reflected waves propagating in the $-x_2$ direction can be ignored, hence the amplitudes A_2 and A_4 can be set to zero. After imposing the boundary conditions of neglecting the normal and tangential stresses at the free surface, equation 2.31 at $x_2 = 0$ can be expressed as:

$$\begin{pmatrix} u_1 \\ u_2 \\ 0 \\ 0 \end{pmatrix}_{x_2=0} = \begin{pmatrix} 1 & 0 & 0 & \beta_2 \\ 0 & \beta_1 & -1 & 0 \\ 0 & -i2k\beta_1\rho c_t^2 & -ik\left[\beta_2^2-1\right]\rho c_t^2 & 0 \\ -ik\left[\beta_2^2-1\right]\rho c_t^2 & 0 & 0 & i2k\beta_2\rho c_t^2 \end{pmatrix} \begin{pmatrix} A_1 \\ A_1 \\ A_3 \\ A_3 \end{pmatrix} e^{i(\omega t - kx_1)} \quad (2.32)$$

which leads to Rayleigh's equation:

$$\left[\beta_2^2 - 1\right]^2 + 4\beta_1\beta_2 = 0. \quad (2.33)$$

2.2 Lamb waves

When the thickness of a medium or the frequency of the waves is reduced, the waves become guided by the structure instead of being considered infinite compared to the wavelength. These waves are known as Lamb waves for an isotropic and homogeneous plate and are dispersive waves. The process for obtaining the Lamb wave dispersion equation is similar to that of the Rayleigh equation. Equation 2.31 is considered where the thickness of the medium is now finite and four boundary condition equations are required to obtain the dispersion relation of the problem. The medium has a thickness of h and is free on each surface, so the boundary conditions of equation 2.32 must be applied at $x_2 = h$. The equation for the boundary:

$$\begin{pmatrix} \sigma_{12}(x_2=0) \\ \sigma_{22}(x_2=0) \\ \sigma_{12}(x_2=h) \\ \sigma_{22}(x_2=h) \end{pmatrix} =$$

$$\begin{pmatrix} 0 & -i2\beta_1 & -i(\beta_2^2-1) & 0 \\ -i(\beta_2^2-1) & 0 & 0 & i2\beta_2 \\ -2\beta_1\sin(P_h) & -i2\beta_1\cos(P_h) & -i\left[\beta_2^2-1\right]\cos(Q_h) & -\left[\beta_2^2-1\right]\sin(Q_h) \\ -i\left[\beta_2^2-1\right]\cos(P_h) & -\left[\beta_2^2-1\right]\sin(P_h) & 2\beta_2\sin(Q_h) & i2\beta_2\cos(Q_h) \end{pmatrix}$$

$$\cdot \begin{pmatrix} A_1+A_2 \\ A_1-A_2 \\ A_3+A_4 \\ A_3-A_4 \end{pmatrix} \cdot k\rho c_t^2 \cdot e^{i(\omega t-kx_1)} = \begin{pmatrix} 0 \\ 0 \\ 0 \\ 0 \end{pmatrix} \tag{2.34}$$

It is supposed that V_L is the Lamb wave phase velocity. Therefore, we have the following properties:

$$\begin{cases} \beta_1 = -i\sqrt{1-\left(\frac{V_L}{c_l}\right)^2} \\ \beta_2 = -i\sqrt{1-\left(\frac{V_L}{c_t}\right)^2} \\ P_h = k\beta_1 h \\ Q_h = k\beta_2 h \end{cases} \tag{2.35}$$

The dispersion relation for Lamb waves can be obtained by making the determinant of the matrix in equation 2.34 equal to zero. This leads to the identification of two types of Lamb modes, the symmetric and antisymmetric modes, as depicted in figure II.3 [3].

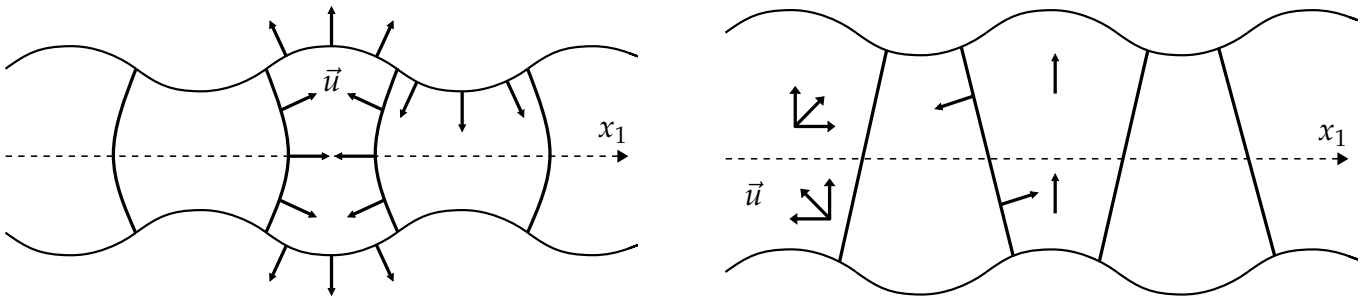

(a) (b)

Figure II.3: Symmetric (a) and antisymmetric (b) Lamb modes illustration.

Another way to express the matrix of equation 2.34 is by changing the origin of the orthonormal system to the center of the plate's thickness and applying the boundary conditions at $x_2 = -h/2$ and $x_2 = h/2$ [10]. This simplifies the equations due to the central symmetry of the sine function and the axial symmetry of the cosine function. The resulting equation is:

$$\begin{pmatrix} \frac{\left[\sigma_{12}\left(x_2=-\frac{h}{2}\right)-\sigma_{12}\left(x_2=+\frac{h}{2}\right)\right]}{2k\rho c_t^2} \\ \frac{\left[\sigma_{22}\left(x_2=-\frac{h}{2}\right)+\sigma_{22}\left(x_2=+\frac{h}{2}\right)\right]}{2k\rho c_t^2} \\ -\frac{\left[\sigma_{12}\left(x_2=-\frac{h}{2}\right)+\sigma_{12}\left(x_2=+\frac{h}{2}\right)\right]}{2k\rho c_t^2} \\ \frac{\left[\sigma_{22}\left(x_2=-\frac{h}{2}\right)-\sigma_{22}\left(x_2=+\frac{h}{2}\right)\right]}{2k\rho c_t^2} \end{pmatrix}$$

$$\begin{pmatrix} 2\beta_1 \sin\left(P_{\frac{h}{2}}\right) & \left[\beta_2^2-1\right]\sin\left(Q_{\frac{h}{2}}\right) & 0 & 0 \\ -i\left[\beta_2^2-1\right]\cos\left(P_{\frac{h}{2}}\right) & 2i\beta_2\cos\left(Q_{\frac{h}{2}}\right) & 0 & 0 \\ 0 & 0 & i\left[\beta_2^2-1\right]\cos\left(Q_{\frac{h}{2}}\right) & 2i\beta_1\cos\left(P_{\frac{h}{2}}\right) \\ 0 & 0 & -2\beta_2\sin\left(Q_{\frac{h}{2}}\right) & \left[\beta_2^2-1\right]\sin\left(P_{\frac{h}{2}}\right) \end{pmatrix}$$

$$\cdot \begin{pmatrix} A_1 + A_2 \\ A_3 - A_4 \\ A_3 + A_4 \\ A_1 - A_1 \end{pmatrix} e^{i(\omega t - kx_1)} = \begin{pmatrix} 0 \\ 0 \\ 0 \\ 0 \end{pmatrix} \tag{2.36}$$

Equation 2.36 can be expressed in the block matrix form as in equation 2.37, where $[M_S]$ and $[M_A]$ represent the matrices whose determinant cancellations give the dispersion relation for symmetric and antisymmetric Lamb modes respectively [8, 10].

$$[M] = \begin{pmatrix} [M_S] & [0] \\ [0] & [M_A] \end{pmatrix} \tag{2.37}$$

The dispersion relations are given by equations 2.38 and 2.39 for symmetric and antisymmetric modes, respectively. These two equations are quite similar and differ only by a phase shift of $\frac{\pi}{2}$.

$$-\frac{4\beta_1\beta_2}{\left(\beta_2^2-1\right)^2}=\frac{\tan\left(Q_{\frac{h}{2}}\right)}{\tan\left(P_{\frac{h}{2}}\right)} \tag{2.38}$$

$$-\frac{4\beta_1\beta_2}{\left(\beta_2^2-1\right)^2}=\frac{\tan\left(P_{\frac{h}{2}}\right)}{\tan\left(Q_{\frac{h}{2}}\right)} \tag{2.39}$$

The phase velocity dispersion curves of the Lamb modes shown in figure II.4 are for a sample of 1.524 mm thick aluminum plate with longitudinal wave velocity of $c_l = 6120$ m/s, shear wave velocity $c_t = 3100$ m/s and a density of $\rho = 2700$ kg/m^3 [11].

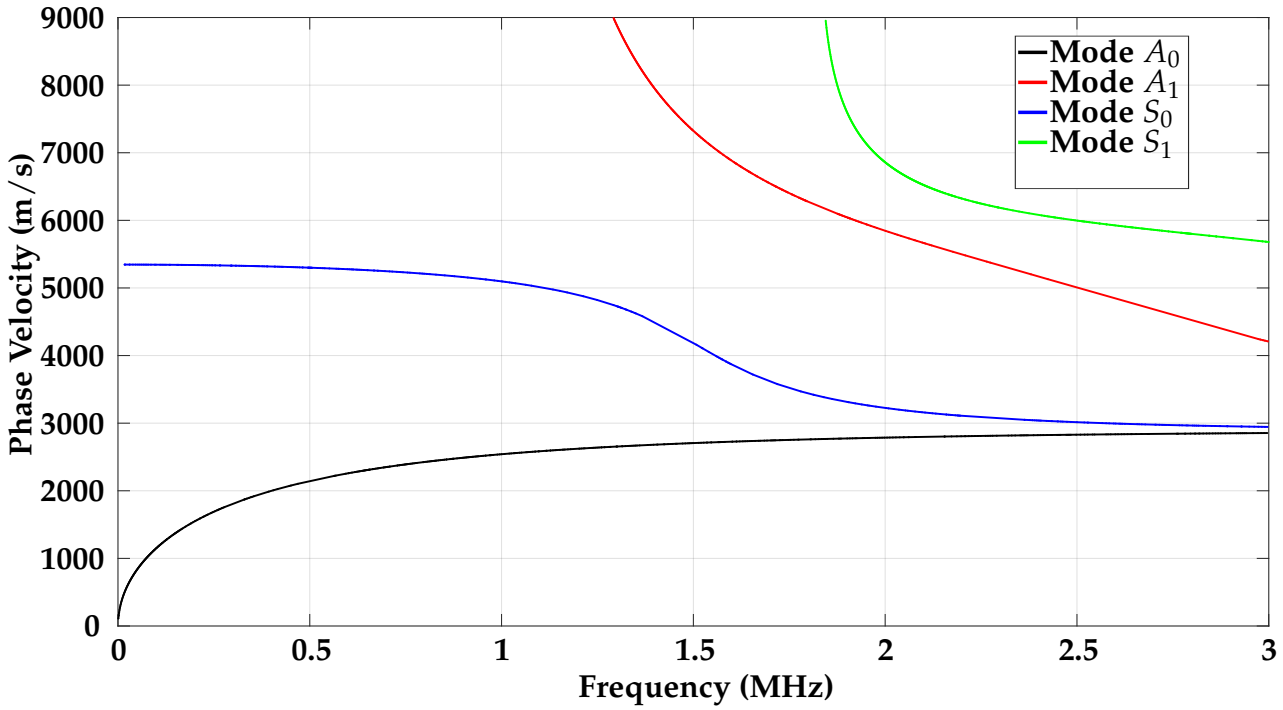

Figure II.4: Lamb modes phase velocity dispersion curves of 1.524 mm thick aluminum plate.

The modes denoted by A correspond to antisymmetric modes, while those denoted by S correspond to symmetric modes. The numerical subscript attached to the letters represents the mode number in order of appearance, according to increasing frequencies. At high frequencies, the A_0 and S_0 modes combine to form the Rayleigh wave, which propagates in a semi-infinite thickness material since the wavelength is much smaller than the thickness of the material. Modes of order 0 are present at all frequencies, but higher-order modes only exist above a certain cutoff frequency.

Figure II.5 displays the dispersion curves for the group velocity of Lamb modes in the same structure. The group velocity, which corresponds to the speed of energy propagation, is not equal to the phase velocity for dispersive waves. The relation between the pulsation ω and the wavenumber k is defined by the group velocity V_g, as shown by the following equation:

$$V_g = \frac{\partial \omega}{\partial k} \tag{2.40}$$

The formula for group velocity, V_g, can be expressed in terms of the frequency, f and the phase velocity,V_ϕ, of the wave as:

$$V_g = \frac{V_\phi^2}{V_\phi - f\frac{\partial V_\phi}{\partial f}} \tag{2.41}$$

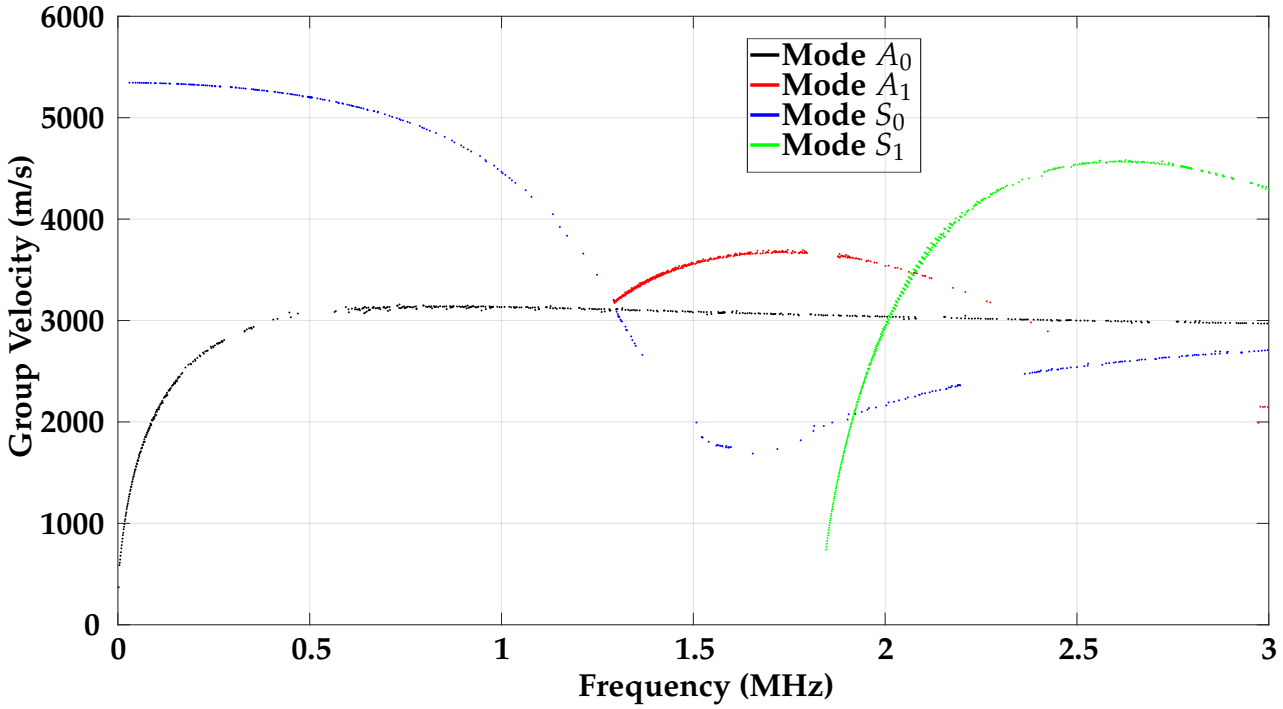

Figure II.5: Lamb modes group velocity dispersion curves of 1.524 mm thick aluminum plate.

If the partial derivative of the phase velocity with respect to frequency is zero, i.e., $\frac{\partial V_\phi}{\partial f} = 0$, then the group velocity is equal to the phase velocity.

2.3 Matrix transfer method in multilayered structure

In a multilayered structure, the surface acoustic waves are dispersive, as each layer has a different effect on the waves' propagation. This leads to the identification of Rayleigh modes. The dispersion relations of these waves can be obtained using a similar approach as introduced in figure II.2 but with a multilayered structure. Figure II.6 shows a structure with n layers and a semi-infinite substrate, of a uniform multilayered structure. In this model, Lame's constants are denoted by λ and μ and ρ is the density. The amplitudes of downgoing and upgoing longitudinal waves are represented by P and P' respectively. Similarly, S and S' correspond to the amplitudes of downgoing and upgoing shear waves respectively [12].

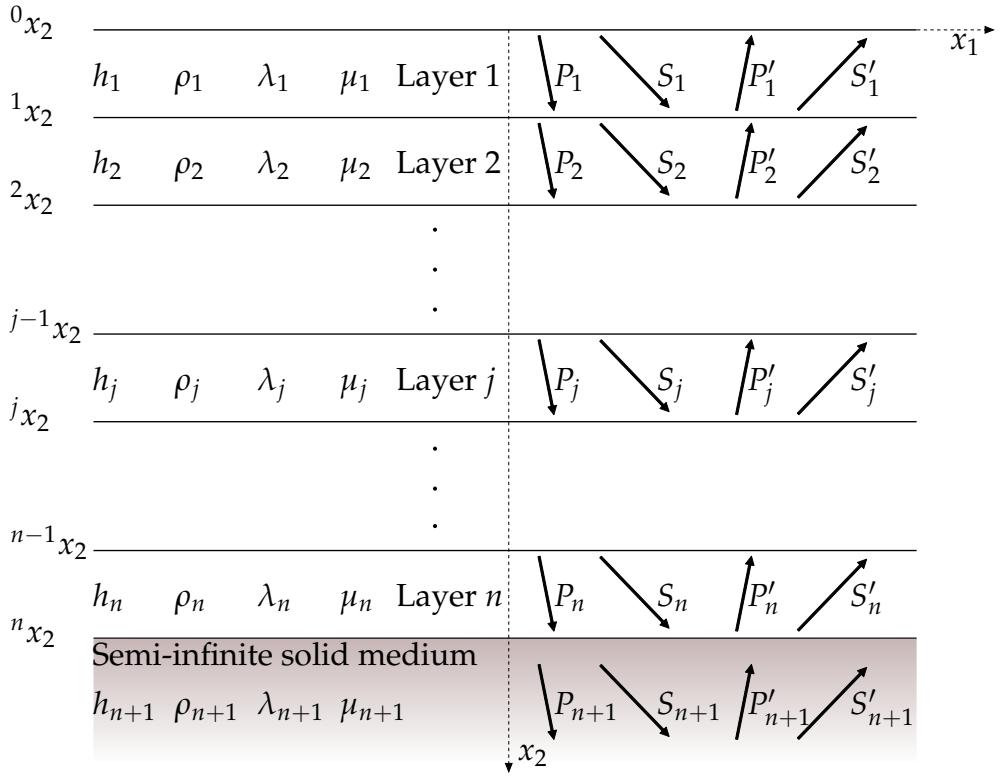

Figure II.6: Diagram showing the coordinate system on a semi-infinite solid structure described by ρ, λ and μ.

The transfer matrix method, first introduced by Thomson in 1950 and later adapted by Haskell in 1951, is a highly flexible numerical calculation method that involves matrices in the computation of reflection and transmission coefficients for bulk waves in a multilayered medium. Later, Haskell

improved this method to accommodate surface acoustic waves [13, 14].

According to equation 2.31, it is possible to formulate the stresses and displacements in any layer j, with $j \in [0, n]$. The equations for these values can be written as follows:

$$\begin{pmatrix} u_{1j} \\ u_{2j} \\ \sigma_{12j} \\ \sigma_{22j} \end{pmatrix} =$$

$$\begin{pmatrix} \frac{\cos(P_{jx_2})}{k\rho_j c_{tj}^2} & \frac{-i\sin(P_{jx_2})}{k\rho_j c_{tj}^2} & \frac{-i\beta_{2j}\sin(Q_{jx_2})}{k\rho_j c_{tj}^2} & \frac{\beta_{2j}\cos(Q_{jx_2})}{k\rho_j c_{tj}^2} \\ \frac{-i\beta_{1j}\sin(P_{jx_2})}{k\rho_j c_{tj}^2} & \frac{\beta_{1j}\cos(P_{jx_2})}{k\rho_j c_{tj}^2} & \frac{-\cos(Q_{jx_2})}{k\rho_j c_{tj}^2} & \frac{i\sin(Q_{jx_2})}{k\rho_j c_{tj}^2} \\ -2\beta_{1j}\sin(P_{jx_2}) & -i2\beta_{1j}\cos(P_{jx_2}) & -i\left[\beta_{2j}^2 - 1\right]\cos(Q_{jx_2}) & -\left[\beta_{2j}^2 - 1\right]\sin(Q_{jx_2}) \\ -i\left[\beta_{2j}^2 - 1\right]\cos(P_{jx_2}) & -\left[\beta_{2j}^2 - 1\right]\sin(P_{jx_2}) & 2\beta_{2j}\sin(Q_{jx_2}) & i2\beta_{2j}\cos(Q_{jx_2}) \end{pmatrix}$$

$$\cdot \begin{pmatrix} A_{1j} + A_{2j} \\ A_{1j} - A_{2j} \\ A_{3j} + A_{4j} \\ A_{3j} - A_{4j} \end{pmatrix} \cdot k\rho_j c_{tj}^2 \cdot e^{i(\omega t - kx_1)} \tag{2.42}$$

j indicates the layer number and $\beta_{1j} = -i\sqrt{1 - \left(\frac{V_{MR}}{c_{lj}}\right)^2}$, where V_{MR} represents the phase velocity of the Rayleigh modes and c_{lj} represents the velocity of the longitudinal waves in the j^{th} layer. Equation 2.42 can be written as:

$$\left[\eta_j\left(x_1, x_2, t\right)\right] = \left[M_j\left(x_2\right)\right]\left[A_j\right] f\left(x_1, t\right), \tag{2.43}$$

with

$$\begin{cases} \left[\eta_j\left(x_1, x_2, t\right)\right] = \begin{pmatrix} u_{1j} \\ u_{2j} \\ \sigma_{12j} \\ \sigma_{22j} \end{pmatrix} \\ \left[M_j\left(x_2\right)\right] : \text{The matrix of stresses in equation 2.42} \\ \left[A_j\right] = \begin{pmatrix} A_{1j} + A_{2j} \\ A_{1j} - A_{2j} \\ A_{3j} + A_{4j} \\ A_{3j} - A_{4j} \end{pmatrix} \\ f\left(x_1, t\right) = e^{i(\omega t - k x_1)} \end{cases} \tag{2.44}$$

Hence, the transfer matrix for layer j is formulated in equation 2.46, based on the expressions for the particle stresses and displacements at the boundaries between layers $j-1$ and j (represented by depth ${}^{j-1}x_2$) as well as between layers j and $j+1$ (indicated by depth ${}^{j}x_2$). Consequently, the difference ${}^{j}x_2 - {}^{j-1}x_2$ corresponds to h_j, which is the thickness of the j^{th} layer. We know that:

$$\begin{cases} \left[\eta_j\left(x_1, x_2 = {}^{j}x_2, t\right)\right] = \left[M_j\left(x_2 = {}^{j}x_2\right)\right]\left[A_j\right] f\left(x_1, t\right) \\ \left[\eta_j\left(x_1, x_2 = {}^{j-1}x_2, t\right)\right] = \left[M_j\left(x_2 = {}^{j-1}x_2\right)\right]\left[A_j\right] f\left(x_1, t\right) \end{cases} \tag{2.45}$$

Hence, $\left[A_j\right] f\left(x_1, t\right) = \left[M_j\left(x_2 = {}^{j-1}x_2\right)\right]^{-1}\left[\eta_j\left(x_1, x_2 = {}^{j-1}x_2, t\right)\right]$ and thus:

$$\left[\eta_j\left(x_1, x_2 = {}^{j}x_2, t\right)\right] = \left[M_j\left(x_2 = {}^{j}x_2\right)\right]\left[M_j\left(x_2 = {}^{j-1}x_2\right)\right]^{-1}\left[\eta_j\left(x_1, x_2 = {}^{j-1}x_2, t\right)\right] \tag{2.46}$$

Considering the boundary conditions:

$$\begin{cases} \left[\eta_j\left(x_1, x_2 = {}^{j}x_2, t\right)\right] = \left[\eta_{j+1}\left(x_1, x_2 = {}^{j}x_2, t\right)\right] \\ \left[\eta_j\left(x_1, x_2 = {}^{j-1}x_2, t\right)\right] = \left[\eta_{j-1}\left(x_1, x_2 = {}^{j-1}x_2, t\right)\right] \end{cases} \tag{2.47}$$

This implies that $\left[M_j\left({}^{j}x_2\right)\right]\left[M_j\left({}^{j-1}x_2\right)\right]^{-1} = \left[M_j\left(h_j\right)\right]\left[M_j\left(0\right)\right]^{-1}$. We can then establish a relation between the transfer matrices of layers $j+1$, j and $j-1$. Therefore, it is possible to connect the properties of layer n with those of layer 1 by the following expression:

$$\left[\eta_n\left(x_1, x_2 =^n x_2, t\right)\right] = \left(\left[M_n\left(h_n\right)\right]\left[M_n\left(0\right)\right]^{-1} \ldots \left[M_1\left(h_1\right)\right]\left[M_1\left(0\right)\right]^{-1}\right) \cdot \left[\eta_1\left(x_1, x_2 = 0, t\right)\right] \tag{2.48}$$

Since $\left[\eta_n\left(x_1, x_2 =^n x_2, t\right)\right] = \left[\eta_{n+1}\left(x_1, x_2 =^n x_2, t\right)\right] = \left[M_{n+1}\left(x_2 =^n x_2\right)\right]\left[A_{n+1}\right] f\left(x_1, t\right)$ and taking into account the boundary conditions at the top boundary of the initial layer (stress cancellation) as well as within the substrate (Sommerfeld condition, absence of a returning wave due to semi-infinite medium propagation, leading to $A_2 = A_4 = 0$), the following expression can be obtained:

$$\begin{pmatrix} A_{1n+1} \\ A_{1n+1} \\ A_{3n+1} \\ A_{3n+1} \end{pmatrix} \cdot f(x_1, t) = [\mathbf{M}] \cdot \begin{pmatrix} u_{11}(x_1, x_2 = 0, t) \\ u_{21}(x_1, x_2 = 0, t) \\ 0 \\ 0 \end{pmatrix} \tag{2.49}$$

Where $[\mathbf{M}]$ is the matrix of stresses and displacements that relates the layers of the system together as:

$$[\mathbf{M}] = \left[M_{n+1}\left(0\right)\right]^{-1} \cdot \left(\left[M_n\left(h_n\right)\right]\left[M_n\left(0\right)\right]^{-1}\right) \ldots \left(\left[M_1\left(h_1\right)\right]\left[M_1\left(0\right)\right]^{-1}\right) \tag{2.50}$$

Thus, the resulting system of equations is:

$$\begin{cases} A_{1n+1} f(x_1, t) = M_{11} u_{11}(x_1, x_2 = 0, t) + M_{12} u_{21}(x_1, x_2 = 0, t) \\ A_{1n+1} f(x_1, t) = M_{21} u_{11}(x_1, x_2 = 0, t) + M_{22} u_{21}(x_1, x_2 = 0, t) \\ A_{3n+1} f(x_1, t) = M_{31} u_{11}(x_1, x_2 = 0, t) + M_{32} u_{21}(x_1, x_2 = 0, t) \\ A_{3n+1} f(x_1, t) = M_{41} u_{11}(x_1, x_2 = 0, t) + M_{42} u_{21}(x_1, x_2 = 0, t) \end{cases} \tag{2.51}$$

Where $M_{a_1 a_2}$ represents the matrix elements of $[\mathbf{M}]$ in the a_1^{th} row and a_2^{th} column. Subtracting

the amplitudes of waves in the substrate, the ratio of particle displacements at the surface of the multilayer can be determined:

$$\frac{u_{21}(x_1, x_2 = 0, t)}{u_{11}(x_1, x_2 = 0, t)} = \frac{M_{21} - M_{11}}{M_{12} - M_{22}} = \frac{M_{41} - M_{31}}{M_{32} - M_{42}}. \tag{2.52}$$

The matrix $[\mathbf{M}]$ only depends on the wavenumber k and the Rayleigh mode phase velocity V_{MR}. Finally, the dispersion relation is expressed as:

$$\frac{M_{21} - M_{11}}{M_{12} - M_{22}} - \frac{M_{41} - M_{31}}{M_{32} - M_{42}} = 0. \tag{2.53}$$

3 Perfect contact of a single layer on a substrate

For a single layer deposited on a substrate, there are three possible situations for Rayleigh modes depending on the relation between the shear wave velocities of the layers [7, 15]. In this section, the solution of the matrix multiplication using mathematical software will be first presented. It is then included in the software to plot the dispersion curves. Results are compared to those of Farnell and Adler [7]. Finally, in the developed program are integrated the characteristics of the materials used experimentally.

3.1 Numerical calculation of the dispersion relation

For a single layer deposited on a semi-infinite substrate, equation 2.50 is written as:

$$[\mathbf{M}] = \left[M_{\text{Substrate}}\,(0)\right]^{-1} \cdot \left(\left[M_{\text{Film}}\,(h_{\text{Film}})\right]\left[M_{\text{Film}}\,(0)\right]^{-1}\right) \tag{2.54}$$

A software is used to calculate the matrix $[\mathbf{M}]$ by calculating the multiplication of the three matrices $\left[M_{\text{Substrate}}\,(0)\right]^{-1}$, $\left[M_{\text{Film}}\,(h_{\text{Film}})\right]$ and $\left[M_{\text{Film}}\,(0)\right]^{-1}$. The input holds all the variables of these matrices as follows:

$$\begin{cases} [M_1] = \begin{pmatrix} 1 & 0 & 0 & \beta_2 \\ 0 & \beta_1 & -1 & 0 \\ 0 & -2ik\beta_1\rho c_t^2 & -ik(\beta_2^2-1)\rho c_t^2 & 0 \\ -ik(\beta_2^2-1)\rho c_t^2 & 0 & 0 & 2ik\beta_2\rho c_t^2 \end{pmatrix} \\ [M_2] = \begin{pmatrix} \frac{\cos(\hat{P}_h)}{k\hat{\rho}\hat{c}_t^2} & \frac{-i\sin(\hat{P}_h)}{k\hat{\rho}\hat{c}_t^2} & \frac{-i\hat{\beta}_2\sin(\hat{Q}_h)}{k\hat{\rho}\hat{c}_t^2} & \frac{\hat{\beta}_2\cos(\hat{Q}_h)}{k\hat{\rho}\hat{c}_t^2} \\ \frac{-i\hat{\beta}_1\sin(\hat{P}_h)}{k\hat{\rho}\hat{c}_t^2} & \frac{\hat{\beta}_1\cos(\hat{P}_h)}{k\hat{\rho}\hat{c}_t^2} & \frac{-\cos(\hat{Q}_h)}{k\hat{\rho}\hat{c}_t^2} & \frac{i\sin(\hat{Q}_h)}{k\hat{\rho}\hat{c}_t^2} \\ -2\hat{\beta}_1\sin(\hat{P}_h) & -i2\hat{\beta}_1\cos(\hat{P}_h) & -i\left[\hat{\beta}_2^2-1\right]\cos(\hat{Q}_h) & -\left[\hat{\beta}_2^2-1\right]\sin(\hat{Q}_h) \\ -i\left[\hat{\beta}_2^2-1\right]\cos(\hat{P}_h) & -\left[\hat{\beta}_2^2-1\right]\sin(\hat{P}_h) & 2\hat{\beta}_2\sin(\hat{Q}_h) & i2\hat{\beta}_2\cos(\hat{Q}_h) \end{pmatrix} \cdot k\rho_j c_{tj}^2 \\ [M_3] = \begin{pmatrix} 1 & 0 & 0 & \hat{\beta}_2 \\ 0 & \hat{\beta}_1 & -1 & 0 \\ 0 & -2ik\hat{\beta}_1\hat{\rho}\hat{c}_t^2 & -ik(\hat{\beta}_2^2-1)\hat{\rho}\hat{c}_t^2 & 0 \\ -ik(\hat{\beta}_2^2-1)\hat{\rho}\hat{c}_t^2 & 0 & 0 & 2ik\hat{\beta}_2\hat{\rho}\hat{c}_t^2 \end{pmatrix} \end{cases} \tag{2.55}$$

Hence the output of $[M_1]^{-1}$ and $[M_3]^{-1}$ are:

$$\begin{cases} [M_{\text{Substrate}}(0)]^{-1} = [M_1]^{-1} = \begin{pmatrix} \frac{2}{\beta_2^2+1} & 0 & 0 & \frac{i}{k\rho c_t^2(\beta_2^2+1)} \\ 0 & \frac{\beta_2^2-1}{(\beta_2^2+1)\beta_1} & \frac{i}{k\rho c_t^2(\beta_2^2+1)\beta_1} & 0 \\ 0 & -\frac{2}{\beta_2^2+1} & \frac{i}{k\rho c_t^2(\beta_2^2+1)} & 0 \\ \frac{\beta_2^2-1}{\beta_2(\beta_2^2+1)} & 0 & 0 & -\frac{i}{k\beta_2\rho c_t^2(\beta_2^2+1)} \end{pmatrix} \\ [M_{\text{Film}}(0)]^{-1} = [M_3]^{-1} = \begin{pmatrix} \frac{2}{\hat{\beta}_2^2+1} & 0 & 0 & \frac{i}{k\hat{\rho}\hat{c}_t^2(\hat{\beta}_2^2+1)} \\ 0 & \frac{\hat{\beta}_2^2-1}{(\hat{\beta}_2^2+1)\hat{\beta}_1} & \frac{i}{k\hat{\rho}\hat{c}_t^2(\hat{\beta}_2^2+1)\hat{\beta}_1} & 0 \\ 0 & -\frac{2}{\hat{\beta}_2^2+1} & \frac{i}{k\hat{\rho}\hat{c}_t^2(\hat{\beta}_2^2+1)} & 0 \\ \frac{\hat{\beta}_2^2-1}{\hat{\beta}_2(\hat{\beta}_2^2+1)} & 0 & 0 & -\frac{i}{k\hat{\beta}_2\hat{\rho}\hat{c}_t^2(\hat{\beta}_2^2+1)} \end{pmatrix} \end{cases} \tag{2.56}$$

We can calculate $[M_1]^{-1} \cdot [M_2] \cdot [M_3]^{-1}$. Once we have the result of this calculation we can then ex-

tract the matrix elements M_{21}, M_{11}, M_{12}, M_{22} M_{41}, M_{31}, M_{32} and M_{42} and then compute the formula of the term in equation 2.53. The computed term will then be generated in the developed program in the form of a polynomial.

Finally, this polynomial allows to plot the phase velocity values V_{MR} at each frequency when it is approximately zero.

3.2 SAW dispersion behaviour for single layer on substrate

3.2.1 Loading case

This first case respects the following condition:

$$\frac{\hat{c}_t}{c_t} < \frac{1}{\sqrt{2}} \tag{2.57}$$

where $\hat{c}_t$ denotes the shear wave speed in the layer and c_t represents the speed in the substrate. In this case, the layer "loads" the substrate, causing its mechanical properties to slow down the surface acoustic wave. It is characterized by the existence of multiple modes, with the phase velocity decreasing as the frequency increases.

A loading case example of the phase velocity dispersion curves of Gold (Au) layer of thickness $h = 1$ μm, $\hat{c}_l = 3361$ m/s, $\hat{c}_t = 1236$ m/s and $\hat{\rho} = 19572$ kg/m^3, deposited on a Fused Quartz (SiO_2) substrate of $c_l = 6050$ m/s, $c_t = 4100$ m/s and $\rho = 2641$ kg/m^3 [7], is plotted in figure II.7.

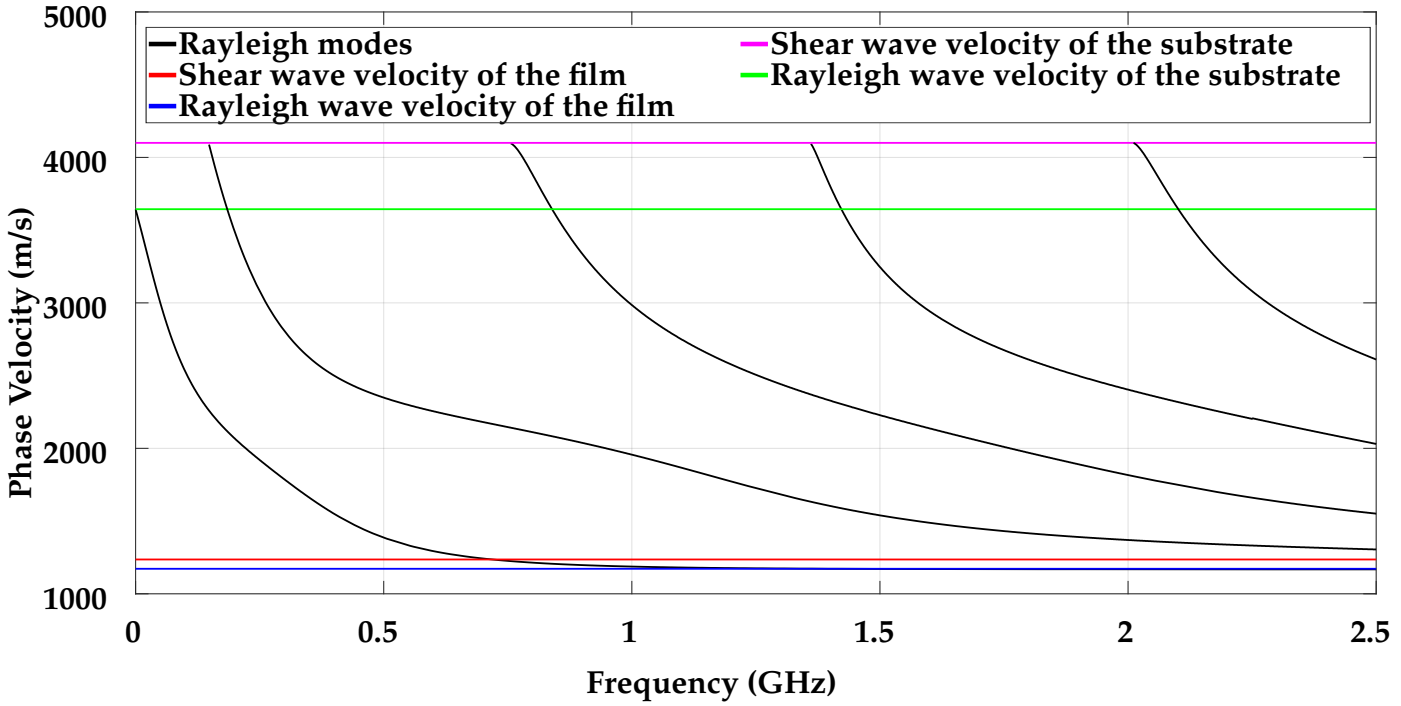

Figure II.7: Rayleigh modes in the loading case of a 1 μm gold layer deposited on a fused quartz substrate.

The phase velocity curves as shown in figure II.7 show the initial Rayleigh mode at the substrate's Rayleigh wave velocity. This is because, at low frequencies, the wavelength is considerably larger than the layer's thickness and thus the layer's influence on wave propagation is negligible. As the frequency rises, the phase velocity of the mode decreases until it reaches the Rayleigh wave velocity within the layer. At high frequencies, the wavelength becomes sufficiently small to the layer's thickness which is considered semi-infinite, causing the wave to transform into a Rayleigh wave within the layer. The changes in the ratio of the wavelength to the layer's thickness at various frequencies are indeed the cause of surface acoustic wave dispersion. As the frequency increases, the layer's impact on wave propagation becomes progressively more significant. A similar occurrence can be seen for higher-order modes, where the low-frequency phase velocity at which they appear corresponds to the shear wave velocity in the substrate. As the frequency rises, the phase velocity of these modes approaches the shear wave velocity within the layer.

3.2.2 Stiffening case

This second case respects the following condition:

$$\frac{\hat{c}_t}{c_t} > \sqrt{2} \tag{2.58}$$

In this case, the layer strengthens the mechanical properties of the substrate, leading to an increase in the phase velocity of the surface acoustic wave. As a result, only one mode exists, with its velocity increasing as the frequency increases.

Figure II.8 shows the surface dispersion for the stiffening case example of a 1 μm thickness of Silicon (Si) layer of $\hat{c}_l = 8945$ m/s, $\hat{c}_t = 5341$ m/s and $\hat{\rho} = 2331$ kg/m^3 deposited on a Zinc Oxide (ZnO) substrate of $c_l = 6000$ m/s, $c_t = 2831$ m/s and $\rho = 5675$ kg/m^3 [7].

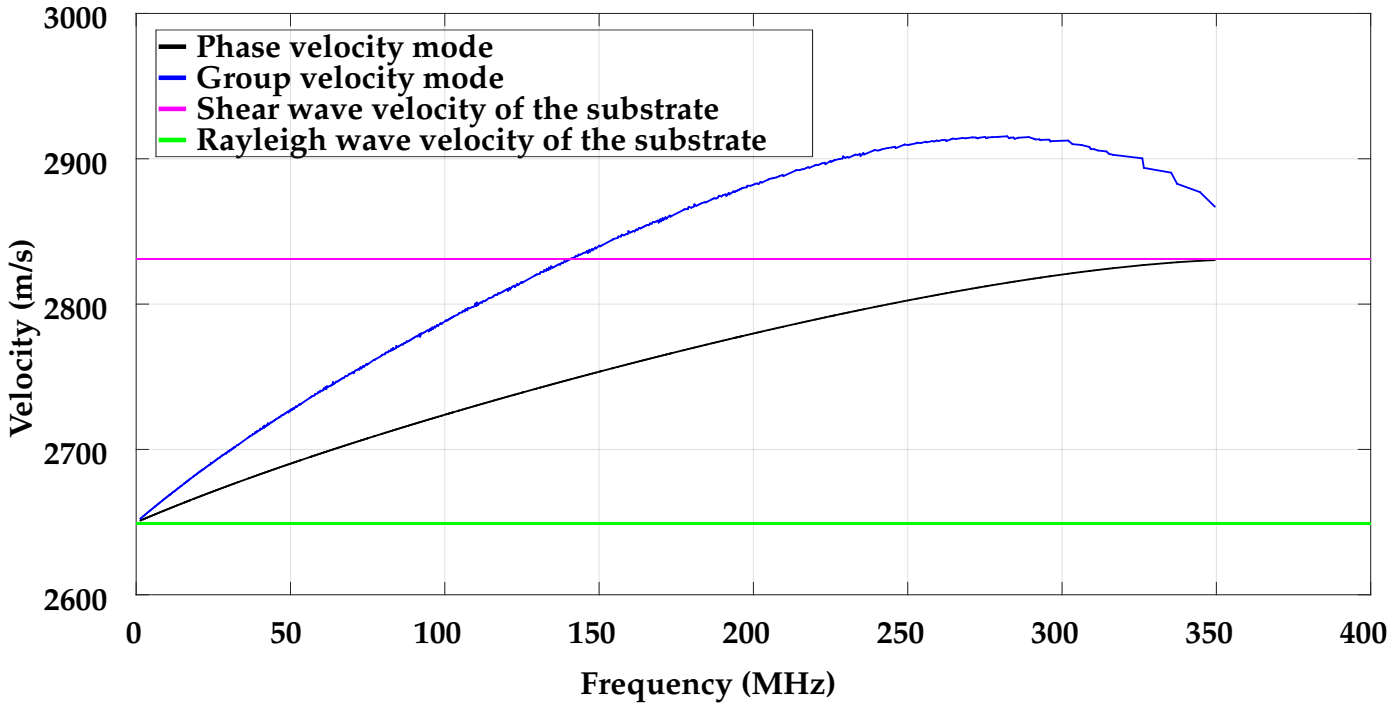

Figure II.8: Rayleigh mode phase velocity in black and group velocity in blue for the stiffening case corresponding to a structure composed of 1 μm silicon layer deposited on a zinc oxide substrate.

At low frequencies, the Rayleigh mode approaches the velocity of the Rayleigh wave of the substrate, due to the large wavelength of the wave, where it is much larger than the order of the thickness of the layer, therefore the elastic properties of the layer are not able to affect the Rayleigh mode. As

frequency increases, the wavelength becomes relatively small. The effect of the layer's mechanical properties starts to increase the phase velocity of the mode until it reaches a high cut-off frequency at which the generated wave becomes a shear wave. This occurs at around 360 MHz corresponding to a wavelength of approximately 8 μm by tracking the velocity of the Rayleigh mode in figure II.8. Therefore, the layer is never considered as semi-infinite relative to the Rayleigh mode wavelength propagating within the structure.

3.2.3 Intermediate case

Finally, the third case respects the following condition:

$$\frac{1}{\sqrt{2}} < \frac{\hat{c}_t}{c_t} < \sqrt{2} \tag{2.59}$$

There can be one or multiple Rayleigh modes in this case depending on the materials considered, for which the curves are no longer monotonic. Figure II.9 presents the dispersion curves of the intermediate case where 1 μm thick Tungsten (W) layer of longitudinal wave velocity $\hat{c}_l = 5231$ m/s, shear wave velocity $\hat{c}_t = 2860$ m/s and density $\hat{\rho} = 18705$ kg/m^3, deposited on an aluminum substrate of $c_l = 6422$ m/s, $c_t = 3110$ m/s and $\rho = 2698$ kg/m^3 (the solid black curve). If the materials were reversed with the same thickness 1 μm, one mode would appear (the broken black curve) at $0 < f < 6$ MHz range of frequencies. For these materials, it is possible to observe the Stoneley wave propagating at the interface [7].

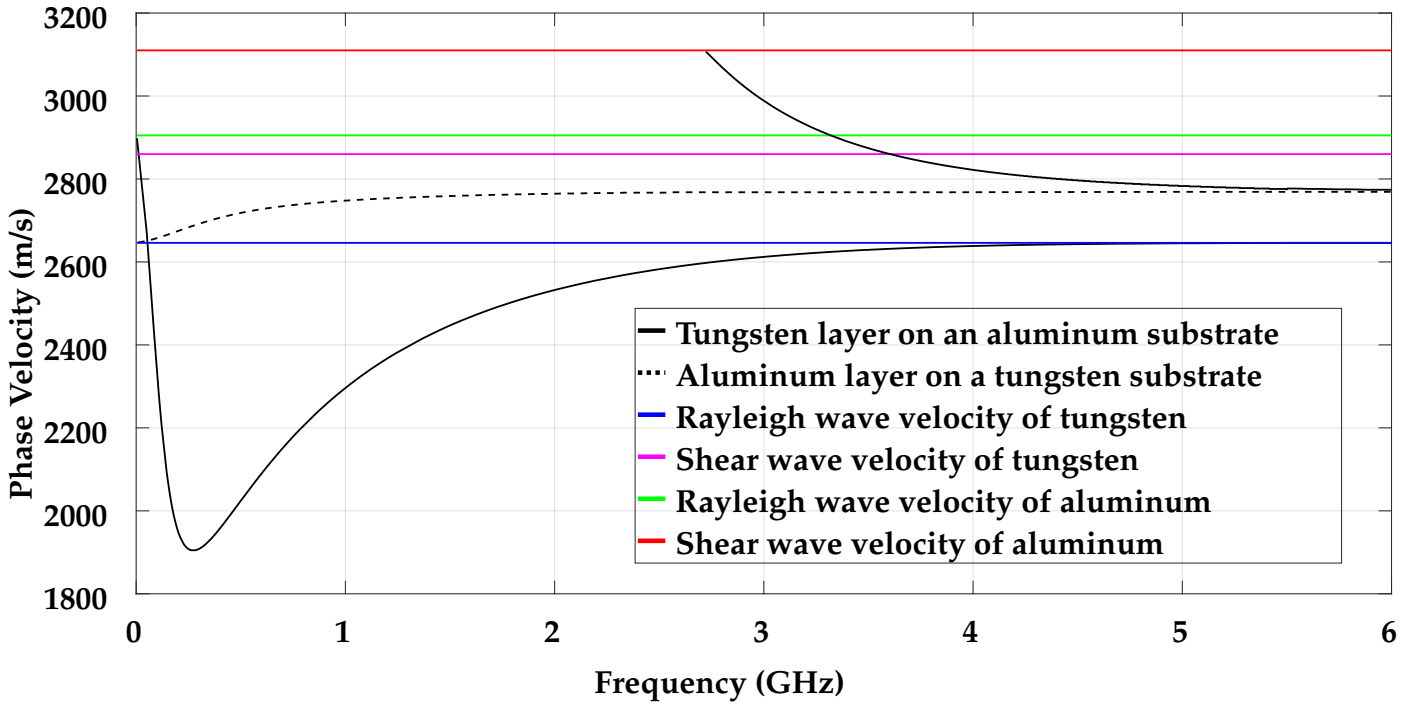

Figure II.9: Rayleigh modes in the intermediate case for a structure composed of 1 μm tungsten layer deposited on an aluminum substrate (solid black) and aluminum on tungsten (dashed black).

In the case where the aluminum layer is deposited on the aluminum substrate, there exist a single Rayleigh mode. This mode starts at the Rayleigh wave velocity of the substrate in the low frequency range (which is the tungsten), as the frequency increases the phase velocity increases and converges towards the Stoneley wave velocity $c_S = 2769$ m/s in the aluminum-tungsten interface [7].

In the case where the tungsten layer is deposited on the aluminum substrate, there exist two Rayleigh modes. At a very low frequency, the first Rayleigh mode has a phase velocity equal to the Rayleigh wave velocity of the substrate and the layer is not effective to the wave propagation. As the frequency increases, the phase velocity of this mode decreases to a certain minimum and then increases such that eventually approaches the velocity of the Rayleigh wave of the layer at a higher frequency. The second Rayleigh mode initially starts at the shear wave velocity of the substrate and then decreases toward the Stoneley wave velocity of this structure.

3.3 Influence of adhesion parameters on SAW dispersion

The previous dispersion relation was evaluated in perfect contact condition. In this section, adhesion parameters (tangential and normal stiffnesses) are included to show the effect of different adhesion strengths on the dispersion curves.

3.3.1 Theoretical analysis of adhesion parameters

The displacement jump model, frequently used in studies on the influence of adhesion in elastic wave propagation in multilayers, demonstrates non-perfect connections between solid layers, resulting in adjusted mechanical stress and particle movement at the layer boundary [16]. Perfect contact, detachment and sliding contact are extreme cases that assume perfect or zero adhesion, while intermediate situations can be represented using this model. The displacement jump model has been extensively studied in many mathematical complexities and different contact conditions can have a significant impact on wave propagation equations [17, 18].

The displacement jump model represents contact conditions at the interface using an infinitesimal intermediate layer, with its properties representing the quality of the interface. Poor adhesion is modeled by a layer with slower propagation speeds and a larger thickness than a layer modeling good adhesion. The basic form of the model replaces boundary conditions with the following expressions:

$$\begin{cases} \sigma_{ij} = \sigma'_{ij} \\ \sigma_{ij} = K_\alpha (u'_i - u_i) \end{cases} \tag{2.60}$$

Here, σ_{ij} and σ'_{ij} represent stress in the first and second mediums, u_i and u'_i are particle displacements in the i direction and K_a is the interface stiffness representing contact quality. $K_a = K_n$ if $i = j$ and $K_a = K_t$ if $i \neq j$. K_n and K_t correspond to normal and tangential stiffnesses respectively.

- Perfect contact condition: $\begin{cases} K_\alpha \to \infty \\ (u'_i - u_i) \to 0 \\ u_i = u'_i \end{cases}$

- Free surface condition: $\begin{cases} K_\alpha \to 0 \\ \sigma_{ij} \to 0 \end{cases}$

- Sliding contact condition: $\begin{cases} K_t \to 0 \\ K_n \to \infty \\ \sigma_{ij} \to 0 \text{ for } i \neq j \\ u_i = u_i' \end{cases}$

Many researchers have examined the modeling of contact conditions using an intermediate layer, starting with Jones and Whittier in 1967 [19], who investigated the propagation of Rayleigh and Stoneley waves at the interface between two media separated by an elastic bond. In this model, they provided the expressions for the tangential stiffness constant, K_t, as $\frac{\mu}{h}$ and the normal stiffness constant, K_n, as $\frac{E}{h}$, where μ, h and E denote the shear modulus (second Lamé coefficient), thickness and Young's modulus of the intermediate layer respectively.

Subsequently, Murty [20] suggested the case of a wave propagating along the interface, applying the displacement jump conditions only to tangential stress and displacement while accounting for a viscous intermediate layer with a complex K_t. In 1980, Schoenberg [21] utilized the displacement jump method to study the effects of a discontinuity at the interface between two solids on reflection and transmission coefficients by examining shear and longitudinal waves. Schoenberg formulated the stiffness constants as follows:

$$\begin{cases} K_n = \frac{(\lambda+2\mu)}{h} = \frac{c_l^2 \rho}{h} \\ K_t = \frac{\mu}{\rho} = \frac{c_t^2 \rho}{h} \end{cases} \tag{2.61}$$

In these expressions, λ represents the first Lamé coefficient of the intermediate layer, ρ denotes its density and c_l and c_t correspond to the longitudinal and shear wave velocities within the layer. The constants K_t and K_n are found in publications that employ the displacement jump model.

3.3.2 Matrix representation of adhesion

We considere a structure composed of n layers and a substrate as in figure II.6. Adding the bond layer, representing the quality of adhesion of various interfaces with an infinitesimal thickness, results in an overall structure of $2n$ layers. Introducing weak normal and tangential stiffnesses is the aim of the characterization of adhesive strength of materials by studying the impact of K_n and K_t on the dispersion curves fitted with the experimental results. The Matrix representation of a bonding layer j is expressed as [13, 14, 16, 4]:

$$[A_j] = \begin{pmatrix} 1 & 0 & \frac{1}{K_{t_j}} & 0 \\ 0 & 1 & 0 & \frac{1}{K_{n_j}} \\ 0 & 0 & 1 & 0 \\ 0 & 0 & 0 & 1 \end{pmatrix} \tag{2.62}$$

Therefore, the matrix of stresses and displacement $[\mathbf{M}]$ can be written as:

$$[\mathbf{M}] = [M_{n+1}(0)]^{-1} \cdot [A_n] \cdot \left([M_n(h_n)][M_n(0)]^{-1}\right) \dots [A_1] \cdot \left([M_1(h_1)][M_1(0)]^{-1}\right) \tag{2.63}$$

3.3.3 Numerical verification

In the case of a single layer on a substrate, the input of the matrices of equation 2.55 in the software is the same, but considering equation 2.63 in single layer case as [4]:

$$[\mathbf{M}] = [M_{\text{Substrate}}(0)]^{-1} \cdot \left[A_{\text{Intermediate Layer}}\right] \cdot \left([M_{\text{Film}}(h_{\text{Film}})][M_{\text{Film}}(0)]^{-1}\right) \tag{2.64}$$

Such that $\left[A_{\text{Intermediate Layer}}\right]$, is the adhesion strength matrix representation according to a chosen K_n and K_t in equation 2.62. Du et al. [12], studied the bonding interface quality of Gold film of thickness 0.5 μm, longitudinal wave velocity $c_l = 3240$ m/s, shear wave velocity $c_t = 1200$ m/s and density $\rho = 19300$ kg/m^3, deposited on a Glass substrate of $c_l = 5130$ m/s, $c_t = 3020$ m/s and

$\rho = 2760\ \mathrm{kg/m^3}$. To verify the developed program using equation 2.64, the same contact conditions of K_n and K_t are indicated in table II.1.

	$\mathbf{K_n}(\times\mathbf{10^{16}N/m^3})$	$\mathbf{K_t}(\times\mathbf{10^{16}N/m^3})$
Perfect bond	∞	∞
Lamb modes	0	0
Level 1	0.84	0.24
Level 2	3.38	0.69
Level 3	13.5	3.84
Level 4	54	15.36
Level 5	216	61.44

Table II.1: Table of stiffness parameters from [12].

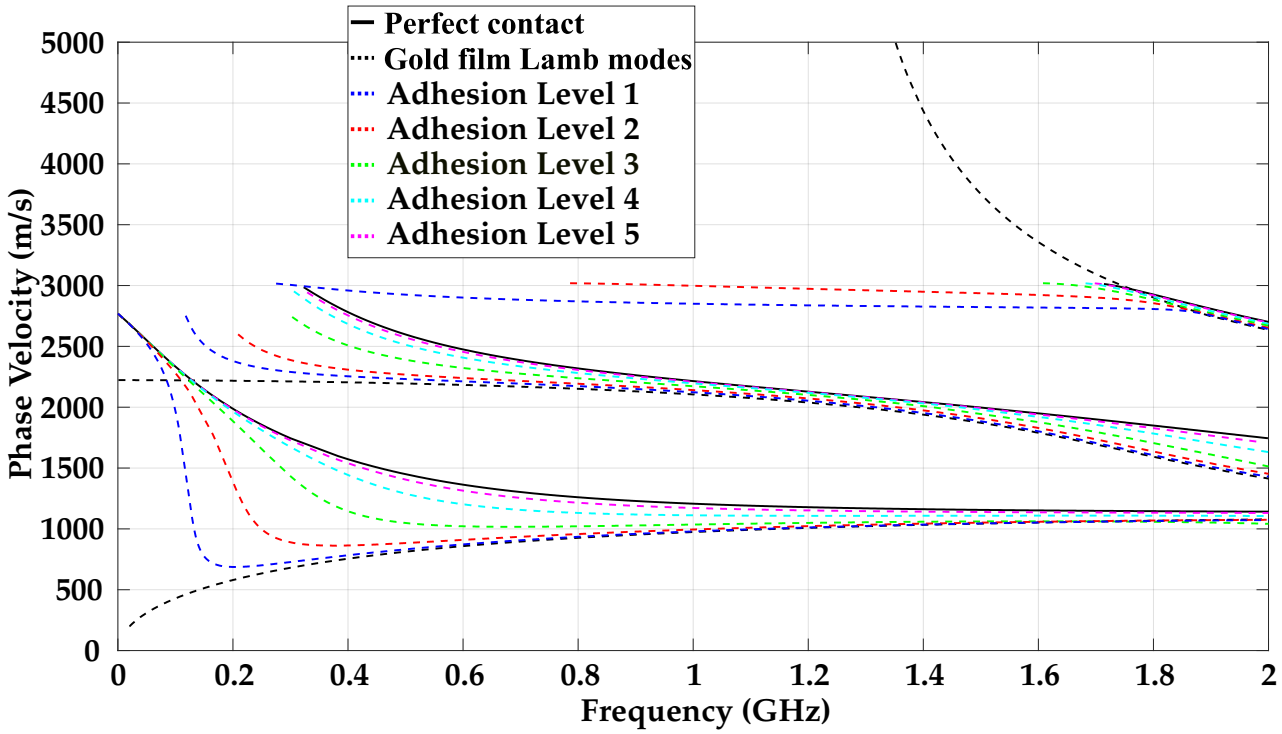

Figure II.10: Surface acoustic waves dispersion curves for different contact conditions for a structure composed of a 0.5 μm gold layer deposited on a glass substrate.

Figure II.10 shows the results of the dispersion curves by the developed program for all adhesion levels. As the stiffnesses, K_n and K_t decrease, surface acoustic wave dispersion curves approach those of the Lamb modes of the layer. This can be an indication of the weaker adhesion between the layer and substrate, making their interaction less significant. With extremely poor adhesion, the wave is no longer influenced by the substrate and behaves like a guided wave in the layer. Additionally, the third Rayleigh mode becomes less dispersive at low frequencies and converges towards the Rayleigh wave velocity of the substrate.

4 SAW dispersion curves of PVC layer on an Aluminum substrate

In this section, we will introduce the dispersion curves of a PVC layer of thickness 215 μm adhering on an Al substrate. Next, a study of varying the adhesion strength K_n and K_t on the dispersion curves will be presented, as well as the sliding boundary condition by fixing K_n and varying K_t and vice-versa to study different cases.

4.1 Perfect contact condition

The PVC layer has a thickness of 215 μm and a density of 1300 kg/m^3 and the aluminum substrate of density 2915 kg/m^3 as presented in table I.3 of Chapter I. Figure II.11, illustrates the "loading" case phase velocity dispersion curves for the surface acoustic waves of the PVC film deposited on an Al substrate at a frequency range from 0 to 6 MHz, as the filter applied to the interferometer in the experiments between 0.2 to 4 MHz to optimize the signal-to-noise ratio of the detected signals.

In the next section, we will introduce a study of the variation of the adhesion parameters K_n and K_t and their influence on the dispersion of the surface acoustic waves.

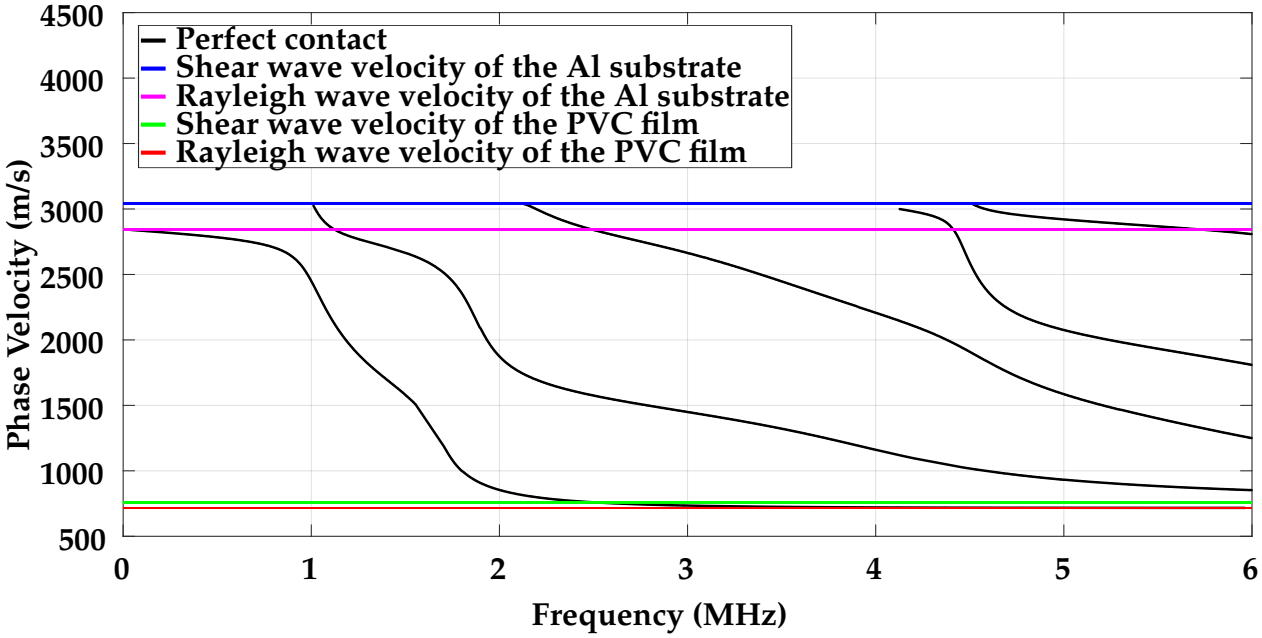

Figure II.11: Perfect contact Rayleigh modes dispersion curves of PVC layer on Al substrate.

4.2 Influence of adhesion parameters on the dispersion curves

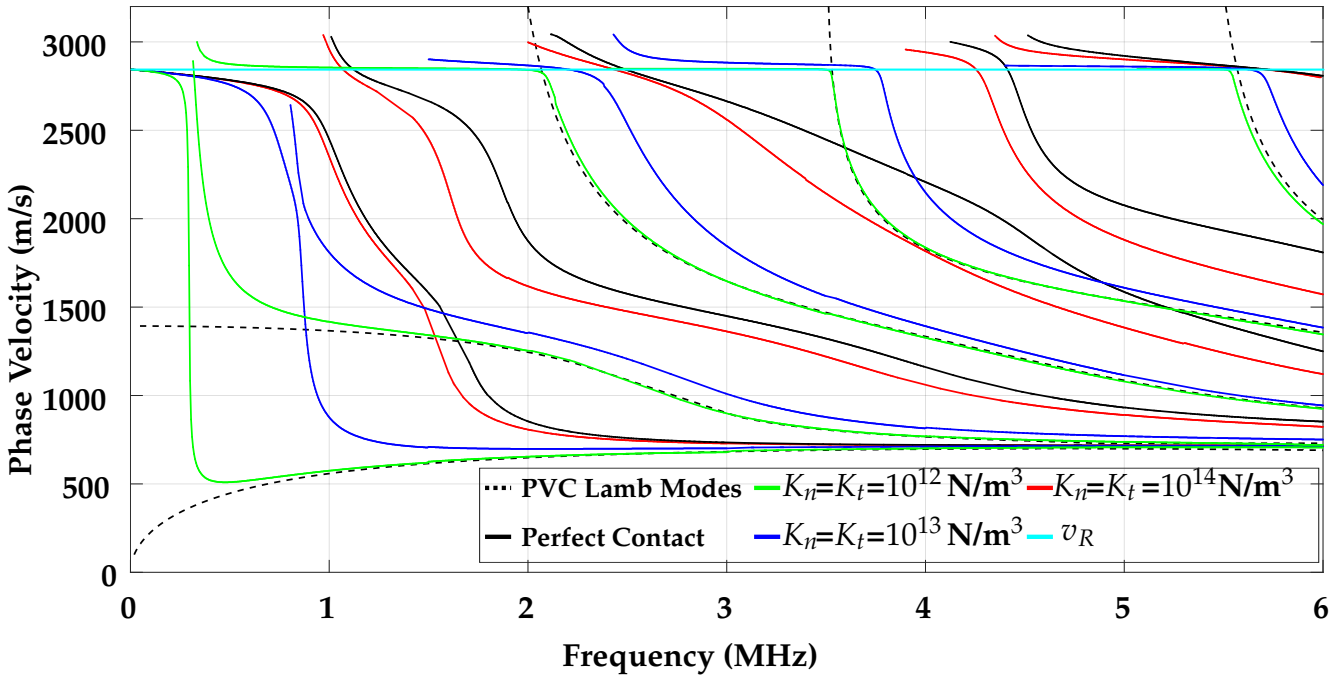

Figure II.12: Effect of K_n and K_t on the dispersion curves of PVC layer on Al substrate.

Figure II.12 demonstrates the influence of K_n and K_t on the dispersion curves. When adhesion is weak ($K_\alpha = 10^{12}$ N/m^3), the modes start by the Rayleigh wave velocity of the Al substrate ($c_R = 2844$ m/s) calculated theoretically [22] and shift towards the Lamb modes of the PVC layer. This occurs when the wavelength is relatively larger than the layer's thickness and the elastic properties of the layer have no effect on Rayleigh wave propagation.

In conditions of high adhesion where $K_\alpha = 10^{14}$ N/m^3, the observed modes converge towards the perfect contact (depicted in black curves). Theoretically, the Rayleigh wave is transferred into Lamb modes guided within the layer.

Figure II.13, shows the effect of the interface stiffness constants K_n and K_t on surface modes for a PVC film on aluminum separately. Initially, K_n is fixed at 10^{16} N/m^3 and K_t is modified, then K_t is fixed at 10^{16} N/m^3 and K_n is varied.

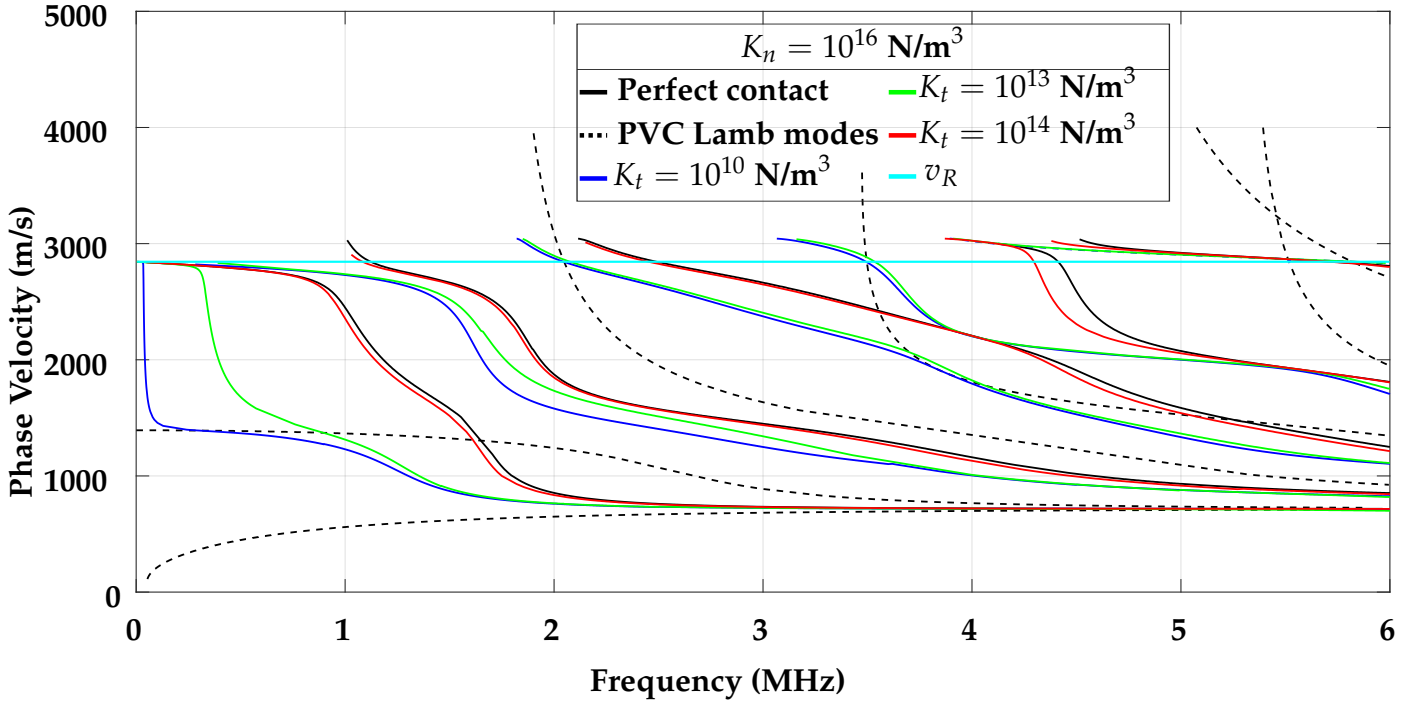

Figure II.13: K_n fixed at 10^{16} N/m^3 and K_t is modified.

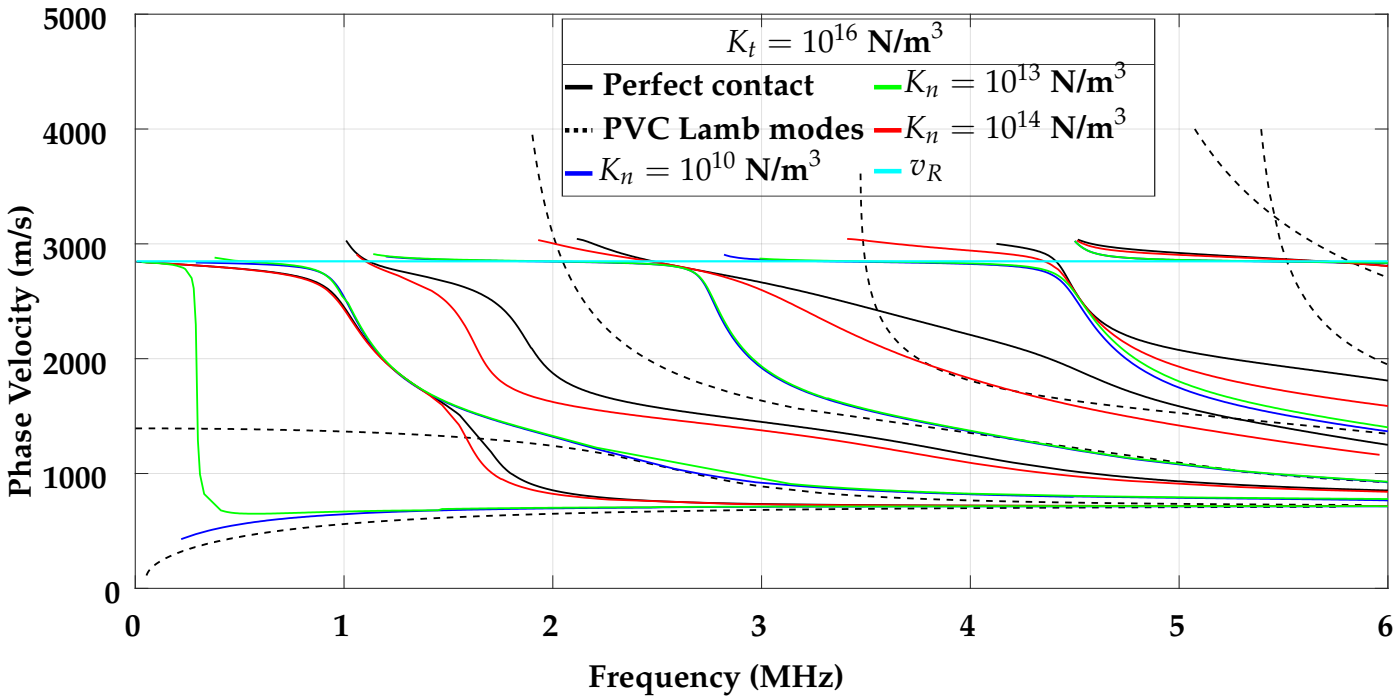

Figure II.14: K_t fixed at 10^{16} N/m^3 and K_n is modified.

Most of the parameters on which the Rayleigh mode dispersion curves in a layer-on-substrate structure depend can thus influence them like a slight variation in adhesion. Poor estimation of one of the parameters can therefore lead to uncertainty in the estimation of interface stiffness from the dispersion curves.

It is possible to locally confuse a variation in adhesion with a poor estimation of the sample characteristics for certain ranges of frequencies and phase velocities.

a) Fixing K_n and varying K_t

When K_n is fixed and K_t is varied, the influence on the Rayleigh modes is different. When K_t is weak, the first mode transforms into the second Lamb mode, while the high-frequency part of this mode tends towards the first Lamb mode of the layer. On the other hand, the second, third and fifth modes show less sensitivity to the lower values of K_t. However, the fourth mode shifts towards the film's fourth Lamb mode of the layer.

b) Fixing K_t and varying K_n

The influence on the modes is evident when K_t is fixed and K_n is modified. As K_n decreases, the modes approach the Rayleigh wave velocity of the substrate and the lamb modes of the film. The first and second Rayleigh modes shift towards the first and second Lamb modes of the layer respectively. Moreover, the third, fourth and fifth Rayleigh modes tend towards the Rayleigh wave speed of the substrate.

4.3 Effect of film's thickness on the dispersion curves

Figure II.15 demonstrates the impact of increasing and decreasing the thickness from $h = h_{\text{PVC}} - 5\ \mu$m to $h = h_{\text{PVC}} + 5\ \mu$m.

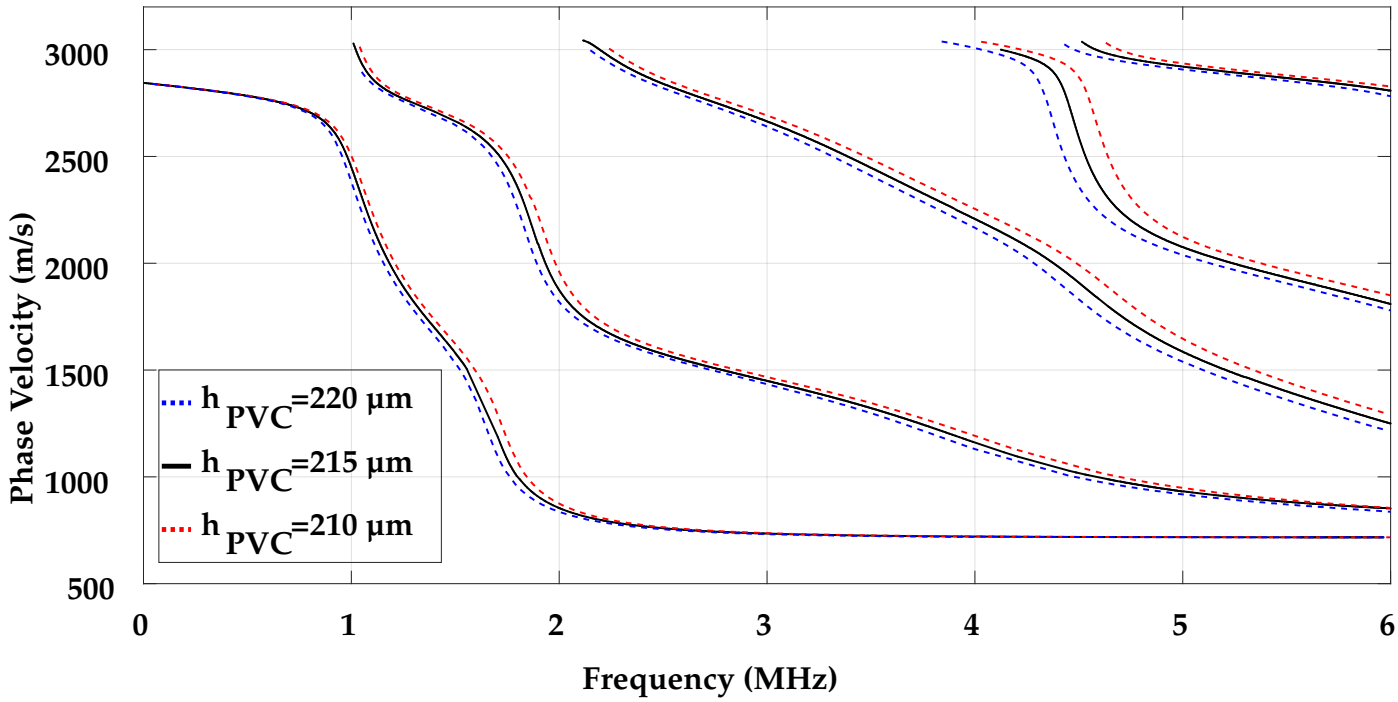

Figure II.15: Effect of thickness on the dispersion curves of surface acoustic waves PVC layer on Al substrate in perfect bonding condition.

As the thickness increases, all modes shift towards lower frequencies. Conversely, when the thickness decreases, the modes shift towards higher frequencies. This variation in the thicknesses shows that it is important to have the most uniform thickness possible of the film during experimental

measurements, as non-uniform thicknesses provide modifications to the dispersion curves leading to complexities in adhesion characterization.

Conclusion

This chapter presented the equations for acoustic wave propagation, focusing on surface acoustic waves. Moreover, the interaction of these waves with a multilayered structure was investigated by the Rayleigh modes dispersion relation. The dispersion curves were generated by a developed program and verified through existing literature results.

Furthermore, we explored the Thomson-Haskell model to understand the impact of adhesion on acoustic wave propagation. By applying this model, we analyzed the influence of the thickness and K_n and K_t parameters on the dispersive behavior of Rayleigh modes for the sample that will be used experimentally.

When adhesion is significantly reduced, Rayleigh modes tend to approach both the Rayleigh wave of the substrate and the Lamb modes of the film. This observation helps in understanding how decayed adhesion affects the behavior of acoustic waves in multilayered structures.

Bibliography of Chapter II

[1] Lev Davidovich Landau et al. *Theory of elasticity: volume 7*. Vol. 7. Elsevier, 1986.

[2] Catherine Potel and Michel Bruneau. "Acoustique générale". In: *chapters* 1 (2006), pp. 3–6.

[3] Eugene Dieulesaint and Daniel Royer. *Ondes élastiques dans les solides-Tome 1: Propagation libre et guidée*. 1996.

[4] Martin Robin. "Contribution à l'étude de l'adhérence des structures du type couche sur substrat par modes de Rayleigh générés et détectés par sources laser". PhD thesis. Université de Valenciennes et du Hainaut-Cambresis, 2019.

[5] Catherine Potel and Michel Bruneau. "Acoustique Générale - équations différentielles et intégrales, solutions en milieux fluide et solide, applications". In: (Jan. 2006).

[6] Daniel Royer and Eugene Dieulesaint. *Elastic waves in solids II: generation, acousto-optic interaction, applications*. Springer Science & Business Media, 1999.

[7] Gerald W Farnell and EL Adler. "Elastic wave propagation in thin layers". In: *Physical acoustics* 9 (2012), pp. 35–127.

[8] Olivier Xeridat. "Etude expérimentale de la propagation, de la diffusion et de la localisation des ondes de Lamb". PhD thesis. Université Nice Sophia Antipolis, 2011.

[9] Lord Rayleigh. "On waves propagated along the plane surface of an elastic solid". In: *Proceedings of the London mathematical Society* 1.1 (1885), pp. 4–11.

[10] Jean-Philippe Groby. "Modélisation de la propagation des ondes élastiques générées par un séisme proche ou éloigné à l'intérieur d'une ville". PhD thesis. Université de la Méditerranée-Aix-Marseille II, 2005.

[11] Francesco Lanza di Scalea, Piervincenzo Rizzo, and Alessandro Marzani. "Propagation of ultrasonic guided waves in lap-shear adhesive joints: case of incident A 0 Lamb wave". In: *The Journal of the Acoustical Society of America* 115.1 (2004), pp. 146–156.

[12] Jikai Du, Bernhard R Tittmann, and Hyeong Sick Ju. "Evaluation of film adhesion to substrates by means of surface acoustic wave dispersion". In: *Thin Solid Films* 518.20 (2010), pp. 5786–5795.

[13] T Thomson William. "Transmission of Elastic Waves through a Stratified Solid Medium". In: *Journal of Applied Physics* 21.2 (1950), pp. 89–93.

[14] Norman Abraham Haskell. *Vincit Veritas: A Portrait of the Life and Work of Norman Abraham Haskell, 1905-1970*. American Geophysical Union, 1990.

[15] HF Tiersten. "Elastic surface waves guided by thin films". In: *Journal of Applied Physics* 40.2 (1969), pp. 770–789.

[16] SI Rokhlin and YJ Wang. "Analysis of boundary conditions for elastic wave interaction with an interface between two solids". In: *The Journal of the Acoustical Society of America* 89.2 (1991), pp. 503–515.

[17] Mohammadi Ouaftouh. "Modélisation de la propagation ultrasonore au niveau de joints collés: Application au contrôle de la qualité d'adhérence". PhD thesis. Valenciennes, 1990.

[18] Nicolas Collier. "Développement d'un outil ultrasonore de caractérisation des propriétés d'adhésion de milieux modèles avec application aux dépôts laitiers". PhD thesis. Lille 1, 2014.

[19] JP Jones and JS Whittier. "Waves at a flexibly bonded interface". In: (1967).

[20] GS1880195 Murty. "A theoretical model for the attenuation and dispersion of Stoneley waves at the loosely bonded interface of elastic half spaces". In: *Physics of the Earth and Planetary Interiors* 11.1 (1975), pp. 65–79.

[21] Michael Schoenberg. "Elastic wave behavior across linear slip interfaces". In: *The Journal of the Acoustical Society of America* 68.5 (1980), pp. 1516–1521.

[22] Igor Aleksandrovich Viktorov. "Rayleigh and Lamb waves". In: *Rayleigh and Lamb Waves* (1967), p. 33.

Chapter III

Studying the influence of adhesion strength by finite element modeling

Introduction

The Finite Element Method (FEM) is employed in the following for detailed modeling and understanding of wave propagation and interaction at the interface of a layer on a substrate structure, which is essential in studying the quality of adhesion by ultrasonic waves and optimizing the performance of a coating.

Indeed, surface acoustic waves are sensitive to various factors when propagating through a film on a substrate structure, such as the thickness of the film and its adhesion strength denoted by the normal and tangential stiffnesses K_n and K_t along the interface. The uniform thickness of the film in the simulation allows the study of the adhesion strength assuming homogeneity along the interface. Conversely, the adhesion area itself is another crucial factor. This factor depends on the areas where the coating adheres strongly, in contrast with other areas that exhibit weak adhesion. In situations where adhesion strength is not homogeneous, obtaining accurate K_n and K_t values with respect to the theoretical calculation becomes challenging.

In this chapter, we will present the finite element modeling, through three sections. The first part

will explain the modeling process and the parameters considered, as the accuracy of our simulation greatly depends on the validity of these parameters. The second one will study the influence of adhesion strength on the dispersion curves of the considered sample and will present the comparisons of the model to the theoretical computations. The final part will display the study of the adhesion area on surface acoustic wave dispersion through the interface, using the continuous wavelet transform on the signal.

1 Introducing the finite element modeling

It is necessary to consider an infinitesimal intermediate layer that has the parameters relevant to the theoretical characteristics of adhesion. Accordingly, a two-dimensional setup within the plane strain structural mechanics model is sufficient for an accurate representation.

1.1 Meshing and parameter justification

a) Parameters and geometry of the FEM

As mentioned previously, the substrate is a square-shaped block of aluminum, which measures 4.4 $\pm$ 0.05 cm in height and 9.8 $\pm$ 0.05 cm in length and width. Moreover, the PVC layer measured has a thickness of $h_{\mathrm{PVC}} = 215 \pm 5$ μm and a width of 17 mm. The dimensions of the subdomains chosen for the finite element model are summarized in table III.1. Figure III.1 displays the geometry of the model.

Material (Subdomain)	**Width (mm)**	**Thickness (μm)**	**Maximum Element Size (μm)**
Polyvinyl chloride	15.1	215	10
Intermediate layer	15.1	0.1	10
Aluminum	17.1	500	10
Perfectly Matched Layer	-	-	Coarse Mesh

Table III.1: Parameters for each subdomain in the model.

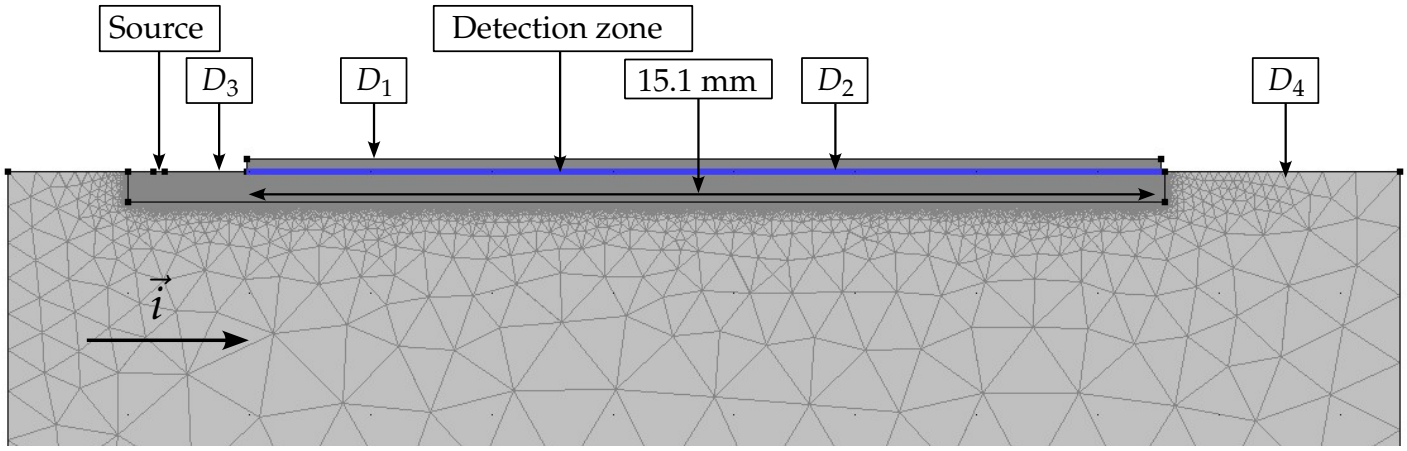

Figure III.1: Geometry of the finite element modeling.

b) Characteristics of the subdomains

In this model, the PVC film is depicted by the subdomain D_1, which measures 15.1 mm in length and 215 μm in thickness. The intermediate layer is represented by the subdomain D_2 in the model, has the same length as the PVC layer (15.1 mm) and has a thickness of $h_0 = 0.1$ μm (that is less than 0.1% of h_{PVC}). The aluminum substrate is characterized by D_3 and D_4 subdomains. The subdomain D_3 extends over 17.1 mm in length and has a thickness of 0.5 mm. Whereas the subdomain D_4 incorporates Rayleigh-type damping to establish a Perfectly Matched Layer (PML), minimizing the acoustic wave reflections at the boundaries of the structure [1]. Finally, the detection zone is represented by 251 blue dots which record the normal displacements on the surface of the substrate along

the interface.

To justify the selected values, it is important to mention that focusing on a segment where the Rayleigh wave is generated and where the influence of the interface on its propagation can be observed is sufficient and reduces the modeling time. Additionally, while the length of D_3 could be set to 17 mm, the 0.1 mm is included to facilitate signal detection on the aluminum surface on the opposite side of the generation point, when required. Moreover, the 15.1 mm of subdomain D_1 is selected based on the number of the detection points (251 points) and the separation distance between them ($d_x = 60$ μm) forming a length of $(251-1) \times d_x = 15$ mm and this subdomain is also extended by 0.1 mm to ensure that all detection points are within the interface area, avoiding the edges of the PVC layer.

Additionally, the intermediate layer has a density of $\rho_0 = 130$ kg/m^3, which is 10% of the density of PVC according to analyses by Du et al. [2]. The adhesion characteristics can be modified by adjusting the Young's modulus (E_0) of the intermediate layer. This control is linked to the adhesive stiffnesses K_n and K_t, as defined by the equation below [3]:

$$\begin{cases} K_n = \frac{1}{h_0} \frac{E_0(1-v_0)}{(1+v_0)(1-2v_0)} \\ K_t = \frac{1}{h_0} \frac{E_0}{2(1+v_0)} \end{cases} \tag{3.1}$$

Featuring a rigid intermediate layer, the Poisson's ratio is assumed to be $\nu_0 = 0$. However, this value can be later modified according to the experimental measurements and the relation between K_n and K_t.

c) Laser pulse modeling

To model laser pulse excitation, two points are created with 200 μm apart, corresponding to the width of the linear laser source. This excitation source is loaded through a dipole force mechanism, based on the surface center of expansion (SCOE) by Rose for metallic materials [4]. The load force is proportional to the function $F(t)$ in equation 3.2 in the thermoelastic regime, characterized by a full-width half maximum (FWHM) of 25 ns and τ representing the time to reach the peak amplitude,

as discussed by Dai et al. [5]. The direction of the applied loads to the first and second points are $-F(t)\vec{i}$ and $+F(t)\vec{i}$, respectively, where $\pm\vec{i}$ denotes the direction of the unit vector $\vec{i}$ along the surface of the substrate [6].

$$F(t) = \frac{t}{\tau^2} \exp\left(\frac{-t}{\tau}\right) \cdot H(t) \tag{3.2}$$

Where $H(t)$ corresponds to the Heaviside function. Figure III.2 is a scheme illustrating modeled laser pulse generating elastic waves on a sample.

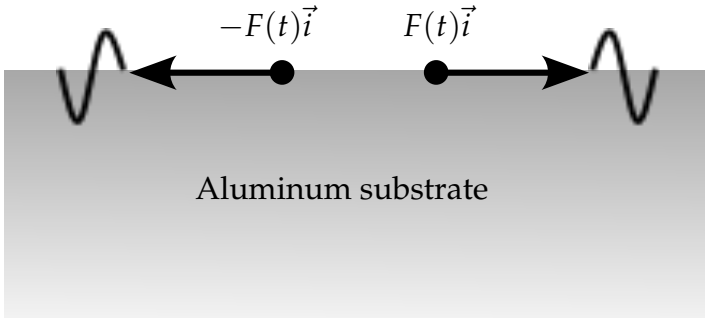

Figure III.2: Scheme explaining the simulation of the laser pulse.

d) Meshing and time increment conditions

Selecting appropriate values for the time step (Δt) allows more detailed time resolution of wave propagation. Moreover, it is important to accurately model the fast-changing dynamics of high-frequency wave propagation by relatively reducing Δt.

Similarly, the maximum element size (Δx) is important for the spatial resolution of the mesh used in the modeling. A smaller Δx results in more accurate simulations up to a specific limit, on the other hand, it also results in increasing the number of computations thus the time cost.

Equation. 3.3 shows the conditions for selecting the appropriate values of the time increment and the maximum element size. Assuming a maximum frequency $f_{max} = 6$ MHz, i.e a minimum wavelength $\lambda_{min} = 474$ μm for a Rayleigh wave velocity of $c_R = 2844$ m/s for an aluminum substrate, the selected element size is then $\Delta x = 10$ μm limited to 23.7 μm and remains uniform in the domains of interest. Moreover, the selected time step is then $\Delta t = 4$ ns [6, 7].

Additionally, a coarse mesh is applied to the PML as it does not require the same spatial resolution of the wave propagation in the area of interest, based on the observation (after several attempts) of the wave attenuation in the defined PML subdomain.

$$\begin{cases} \Delta t < \frac{1}{20 f_{max}} \\ \Delta x < \frac{\lambda_{min}}{20} \end{cases} \tag{3.3}$$

1.2 Fundamentals and computational approaches in solid mechanics

In the study of plain strain solid mechanics, the propagation equation (equation 2.5) is used to calculate the displacements within a material. This fundamental equation ensures that the mass times acceleration of a material point equals the sum of internal and external forces acting upon it.

a) Total stress

To comprehensively account for different sources of stress, the total stress equation is used:

$$S_{ad} = S_0 + S_{ext} + S_q \tag{3.4}$$

Such that, S_{ad} is the additional stress tensor, S_0 is the initial stress tensor, S_{ext} includes external stress contributions, and S_q holds other stress factors such as thermal effects. The software sums these components to derive the total additional stress tensor at each point in the mesh.

In our model, S_0 is zero since no stress is applied initially. S_{ext} accounts for external forces applied during the simulation, and S_q includes thermal stress calculated based on temperature distributions within the materials and is expressed as:

$$S_q = \alpha \cdot \Delta T \cdot C \tag{3.5}$$

where α the coefficient of thermal expansion and ΔT the temperature change are both constants and C is the elasticity tensor.

b) Elastic and inelastic strain

The total strain in the material is decomposed into elastic and inelastic components expressed as:

$$\varepsilon = \varepsilon_{el} + \varepsilon_{inel} \tag{3.6}$$

Where, ε represents the total strain tensor, ε_{el} is the elastic strain tensor, and ε_{inel} denotes the inelastic strain tensor. The software calculates the total strain by adding the elastic and inelastic strains, where the elastic strain is derived from the displacement field and the inelastic strain is defined based on material models.

In our case, ε_{el} is derived from the normal displacement field and ε_{inel} is constant such that it includes the thermal strain based on the coefficient of thermal expansion and the temperature change.

c) Strain-displacement relation

The relation between strain and displacement is described by:

$$\varepsilon = \frac{1}{2}\left((\nabla \vec{u})^T + \nabla \vec{u}\right) \tag{3.7}$$

where ε is the strain tensor, $\vec{u}$ is the displacement vector, and $\nabla \vec{u}$ is the displacement gradient tensor (first spatial derivative of displacement). This equation ensures that the strain is symmetric and describes the material deformation.

d) Elasticity tensor

The elasticity tensor, which characterizes the material's response to deformation, is given by:

$$C = C(\varepsilon, \nu) \tag{3.8}$$

where C is the elasticity tensor, ε is the strain tensor, and ν is Poisson's ratio. The software calculates this tensor based on the material properties and the strain tensor at each point in the mesh.

1.3 Elastic parameters of materials

The input parameters included in the modeling are Young's modulus E, density ρ and Poisson's ratio ν for each material. These parameters determine the mechanical behavior under different loads and stresses.

To include these parameters into the model, the values of E and ν of the aluminum substrate and PVC film are calculated using equation 3.9 [8].

$$E = \rho \cdot c_t^2 \cdot \left(\frac{3c_l^2 - 4c_t^2}{c_l^2 - c_t^2} \right) \qquad \text{and} \qquad \nu = \frac{c_l^2 - 2c_t^2}{2\left(c_l^2 - c_t^2\right)} \tag{3.9}$$

Where c_l and c_t, are the longitudinal and shear wave velocities. Table III.2 recalls the parameters from table I.3 of Chapter I (highlighted in blue) and the corresponding calculated Young's modulus and Poisson ratios for the materials.

Material	$\rho\ (kg/m^3)$	$c_l\ (m/s)$	$c_t\ (m/s)$	$E\ (GPa)$	ν
Polyvinyl chloride (PVC)	1300	1900	760	2.11	0.40
Aluminum (Al)	2915	6276	3044	72.72	0.35

Table III.2: Young's modulus and Poisson's ratio calculated for PVC and aluminum.

By referring to the study of the effect of K_n and K_t parameters on the dispersion curves of Chapter II, we can then consider the perfect contact condition is at $K_n = 2 \times 10^{16}$ N/m^3 and $K_t = 10^{16}$ N/m^3, corresponding to the Young's modulus of $E_0 = 2$ GPa selected for the intermediate layer from equation 3.1. The results of the simulation at this value are presented in the next section, which corresponds to the perfect contact condition.

1.4 Simulation of acoustic wave propagation

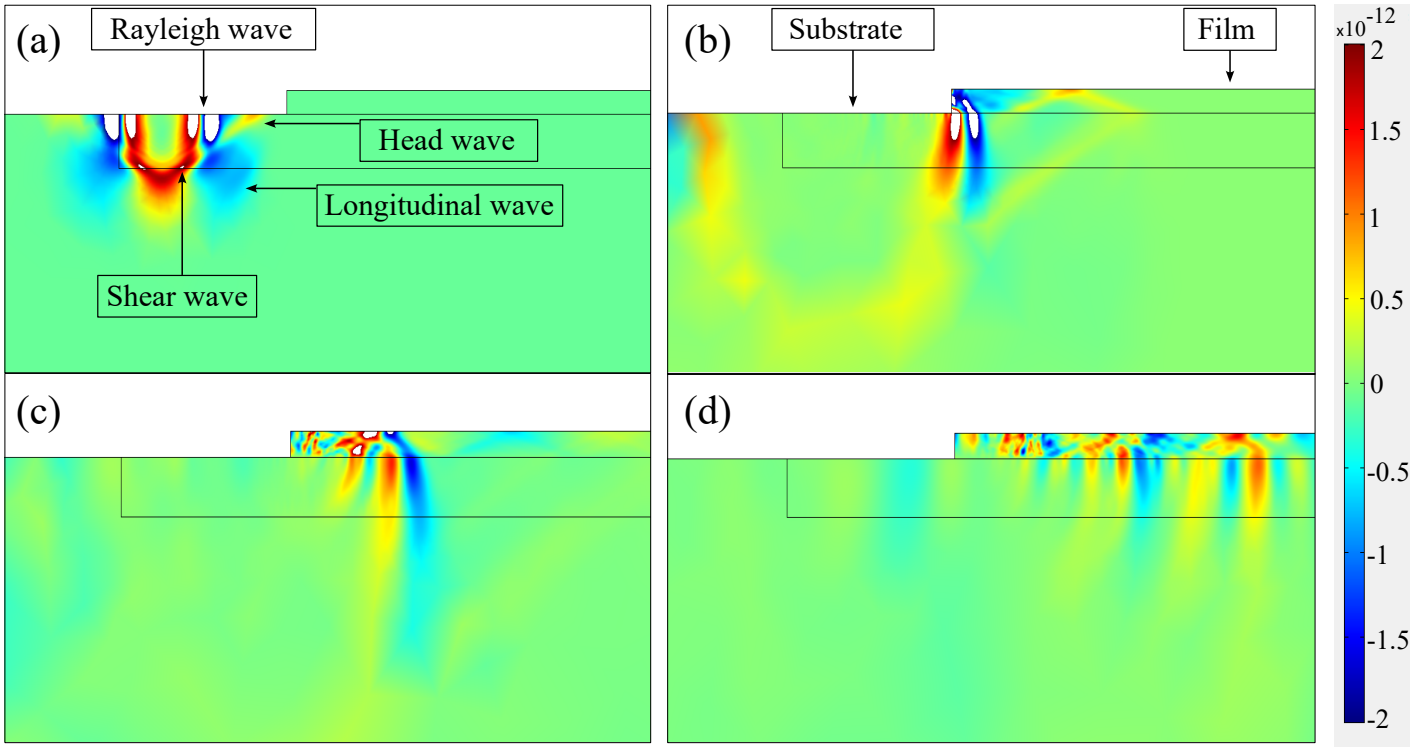

Figure III.3: Acoustic waves propagating through the structure at different times: $t = 0.2\ \mu s$ (a), $t = 0.6\ \mu s$ (b), $t = 1\ \mu s$ (c) and $t = 2\ \mu s$ (d).

Figure III.3 shows the simulated elastic waves in a 2D amplitude plot over different times of flight, with amplitude variation according to a fixed maximum and minimum color scale. Initially, at $t = 0.2\ \mu$s (a), the impact of the applied force displays the generation of the longitudinal, shear, head and Rayleigh waves within the thermoelastic regime on the aluminum substrate. By $t = 0.6\ \mu$s (b), these elastic waves start to attenuate when propagating in the PML, whereas the surface acoustic waves undergo reflections when interacting with the film leading to guided waves. Progressing to $t = 1\ \mu$s (c), the dispersion of the surface acoustic wave is observed at the interface, which is further improved by $t = 2\ \mu$s (d) as the waves continue to propagate.

The detection zone is composed of 251 virtual probes spaced by $d_x = 60\ \mu\text{m} << \lambda_{\text{min}}$. Figure III.4 displays the normal displacement of 32 signals selected out of the 251 by the 8^{th} signal of the virtual probes. The initial signal (black) illustrates the Rayleigh wave in the aluminum substrate.

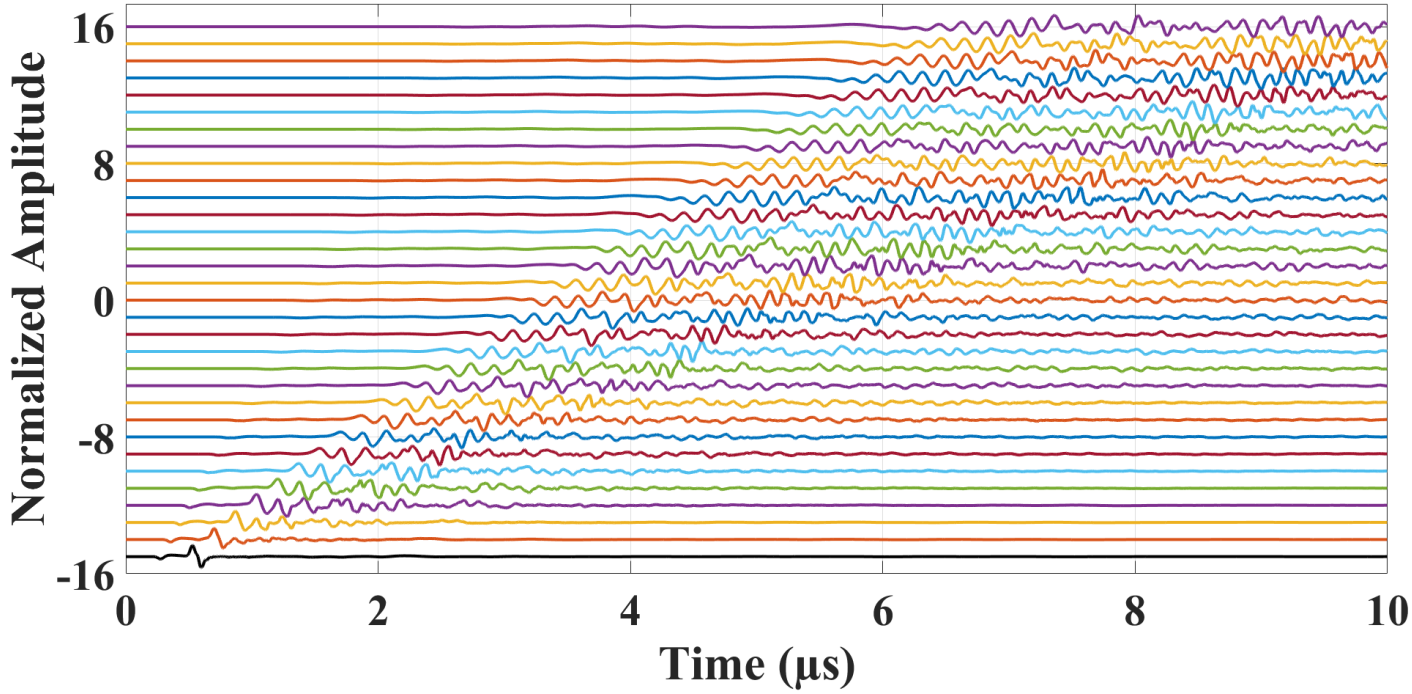

Figure III.4: Representation of 32 signals obtained from the blue virtual probes.

Signals in figure III.4 present the influence of the interaction of the surface acoustic wave propagation with the layer in perfect contact adhesion condition, showing an increase in the dispersion with wave propagation at the interface. This implies that a larger distance of surface acoustic wave propagation at the interface results in a more significant dispersion due to the increase of the reflections within the boundaries of the film.

The two-dimensional Fourier transform (2DFFT) is used to verify the simulation that models the influence of adhesion on the propagation of surface acoustic waves. This technique allows the derivation of the dispersion curves in the wavenumber-frequency domain when applied to the detected signals. The mathematical formulation of the 2DFFT is given by:

$$S(k_x, f) = \int_{-\infty}^{\infty} \int_{-\infty}^{\infty} s(x,t) e^{-j(2\pi k_x x + 2\pi f t)} \, dx \, dt \tag{3.10}$$

where $s(x,t)$ is the time-space data, k_x is the wavenumber, and f is the frequency. The resulting $S(k_x, f)$ provides a plot of the dispersion curves $f(k)$ and how the phase velocities $V_p(f) = \frac{2\pi f}{k}$ of the waves vary with frequency.

The 2DFFT allows to reveal the detailed dispersion characteristics of the material under investigation. By transforming the time-domain signals into the frequency-wavenumber domain, we can analyze the impact of the layer's elastic properties on wave propagation.

This approach has advantages in non-destructive testing with its ability to show the dispersion characteristics (loading, stiffening, or intermediate case) of surface modes for the structure under investigation. Figure III.5 presents the results of this transformation.

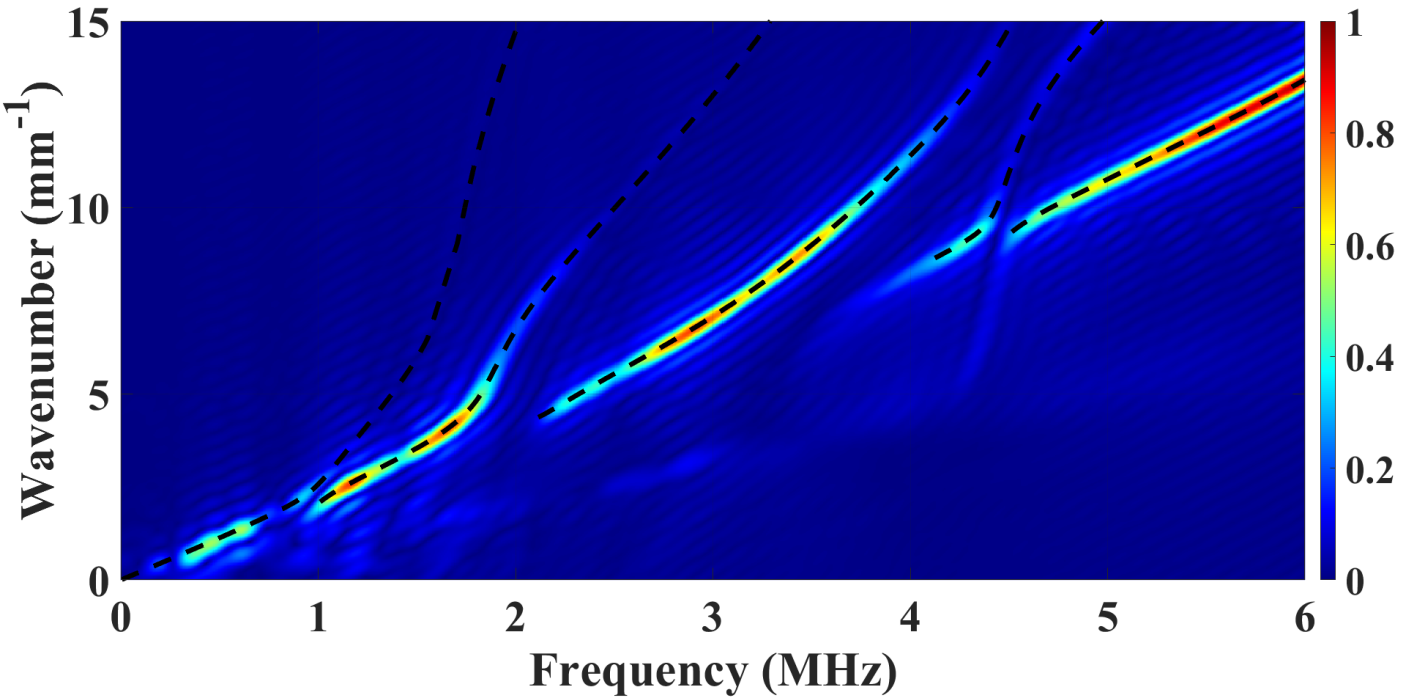

Figure III.5: Wavenumber-frequency diagram from the model and the theoretical dispersion dashed curves in perfect contact condition.

The spectral amplitudes of the modes in figure III.5 are normalized and correspond to the color bar, showing high amplitudes at specific wavenumber-frequency values where the surface modes exist. The results show five distinct modes in the frequency range ($0 \leq f \leq 6$ MHz) where the first and the fourth modes have weak amplitude and are difficult to distinguish without the verification of the theoretical ones (dashed curves). However, the second, third and fifth modes are visible and reach up to a certain part of the theoretical ones at a specific range of frequency.

After tracking the maximum amplitudes at each frequency value, we can plot the phase velocity dispersion curves obtained from the model. Figure III.6 displays the phase velocities determined at

the peak amplitudes for each frequency value of the modes identified in the wavenumber-frequency domain.

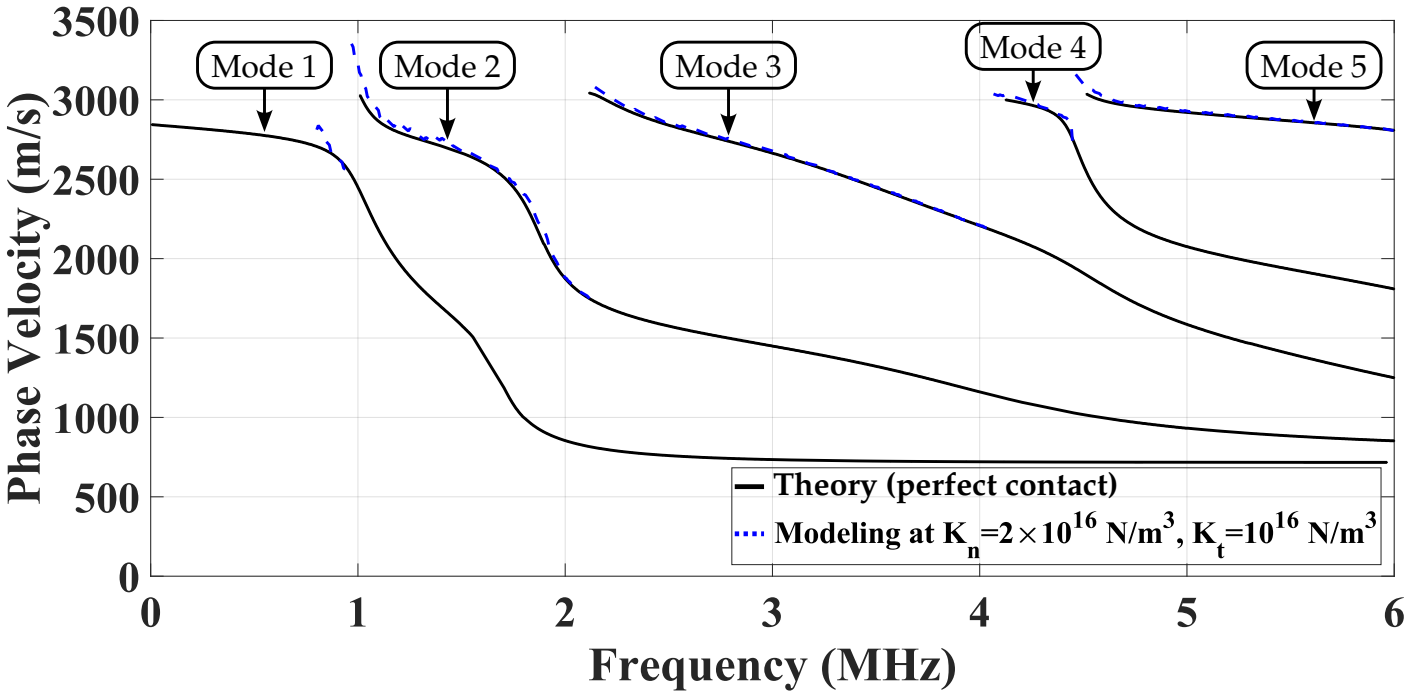

Figure III.6: Phase velocity dispersion curves obtained from the model with theoretical verification.

The first and fourth modes show low resolution and complicate the determination of the impact of adhesion quality on these modes. However, the second, third and fifth modes, characterized by their high resolution and spectral amplitudes facilitate the ability to distinguish experimentally the effect of adhesion quality on these modes. In the next section, we will investigate the influence of the adhesion strength on the dispersion curves of surface modes.

2 Studying the uniform adhesion quality

In this section, we will present the effect of the adhesion strength on the dispersion of the surface acoustic waves. This study is divided in two parts: the first part presents the influence of the uniform adhesion strength on the surface acoustic wave propagation showing the frequency distribution of the signal in a scalogram for each adhesion level. In the second part, we will discuss the dispersion curves for each adhesion level associated with their corresponding signals obtained in the first part.

2.1 Influence of adhesion on surface acoustic wave propagation

Different adhesion levels can be obtained by varying the value of Young's modulus of the intermediate layer which corresponds to specific values of K_n and K_t as expressed previously. The simulated values are presented in table III.3.

E_0 (MPa)	0.1	1	10	100	1000
K_n (N/m^3)	10^{12}	10^{13}	10^{14}	10^{15}	10^{16}
K_t (N/m^3)	5×10^{11}	5×10^{12}	5×10^{13}	5×10^{14}	5×10^{15}

Table III.3: Stiffness coefficients K_n and K_t for different values of Young's modulus.

We have previously shown in Chapter II, that values of K_n and K_t in the order of $\leq 10^{12}$ N/m^3 are considered weak adhesion. Whereas a values of $\geq 10^{15}$ N/m^3 are considered good adhesion.

Figure III.7 clarifies the aim of the study, where the two black points represent the laser pulse source by loading $-F(t)\vec{i}$ on the first point and $+F(t)\vec{i}$ on the second one. The blue dots represent the virtual probes where the detection occurs on the substrate's interface and the last red point is the virtual probe at which the surface acoustic wave signal that passes through the film is detected on the substrate surface. The intermediate layer shows the adhesion parameters related to Young's modulus for the chosen value of Poisson's ratio $\nu_0 = 0$, representing a non-deformable layer. The aim is to display the detected signal at the red virtual probe and its frequency distribution over time, then to show the dispersion curves associated to this signal.

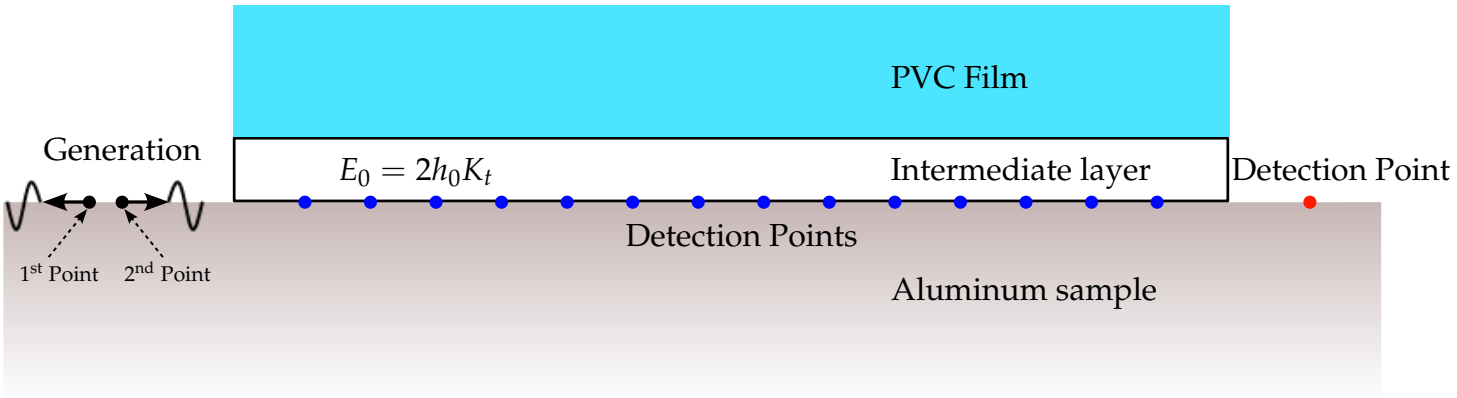

Figure III.7: Uniform adhesion illustrated in the intermediate layer and used in the model.

Figure III.8 illustrates the signals detected at the red point for different adhesion levels. A low-pass filter of 4 MHz cut-off frequency was applied to these signals in order to approach the experimentally detected ones. These signals show that a higher adhesion strength increases the dispersion of the surface acoustic wave to a certain limit (the perfect contact condition).

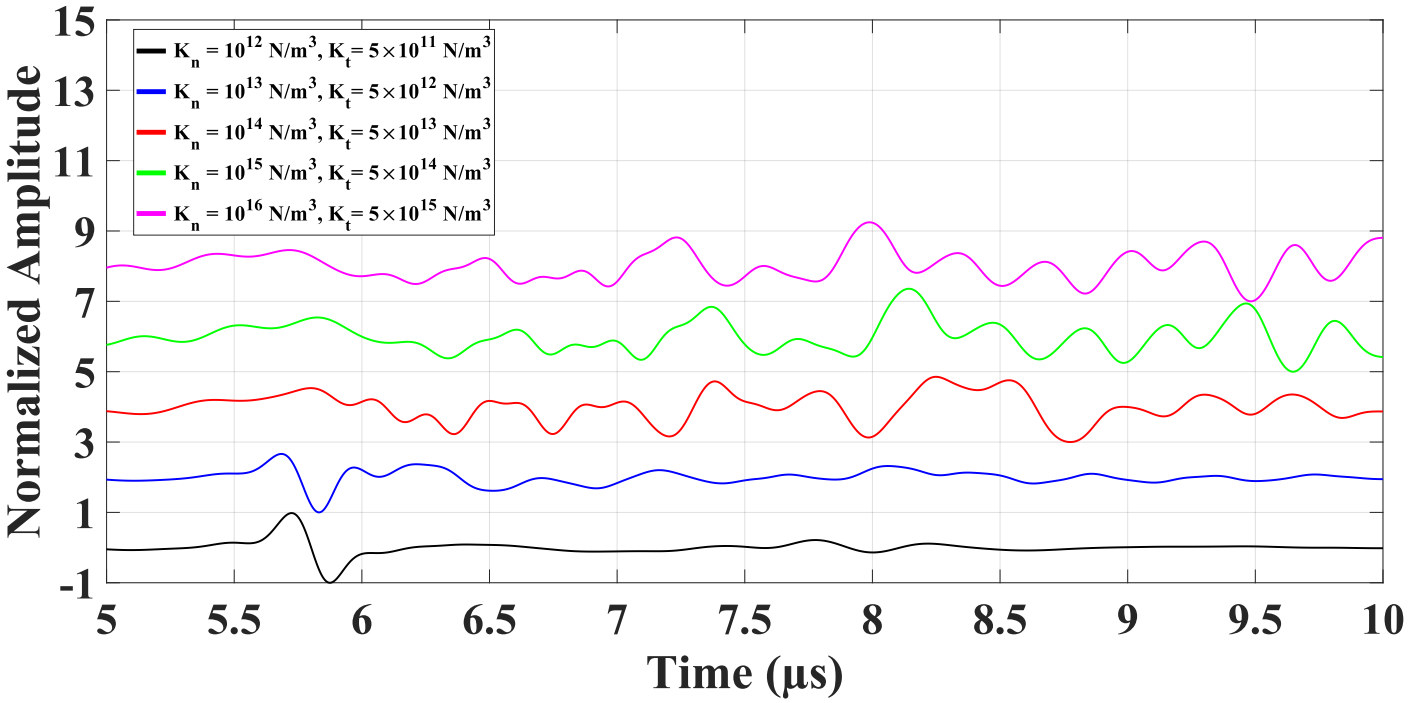

Figure III.8: Signals obtained at the red virtual probe with different adhesion parameters.

2.2 Frequency-time analysis of the signals

Figure III.9 represents the Fourier transform of the signals detected at the red point for this study.

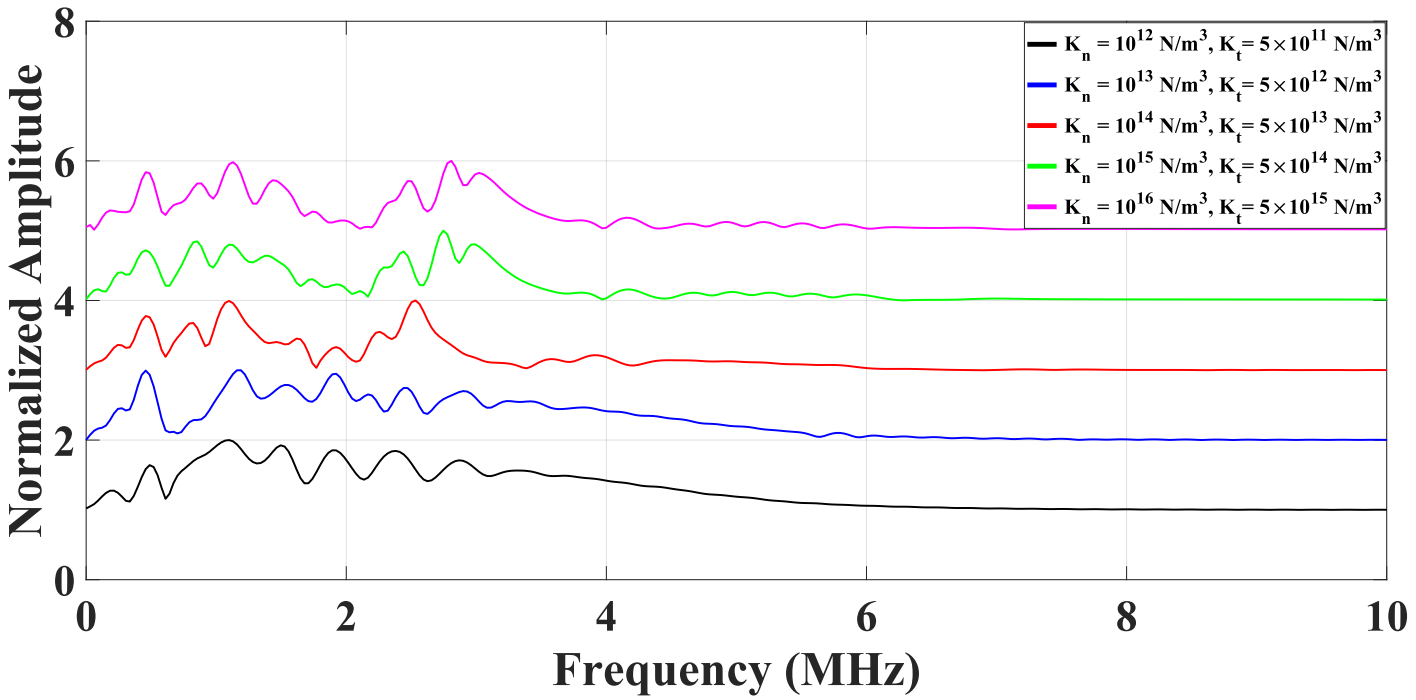

Figure III.9: Spectrum of the signals obtained at the red virtual probe with different adhesion parameters.

The black and blue curves represent the spectra at low adhesion values ($K_t = 5 \times 10^{11}$ N/m^3 and $K_t = 5 \times 10^{12}$ N/m^3, respectively). These spectra have overlapping peaks in the frequency range of $1 - 3.5$ MHz. The red, green, and magenta curves represent the spectra at higher adhesion values ($K_t = 5 \times 10^{13}$ N/m^3, $K_t = 5 \times 10^{14}$ N/m^3, and $K_t = 5 \times 10^{15}$ N/m^3, respectively). The peaks of these spectra become more separated. Moreover, these spectra are observed in a lower frequency range of $0.4 - 2.8$ MHz. The maximum normalized amplitudes shift to lower frequencies, indicating a change in the surface mode behavior.

The separation of the peaks in the spectra at higher adhesion values suggests the presence of multiple surface modes. To observe the dispersive nature of surface acoustic wave propagation, the continuous wavelet transform is performed using the Morlet mother wavelet expressed in equation 3.11 showing the frequency distribution over time of the signals [9, 10].

The Morlet mother wavelet is chosen for the continuous wavelet transform (CWT) due to its superior time-frequency localization properties. The mathematical definition of the Morlet wavelet, $\mathrm{Mor}(t) = \frac{1}{\sqrt{\pi}} \exp(-t^2) \cdot \exp(2\pi i t)$, shows that it consists of a Gaussian window modulating a complex exponential function. This structure ensures good time localization and frequency localization, making it ideal for analyzing signals with varying frequency content over time. The characteristics of the Morlet wavelet, as illustrated in Figure 4.26, show that it can capture both the amplitude and phase information of the signal, which is crucial for detailed signal analysis. Additionally, its widespread usage in signal processing underscores its reliability and versatility. Therefore, the Morlet wavelet is an optimal choice for analyzing the frequency distribution of signals.

$$\psi(t) = \frac{1}{\sqrt{\pi}} e^{-t^2} e^{2i\pi t} \tag{3.11}$$

Figure III.10 illustrates the characteristics of the Morlet wavelet.

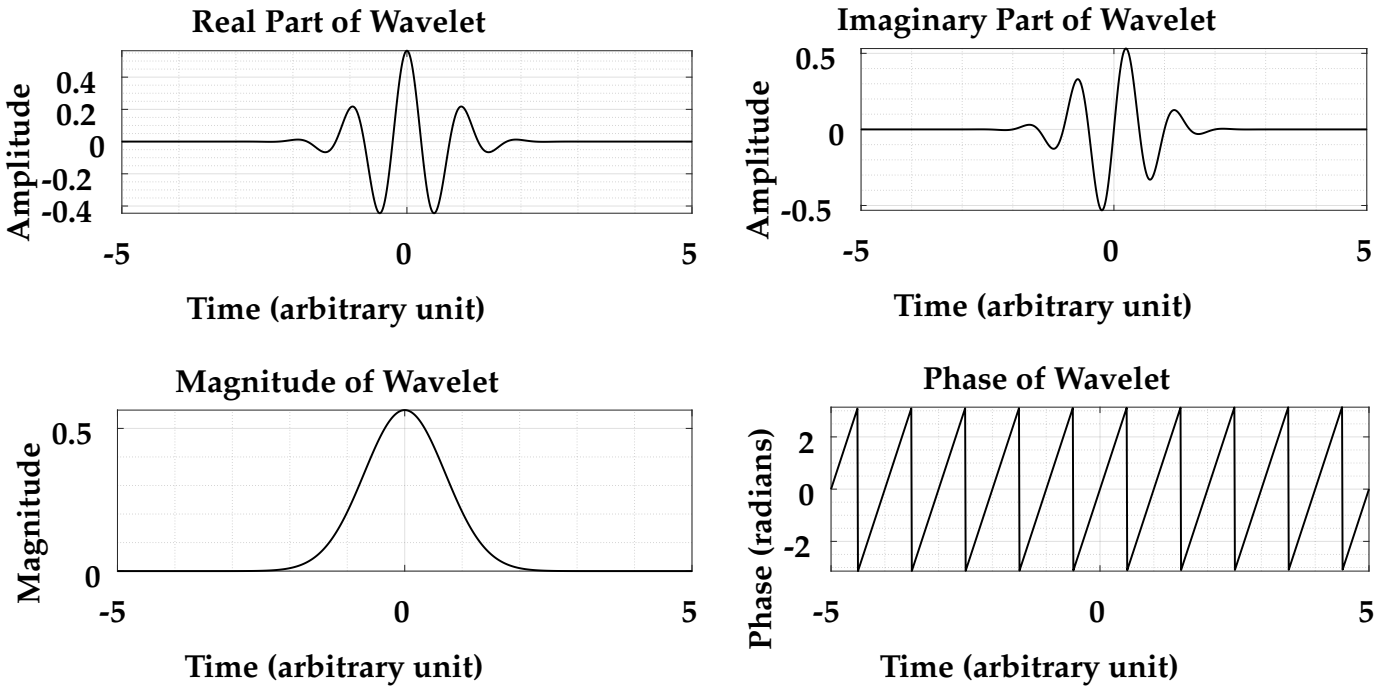

Figure III.10: Characteristics of the Morlet wavelet used as the mother wavelet in the continuous wavelet transform.

The advantage of time-frequency analysis using the Morlet wavelet is that its Gaussian shape

reduces the ripples that appear as oscillations, common in filters with sharp cut-off frequencies. Second, temporal resolution is retained when a Morlet wavelet is convolved with a signal. The Morlet wavelet convolution process on the other hand is computationally efficient and easy parameters adjustment compared to other wavelets. With its good time-frequency concentration and Gaussian envelope, the Morlet is preferred in continuous wavelet transform. It offers a good analysis of high-frequency as well as low-frequency oscillations making it a good tool in signal processing [11]. Figure III.11 presents the scalograms of the signals with their corresponding adhesion parameter.

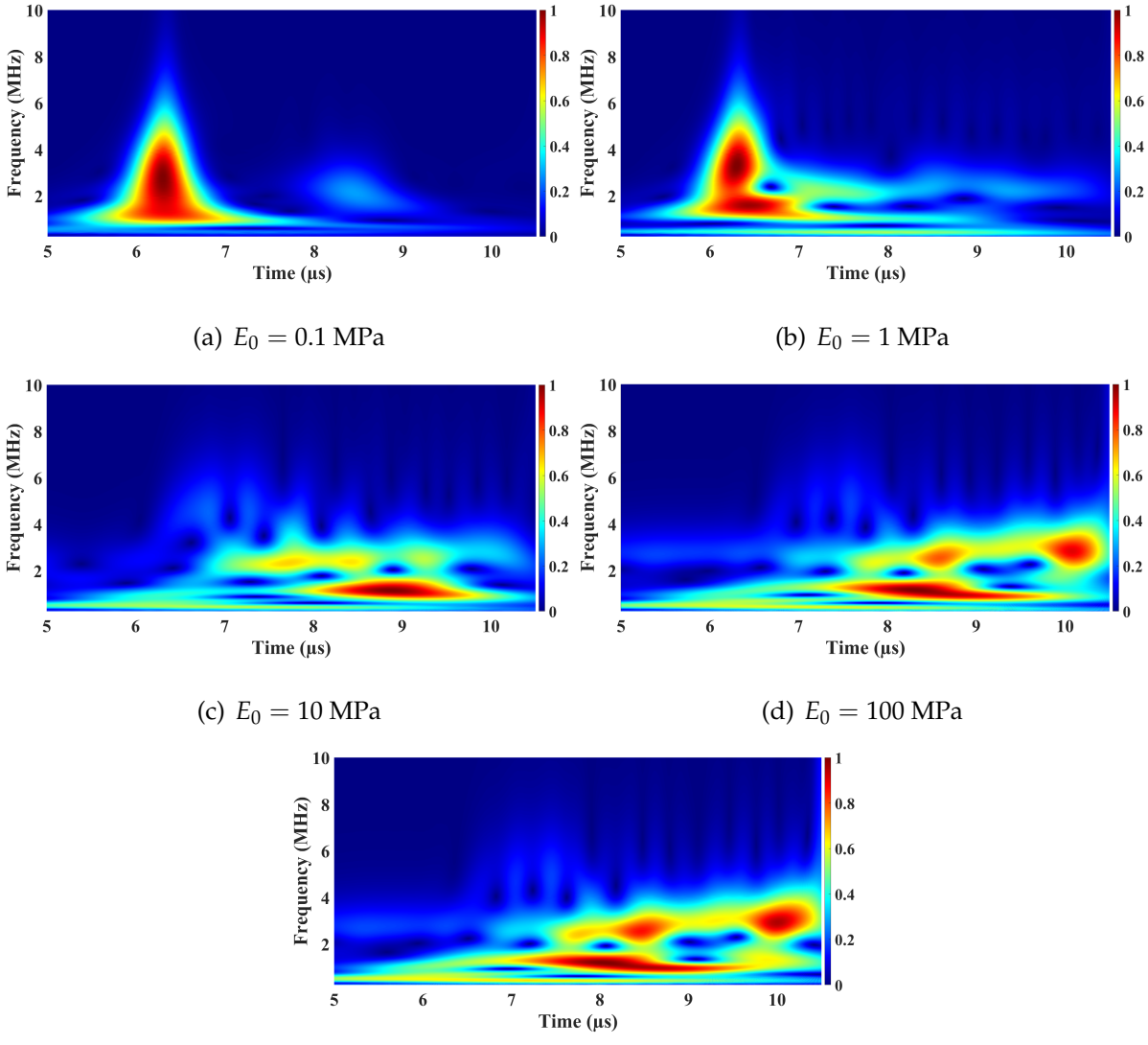

(a) $E_0 = 0.1$ MPa

(b) $E_0 = 1$ MPa

(c) $E_0 = 10$ MPa

(d) $E_0 = 100$ MPa

(e) $E_0 = 1000$ MPa

Figure III.11: The results of the square of the modulus after applying the wavelet transform.

These scalograms are the square of the modulus of the wavelet transform with a temporal resolution $T_s = \Delta t = 4$ ns. At $E_0 = 0.1$ MPa and $E_0 = 1$ MPa (a-b), the adhesion is weak and the surface acoustic wave does not interact with the elastic characteristics of the PVC film at the interface, therefore the scalogram shows no dispersion and the frequencies arrive at the same time. However, at $E_0 = 10$ MPa (c), the scalogram indicates that the surface acoustic wave interacts with the film at the interface and the adhesion is considered strong due to the obvious dispersion in the frequencies over time. By $E_0 = 100$ MPa and $E_0 = 1000$ MPa, the frequency distribution is almost the same. The interaction of the surface acoustic wave with the film reaches its maximum when $E_0 \geq 1$ GPa and the adhesion is in its perfect contact condition.

The sudden shift observed between the cases $E_0 = 1$ MPa and $E_0 = 10$ MPa indicates a high sensitivity of the surface acoustic waves to changes in adhesion quality.

2.3 Dispersion curves in studying uniform adhesion interface

As previously explained, by tracking the maximum amplitude for each frequency in the wavenumber-frequency domain, we can then plot the phase velocity dispersion curves. Figure III.12 presents the impact of adhesion strength on the SAW dispersion curves by progressively increasing E_0.

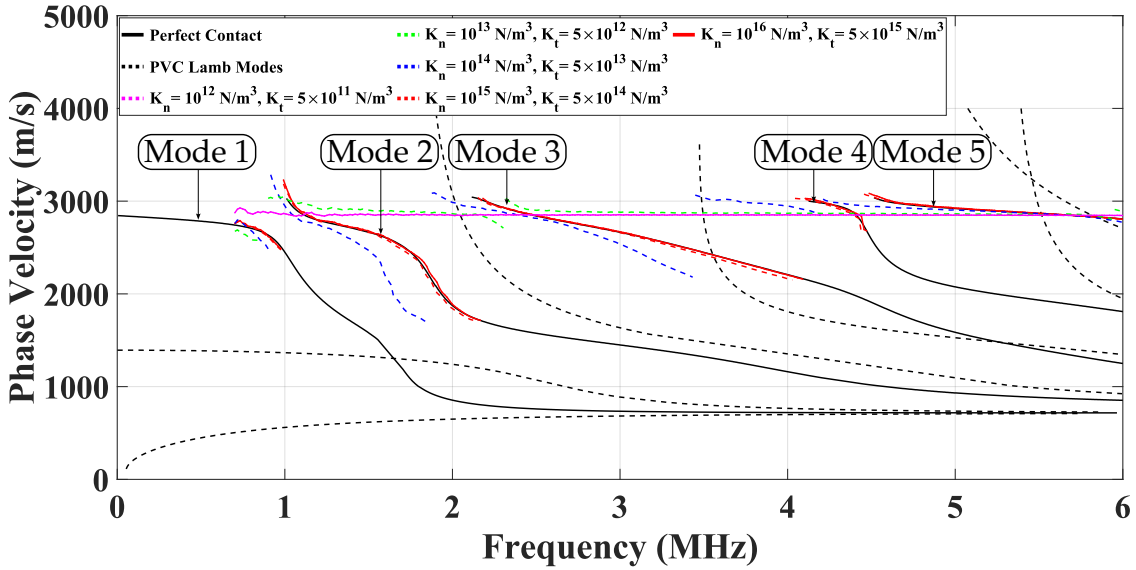

Figure III.12: Surface acoustic wave dispersion curves influenced by adhesion strength in the modeled cases.

The low resolution of the first mode makes it challenging to characterize the adhesion quality using this mode. However, in cases of weak adhesion, the curves approach the Rayleigh wave velocity of the substrate $c_R = 2844$ m/s. Consequently, multiple modes appear when the adhesion increases, with modes 2 and 3 being the most responsive to adhesion variations within the frequency range $0 \leq f \leq 6$ MHz. Modes 4 and 5 are closer to the c_R of the substrate, making it difficult to observe their modifications experimentally.

In the previous studies of the influence of the adhesion parameters K_n and K_t on the surface modes dispersion curves in Chapter II, we have seen that the curves converged towards the Lamb modes of the film and the Rayleigh wave velocity of the substrate when the adhesion decreases. However, this method shows that the film Lamb modes are not observed if the measurements are done at the interface in the case of weak adhesion or total detachment and the curves only converged toward the Rayleigh wave velocity of the substrate, this is due to the detection of the signals on the surface of the substrate. Hence, we observe the normal displacements that occur on the substrate. In the next section, a similar model is presented, to study the effect of the adhesion zone.

3 Studying the non-uniform adhesion quality

Adhesion was considered uniform across the acquisition distance in the previous simulation. In contrast, the following study aims to investigate the effect of the average adhesion strength, taking into account non-uniform adhesion at the interface. Figure III.13 illustrates the goal of the simulation.

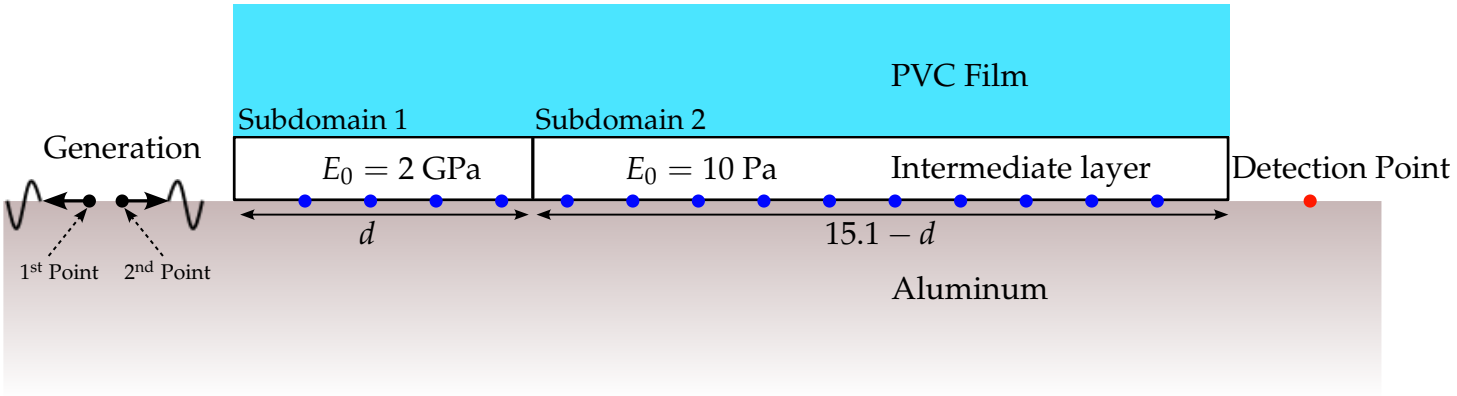

Figure III.13: Non-uniform adhesion illustrated in the intermediate layer of the model.

The intermediate layer is divided into two subdomains to model the non-uniform adhesion interface. In the first subdomain, adhesion strength is set at the perfect contact condition where Young's modulus is $E_0 = 2$ GPa ≥ 1 GPa according to the previous study. However, the second subdomain represents the weak adhesion condition with Young's modulus $E_0 = 10$ Pa. These values of adhesion strengths are constant and the length d of the first subdomain is progressively expanded in this study, leaving the rest (subdomain 2) of length $(15.1 - d)$ mm with weak adhesion strength.

3.1 Analysing the frequency distribution of the signals

Starting with an adhesion zone of $d = 1$ mm and incrementally enlarging it by 2 mm, we observe eight signals that analyze how the propagation behavior of the surface acoustic wave is influenced. Moreover, the propagation distance between the generation and the red virtual probe remains constant for this study.

Figure III.14 illustrates the effect of varying the adhesion distance d on the interaction of the Rayleigh modes with the PVC film at the interface. Similarly, a 4 MHz low-pass filter is applied to the signals approaching the experimental ones.

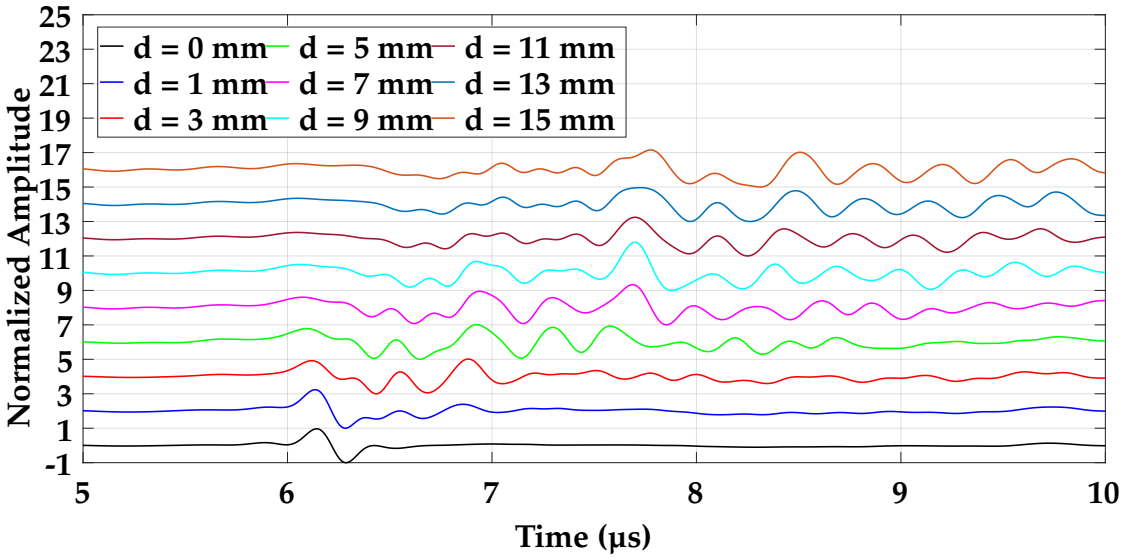

Figure III.14: Signals detected at the red virtual probe with increasing the adhesion distance d.

The resulting signals show that the propagation of the surface acoustic wave at the interface inter-

acts significantly with the PVC film at a larger adhesion distance. Therefore, we can conclude that the wave interacts with the film only in the range (d) that is defined as a perfect contact.

The eight signals are compared to the one with $d = 0$ mm (in black), at which the film is detached. The signal undergoes no dispersion at $d = 0$ mm. At $d = 1$ mm shows a slight change in the signal, while at $d = 3$ mm, the dispersion becomes more evident, eventually reaching a limit in their dispersion for $d \geq 11$ mm.

The detected normalized amplitude starts with signals that have relatively short wavelengths. As the adhesion distance d increases, the signals become progressively wider, indicating an increase in wavelength. This suggests that a larger adhesion area influences wave propagation at the interface, resulting in a shift towards a lower frequency range. Whereas, at smaller adhesion distances ($d = 0$ mm), the signal shows a shorter wavelength of higher frequency Rayleigh wave. This behavior illustrates the impact of adhesion distance on the propagation characteristics of the wave, where larger adhesion areas reduce the frequency and increase the wavelength of the detected signals. Figure III.15 presents the spectra of these signals for a better analysis.

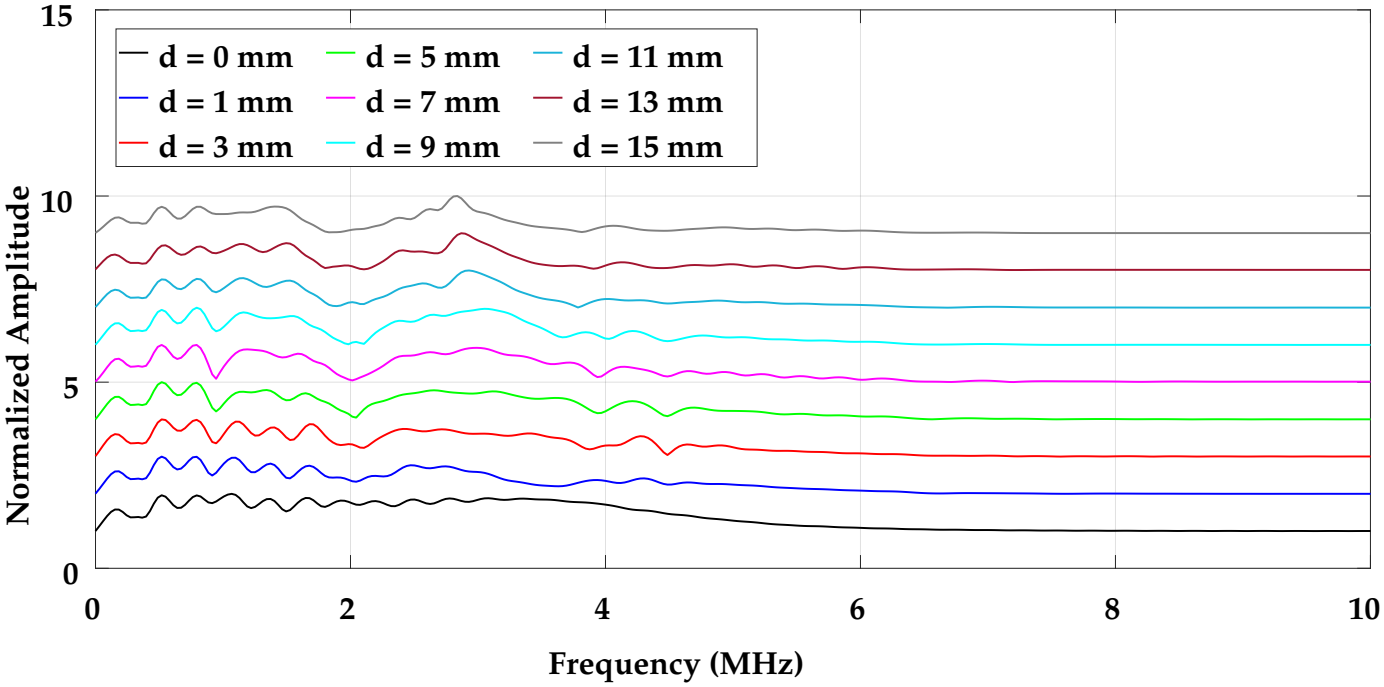

Figure III.15: Fourier transform of the detected signals at the red virtual probe with increasing the adhesion distance d.

The Fourier transform of the detected signals confirms the previous analysis. The black and blue curves represent the spectra at smaller adhesion distances ($d = 0$ mm and $d = 1$ mm, respectively). These spectra have overlapping peaks in the frequency range of $1 - 3.5$ MHz and show amplitude attenuation after 4 MHz due to the applied low-pass filter.

As the adhesion distance increases, the spectral peak amplitudes are separated and shifted towards lower frequencies $0.4 - 2.8$ MHz. This shift is observed as an attenuation in the amplitude of higher-frequency components and an increase in the amplitude of lower-frequency components. Therefore, the larger adhesion areas increase the wavelengths of the wave observed in the time-domain signals.

Similarly, the continuous wavelet transform offers a better analysis of the dispersion characteristics of surface acoustic waves concerning the adhesion zone, as depicted in the scalograms of figure III.16.

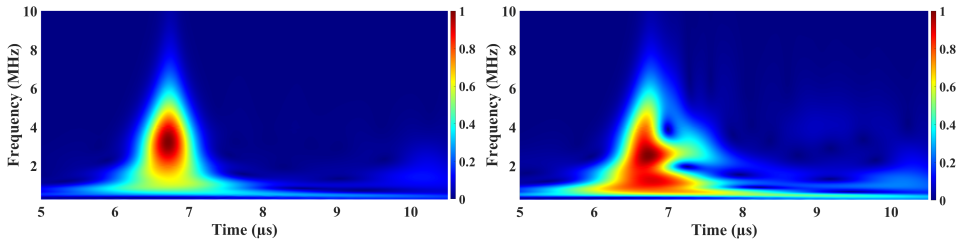

(a) $d = 0$ mm

(b) $d = 1$ mm

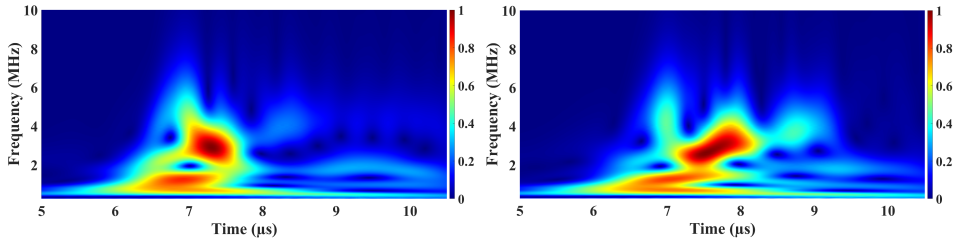

(c) $d = 3$ mm

(d) $d = 5$ mm

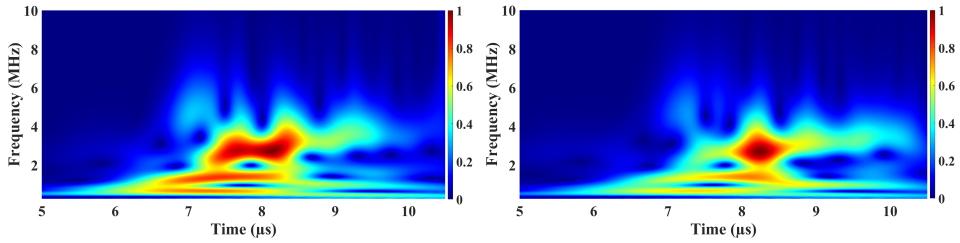

(e) $d = 7$ mm

(f) $d = 9$ mm

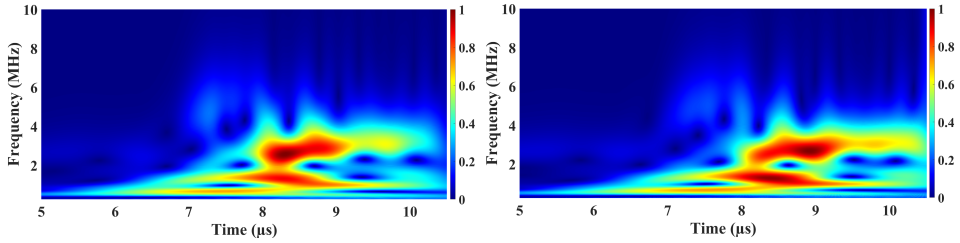

(g) $d = 11$ mm

(h) $d = 13$ mm

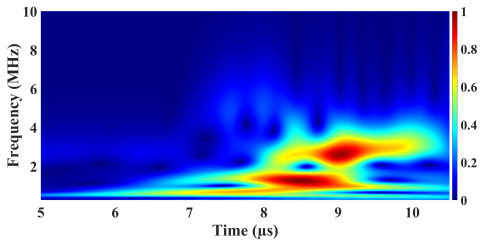

(i) $d = 15$ mm

Figure III.16: Studying the effect of the area adhered on the frequency distribution of the signals as a function of time using the same wavelet transform.

In (a) and (b), the dispersion is comparable to that when the adhesion is weak and the frequency values arrive at the same time with slight changes in (b). However, the shifting of the amplitudes starts in (c) indicating a dispersive signal. In (d) and (e), the signals start to show low-frequency components, indicating a further shift in the frequency spectrum as the adhesion area increases. The adhesion starts to improve progressively and becomes more related to strong adhesion due to the dispersion observed in (f) and (g). Moreover, (h) and (i) demonstrate that the low-frequency components are more stable and the energy is distributed in time with a larger adhesion area indicating multiple surface modes and an increase in the dispersion of the signals reaching the perfect contact limit.

This additional analysis highlights the continuous transition from high-frequency to low-frequency dominance in wave propagation as the adhesion area increases. The wavelet transform presented this shift in frequency content over time and provided a good approach to the adhesion area impact on the interaction of SAW with the interface.

3.2 Dispersion curves in studying non-uniform adhesion interface

Figure III.17 shows the influence of the variation of d to the dispersion curves.

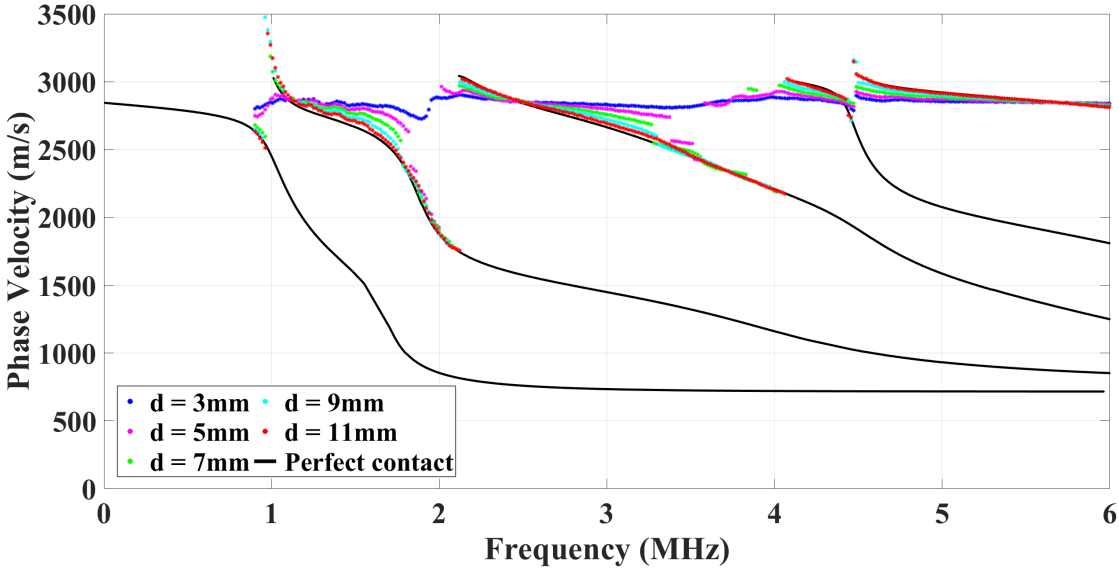

Figure III.17: Comparison of non-uniform adhesion dispersion curves with the ones relative to the perfect contact case.

The results indicate that with a weak average adhesion strength ($d = 3$ mm), the dispersion curves approach the Rayleigh wave velocity of the substrate ($c_R = 2844$ m/s). As d increases up to 11 mm, indicating stronger adhesion, the curves split into multiple modes and progressively converge towards those of perfect contact condition.

4 Electro-adhesion: a modeling approach

Using the default equations and studying the electrostatics. The electric potential, V, in the region of interest (absent of free charges), obeys Laplace's equation [12]:

$$\nabla^2 V = 0 \tag{3.12}$$

However, if there are free charges present, the electric potential is governed by Poisson's equation:

$$\nabla^2 V = -\frac{\rho}{\varepsilon} \tag{3.13}$$

Where ∇^2 is the Laplacian operator, ρ represents the free charge density and ε is the permittivity of the material, typically expressed as $\varepsilon_0 \varepsilon_r$, the product of vacuum permittivity ε_0 and the relative permittivity ε_r of the material. Subsequently, the electric field, E, can be determined from the negative gradient of this potential:

$$E = -\nabla V \tag{3.14}$$

This electric field can then be evaluated specifically at the surface of the dielectric element.

4.1 Electro-adhesion effect

As previously introduced in Chapter I, the electro-adhesion occurs due to induced attraction forces generated by the electrodes. The expected force responsible for this adhesion results in an induced pressure in the range of the electric field. This pressure can be theoretically quantified by the Maxwell

stress tensor considering a uniform electric field. A previous research focused on contact EA pads modeled as parallel plate capacitors. In this section, we refer to a model by Jiubing Mao et al. [13] aiming to validate the values of Maxwell's stress tensor.

4.1.1 Modeling the EA pad electrode effect

The model examines an EA pad composed of multiple electrodes alternately charged with positive and negative voltages of identical magnitude. Figure III.18 illustrates the EA pad, focusing on a segment of the system, taking a single electrode forming a parallel plate capacitor setup. This subsystem consists of an electrode plate charged with either a positive or negative voltage, placed on a dielectric insulator of relative permittivity ε_{r_1} and a thickness of d_1, followed by an air gap with a relative permittivity ε_{r_2} and a thickness of d_2 and finally, the second plate, which is a grounded conductor.

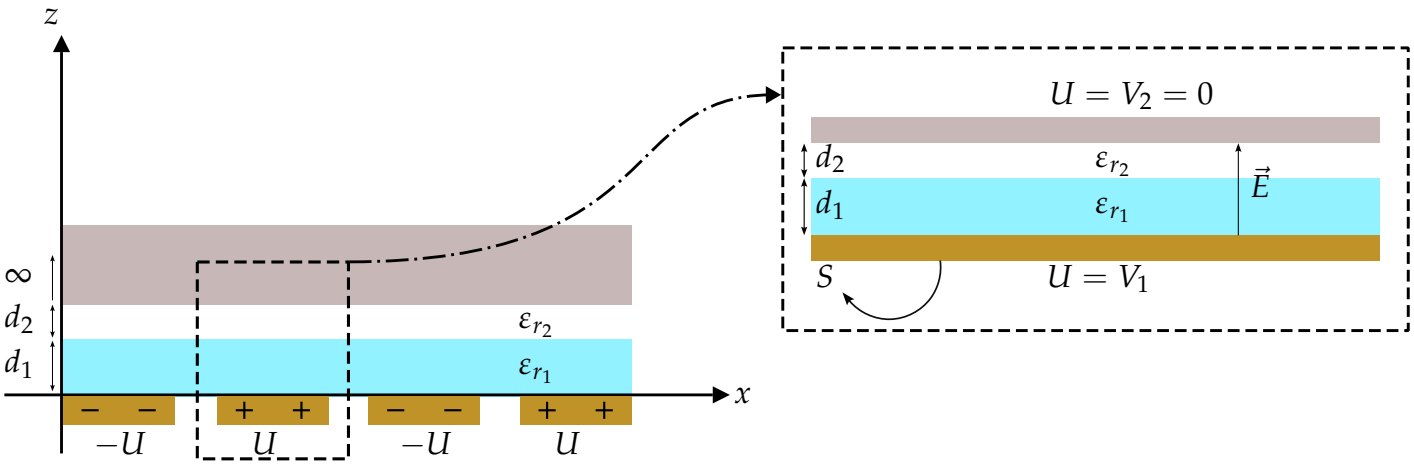

Figure III.18: Schematic of the Electro-Adhesion (EA) Pad with Parallel Plate Capacitor Design [13].

A three-dimensional electrostatic model is developed. The plates in this model are assumed to be a squared shape with a side length L calculated from [13]. These parameters are summarized in Table III.4.

	Side Length L (mm)	Thickness d_i (μm)	Relative Permittivity ε_{r_i}
Copper	10.95	–	–
Polyimide	10.95	$d_1 = 25$	$\varepsilon_{r_1} = 3.5$
Air	10.95	$d_2 = 5$	$\varepsilon_{r_2} = 1$

Table III.4: Model parameters for different materials.

The detailed dimensions and geometry of the model are depicted in Figure III.19. This figure illustrates the surface where the integration of the Maxwell stress tensor is calculated. The structure is positioned within an air medium with a side length of $2L$ and thickness of 1.5 mm. Positioning the structure within an air medium can be an initial model for further studying the non-contact EA effect. However, this does not affect the results.

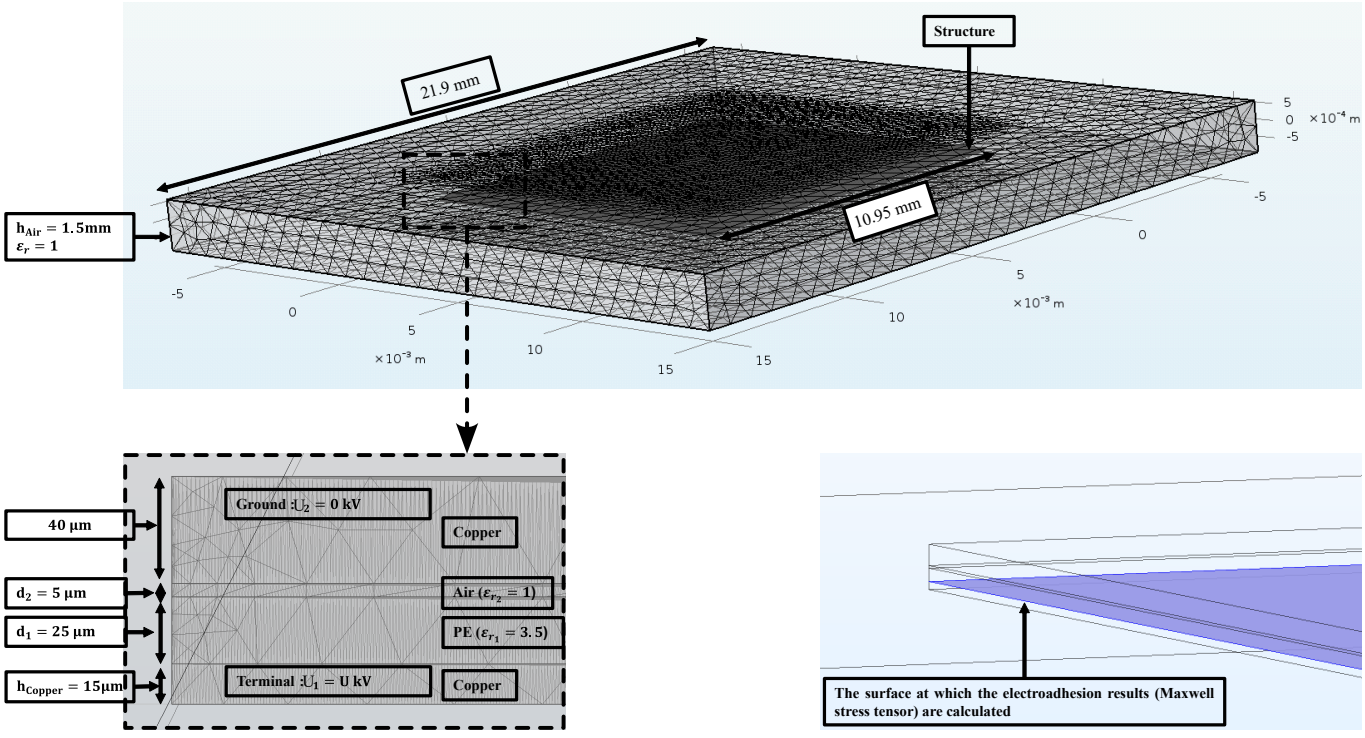

Figure III.19: Detailed dimensions of the model Geometry showing the surface for the calculated integral of Maxwell stress tensor.

The EA force can be calculated using default equation settings, which compute the electric force F_e

by determining the electric field E induced at each element based on the input boundary conditions. These latter correspond to the grounded conductor (i.e., the top plate $U = 0$ (kV)) and the terminal electrode loaded with voltage U (kV). The well-known Maxwell's stress tensor equation, in the absence of a magnetic field, is expressed as follows [14]:

$$T_{ij} = \varepsilon \left(E_i E_j - \frac{1}{2} \varepsilon E^2 \delta_{ij} \right) \tag{3.15}$$

Where ε and δ_{ij} represent the relative permittivity and the Kronecker delta, respectively. Due to the existence of simulated values of Maxwell's stress tensor in opposite directions normal to the surface in the z direction, which is caused by the effect of different materials, it becomes essential to calculate the jump in Maxwell's stress tensor. This jump is denoted by $\langle T_{zz} \rangle$ such that [15]:

$$\langle T_{zz} \rangle = T_{zz}^{+} - T_{zz}^{-} \tag{3.16}$$

T_{zz}^{+} and T_{zz}^{-} correspond to the values slightly above and below the surface in the z-direction, respectively. The electrostatic adhesion force is derived by integrating $\langle T_{zz} \rangle$ over the surface, as illustrated in Figure III.19 and can be expressed as follows [13]:

$$F_e = \frac{\varepsilon_{r_1} \cdot \varepsilon_{r_2}^2 \cdot \varepsilon_0 \cdot U^2}{2 \cdot (\varepsilon_{r_1} \cdot d_2 + \varepsilon_{r_2} \cdot d_1)^2} \cdot S \tag{3.17}$$

Results of Maxwell's stress tensor

This model shows that a uniform electric field norm corresponds to a uniform Maxwell stress tensor norm due to the parallel plate structure. Figure. III.20 presents the integration of the Maxwell stress tensor evaluated over the desired surface, thereby verifying the accuracy of the model [13].

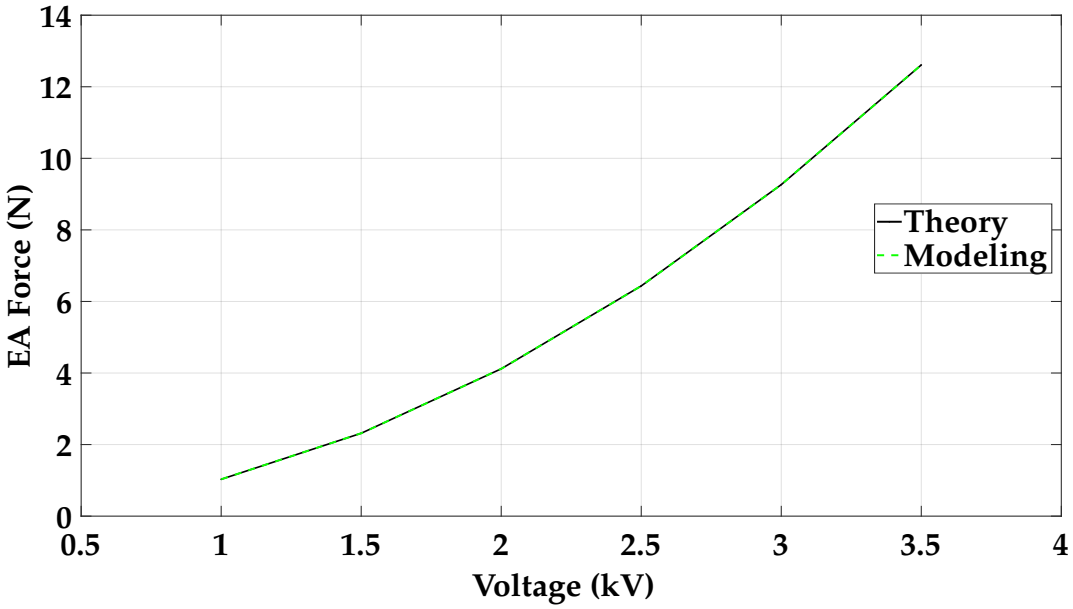

Figure III.20: Calculated F_e from the theoretical derivation equation 3.17 and the integration of Maxwell stress tensor by simulation

As the voltage increases from 1 kV to 3.5 kV, the Maxwell stress tensor also increases from 1.0 N to 12.6 N. Although this model is for parallel plate electrodes, this evaluation is important for EA simulations, as it should provide methods for modeling the threshold voltage value at which the layer adheres to the substrate.

The complexity of modeling the SAW interaction with adhesion conditions affected by an electric field source in a multiphysics model lies in many factors that need to be considered. This section outlines the main factors and limitations:

- Dielectric strength: is important in such models and can be influenced by the thickness and quality of the dielectric film considered.

- Adhesion of the layer to the substrate: Some layers adhere to certain substrates when an applied pressure is used. When using an EA device in such model, this threshold pressure at which the film adheres should be evaluated and confirmed experimentally to ensure it can be accurately included in the model.

- The air gap between the dielectric and the substrate: This is essential in such models. As this

must decrease over time while voltage is applied, the model should be time-dependent for both the electric and the acoustic simulation.

- Interface boundary condition: This is the most important factor. The results of the Maxwell stress tensor should be transformed into a boundary condition that defines the adhesion strength of the interface to simulate the SAW interaction accurately.

Conclusion

In this chapter, the results of the finite element model in studying the surface acoustic wave interaction with the interface of a thin layer and a substrate were displayed and discussed.

In the first part, the geometry of the model was explained, with the dimensions of each subdomain and justified as well as the conditions to generate the acoustic waves in the simulation.

Then two studies were examined. First, the uniform adhesion strength was studied with its sensitivity to the adhesion parameters. Then, the non-uniform adhesion strength was investigated by splitting the intermediate layer into a zone with a fixed high-value Young's modulus and the other zone with a low one.

The results show that higher adhesion quality or higher adhesion zone results in more dispersive signals. The dispersion curves of these signals shift towards the perfect contact condition in both studies. However, in the uniform case, the curves showed the Rayleigh modes at which that corresponds to a value of the stiffnesses. Whereas, in the non-uniform case, as we have inserted a fixed value of the stiffnesses (which is in this study the perfect contact case), the curves showed a convergence from the Rayleigh wave velocity of the substrate towards the perfect contact case.

Moreover, the evaluation of the electro-adhesion effect using the integration of Maxwell's stress tensor is necessary for characterizing the EA devices. It shows that the increase in the potential difference increases the electro-adhesion effect (experimentally up to a certain limit depending on the dielectric strength). The verification of the model can be a starting point for modeling more complex EA devices for further studies.

Bibliography of Chapter III

[1] Masoud Khazaei Poul and Aspasia Zerva. "Time-domain PML formulation for modeling viscoelastic waves with Rayleigh-type damping in an unbounded domain: Theory and application in ABAQUS". In: *Finite Elements in Analysis and Design* 152 (2018), pp. 1–16.

[2] Jikai Du, Bernhard R Tittmann, and Hyeong Sick Ju. "Evaluation of film adhesion to substrates by means of surface acoustic wave dispersion". In: *Thin Solid Films* 518.20 (2010), pp. 5786–5795.

[3] Michael Schoenberg. "Elastic wave behavior across linear slip interfaces". In: *The Journal of the Acoustical Society of America* 68.5 (1980), pp. 1516–1521.

[4] LRF Rose. "Point-source representation for laser-generated ultrasound". In: *The Journal of the Acoustical Society of America* 75.3 (1984), pp. 723–732.

[5] Yong Dai et al. "Finite element modeling of the interaction of laser-generated ultrasound with a surface-breaking notch in an elastic plate". In: *Optics & Laser Technology* 42.4 (2010), pp. 693–697.

[6] Christopher B Scruby and Leslie E Drain. *Laser ultrasonics techniques and applications*. CRC press, 1990.

[7] Jan D Achenbach. "Laser excitation of surface wave motion". In: *Journal of the Mechanics and Physics of Solids* 51.11-12 (2003), pp. 1885–1902.

[8] Josef Krautkrämer and Herbert Krautkrämer. *Ultrasonic testing of materials*. Springer Science & Business Media, 2013.

[9] Sabrina Fourez et al. "Non-contact thickness gauging of a thin film using surface waves and a void effect on their propagation". In: *Measurement Science and Technology* 23.8 (2012), p. 085608.

[10] Frédéric Jenot. "Génération et détection d'ondes élastiques par sources lasers: applications au contrôle non destructif". PhD thesis. Valenciennes, 2003.

[11] Michael X Cohen. "A better way to define and describe Morlet wavelets for time-frequency analysis". In: *NeuroImage* 199 (2019), pp. 81–86.

[12] Frédéric Viry et al. "Electrostatic and Aerodynamic Modelling of the Charged Droplet Trajectories thanks to a Lagrangian-Eulerian Model in COMSOL Multiphysics®". In: *19th International Multidisciplinary Modeling & Simulation Multiconference*. 2022.

[13] Jiubing Mao et al. "Modeling and simulation of electrostatic attraction force for climbing robots on the conductive wall material". In: *2014 IEEE International Conference on Mechatronics and Automation*. IEEE. 2014, pp. 987–992.

[14] LD Landau, EM Lifshitz, and LP Pitaevskii. "Electrodynamics of Continuous Media. Burlington". In: *MA, USA: Butterworth-Heinemann* 2 (2008), pp. 64–66.

[15] Gerd Brandstetter and Sanjay Govindjee. *Chucking Pressures for Idealized Coulomb-type Electrostatic Chucks*. Department of Civil and Environmental Engineering, University of California, 2011.

Chapter IV

Surface acoustic waves characterization of adhesion induced by an electric field source

Introduction

Many papers have investigated adhesion using different methods, including ultrasonics. The electro-adhesion effect has been studied recently as the researchers predicted the presence of electrostatic forces at the interface. However, it is challenging to evaluate their quantitative behavior due to the complexity of the electrical, chemical and mechanical forces at the interface [1, 2, 3].

As mentioned in Chapter I, the electro-adhesion between coatings and substrates can be controlled by modifying their potential difference. However, there are also limitations to be considered such as specific materials that interact with EA devices, not designed for complex shapes and difficulty in controlling the forces [4, 5, 1].

This technology has potential applications in many fields, including robotics, packaging and human-machine interaction. In comparison to traditional adhesion methods, EA has the advantage of being fast and capable of handling sensitive surfaces [6]. It also eliminates the need for adhesive intermediate layers of non-uniform thickness.

This chapter discusses the principles of electro-adhesion using an electrode-based EA device and

its associated constraints. Moreover, we explore the attractive forces generated between a PVC film and an aluminum substrate. This is followed by a description of the EA device used in experimental investigations, specifying the challenges in defining adhesion levels and the experimental setup for Laser-Ultrasonics.

Concerning the experimental studies, we conduct experiments for different dielectric materials to explore the impact of the electric field on adhesion strength. Then, we investigate the effect of an electro-adhesion device on the interface boundary between a PVC film and an aluminum substrate for generating multiple levels of adhesion and the influence of these levels on the dispersion curves of surface acoustic wave providing an estimation of the adhesion properties by solving the inverse problem. Finally, we integrate the comparison with the finite element model that simulates surface acoustic wave interaction with interface conditions according to the experimental results.

1 Initial testing of a uniform electric field

In this part, we will explain the effect of applying the potential difference between two electrodes and generating attractive forces. This test was necessary to indicate the dielectrics that respond well to EA.

An aluminum plate is fixed to a solid handle at the top, while a copper film (electrode) adheres to the underside of the PVC surface. In this experiment, a motor controlled by software moves the upper part (aluminum plate) downwards to make contact with the PVC film. Subsequently, the plate is moved upwards to examine the adhesion between the PVC film and the aluminum plate. This test setup is depicted in Figure IV.1.

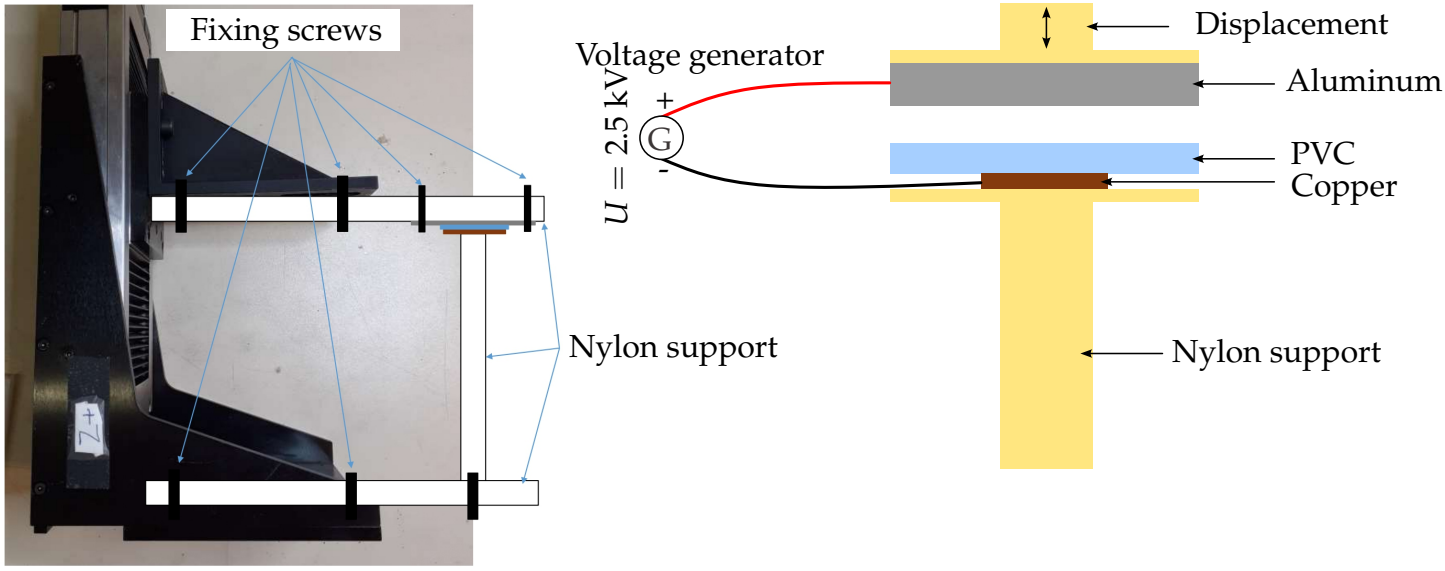

Figure IV.1: Experimental setup for testing the adhesive forces using a motor for translation.

1.1 Induced Maxwell stress tensor on PVC film

Studying adhesion affected by the electric field is directly linked to the electric properties of the materials. A Copper (Cu) film and aluminum plate were included as electrodes and a $U = 2.5$ kV potential difference was applied to demonstrate the effect of the electrostatic field on the adhesion of the film with polyvinyl chloride as the dielectric material.

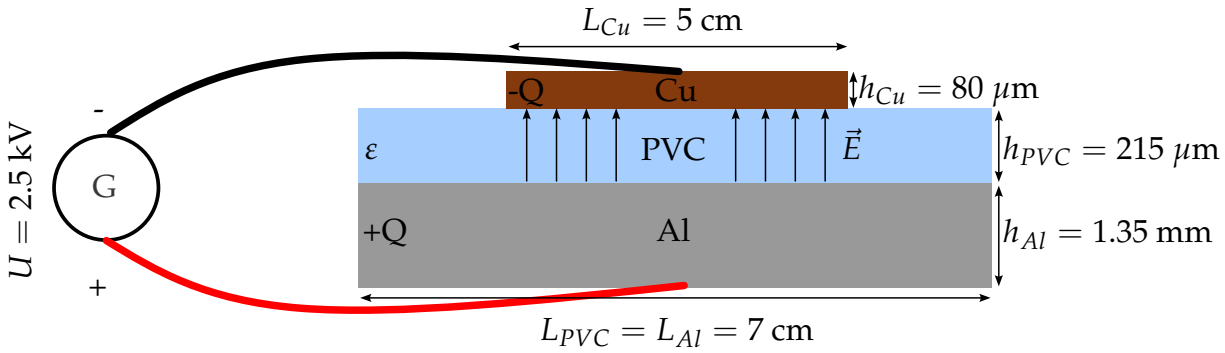

Figure IV.2: Diagram representation of the experimental setup.

Figure IV.2 shows the diagram of testing the effect of electrostatic forces on film adhesion. This system is comparable to a parallel plate capacitor as previously modeled. However, the copper plate

is smaller in area than the aluminum plate which has the same area as the polyvinyl chloride film. The measured parameters of each element are as follows:

Material	**Thickness (μm)**	**Area (cm^2)**	**Relative Permittivity (ε_r) [7]**
Aluminum	1350	49	–
Copper	80	25	–
Polyvinyl Chloride	215 ± 5	49	3.3

Table IV.1: Properties of different dielectric elements that are commonly used in scientific studies.

When 2.5 kV is applied across the plates, electrical charges are stored on the surface of each plate, establishing an electrostatic field between the plates. The dielectric material polarizes due to this field, leading to a local realignment of charge within the dielectric (as dielectric materials do not conduct electricity). This polarization can result in the generation of electrostatic forces at the interface between the dielectric and the plates. The accumulation and distribution of charges on the plates follow the laws of electrostatics, with positive charges accumulating on one plate and negative charges on the other.

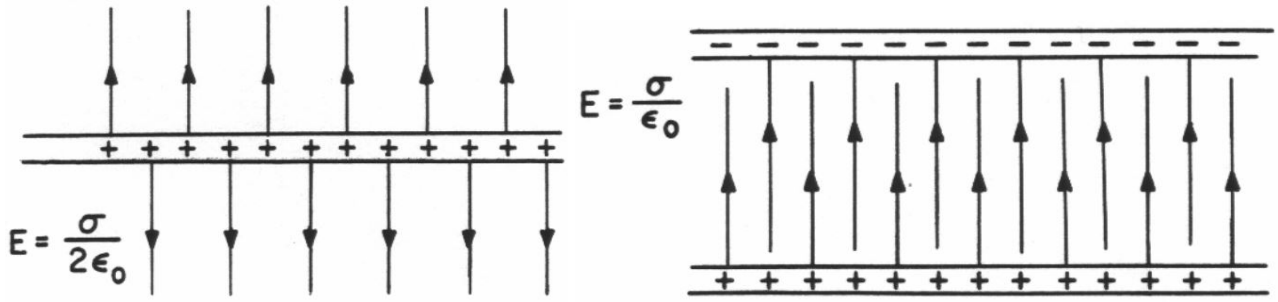

(a) (b)

Figure IV.3: Magnitude of electric field for a single infinite plate (a) and for a parallel plates capacitor (b) [6].

The electro-adhesion forces are simulated using the model in Chapter III for different voltages, the Maxwell stress tensor in the result of the integration over the area of the PVC film at the interface:

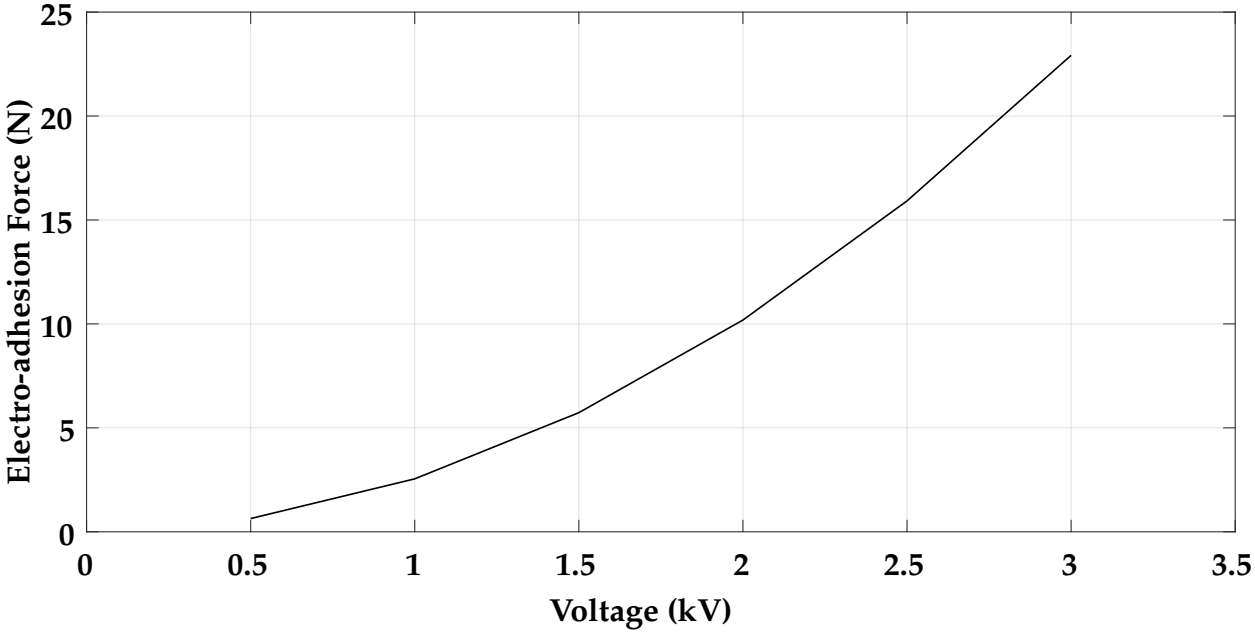

Figure IV.4: Electro-adhesion force variation as a function of voltage variation.

Figure IV.4, shows a similar increase of the electrostatic force to the voltage, to the increase of the modeled one in the previous section by the Maxwell stress tensor.

In this section, we present the effect of electrostatic forces on the adhesion of PVC to aluminum. While polyvinyl chloride naturally adheres to aluminum, electric forces are typically weak to significantly enhance this adhesion. High voltages are required to impact this effect. Accordingly, this test is designed to study the influence of an applied voltage U (with $0.5\ \text{kV} \leq U \leq 3\ \text{kV}$) on the adhesion of PVC to aluminum.

It is important to mention that if the upper plate continues to move downwards after making contact with the film, it will apply a certain pressure of undetermined magnitude, facilitating the adhesion of the PVC film to the aluminum substrate. Therefore, the upper plate is carefully stopped when the film makes a slight touch to the aluminum plate. While it is challenging to completely avoid exerting any pressure, it is possible to minimize it, ensuring that it remains below the critical threshold that would induce the film's adhesion.

The results in Figure IV.5 indicate that there is no adhesion between the aluminum surface and the PVC film. The copper film does not influence the adhesion effect while no voltage is applied.

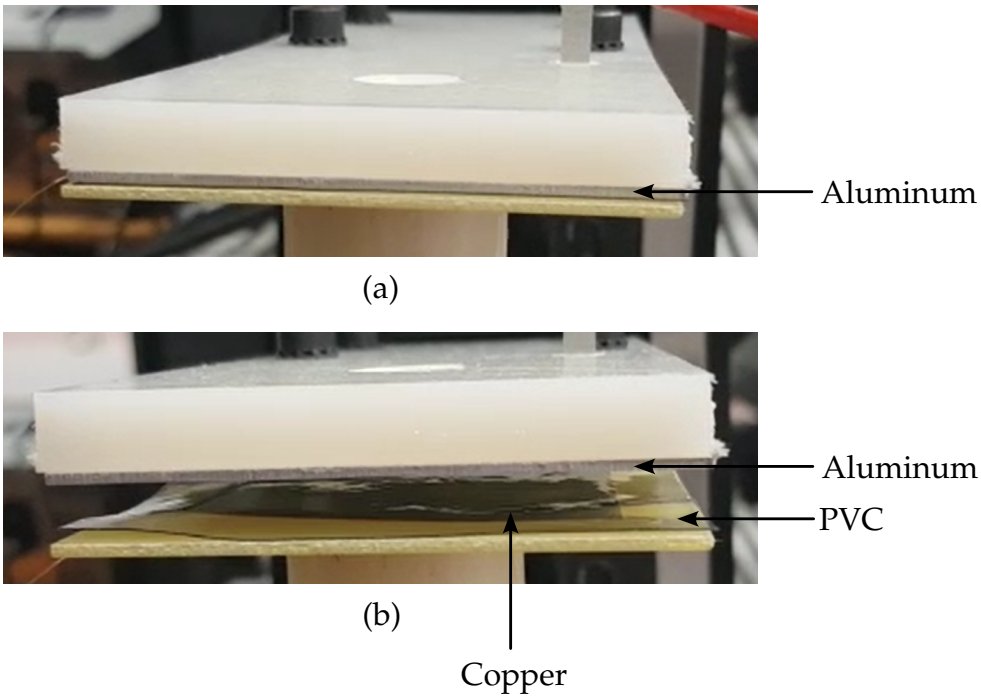

Figure IV.5: The aluminum plate while it is in contact with the PVC-Cu sample (a) and the result after the aluminum plate is released (b).

The results in Figure IV.6 demonstrate that the applied potential difference influences the adhesion between the PVC film and the aluminum plate. In (a), the aluminum plate is moved to the same position reaching a slight contact with the PVC film, in the same way mentioned previously and then a 2.5 kV voltage is applied. The sample is lifted upwards after turning the voltage off and the results in (b) confirm the adhesion of the PVC film to the aluminum plate.

This test is also done using polypropylene and polyethylene terephthalate as dielectrics, where they attach to the aluminum as long as the voltage is applied. However, once the voltage is switched off, the dielectrics detach after a short period (when the weight of the dielectric-Cu sample surpasses the electrostatic forces present in the capacitor during natural discharging), unlike the polyvinyl chloride film which takes a longer time to detach.

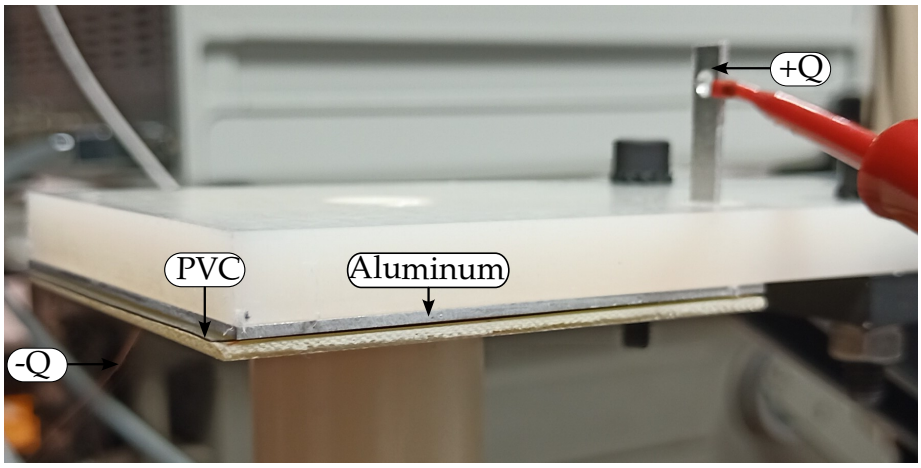

(a)

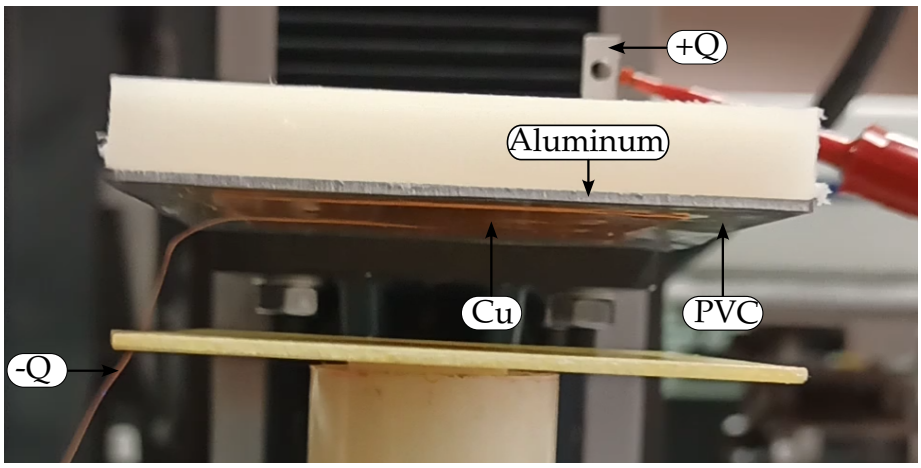

(b)

Figure IV.6: The aluminum plate in contact with PVC-Cu sample (a) and the result after applying voltage (b).

1.2 Induced attraction forces

The attraction forces between the PVC film and the aluminum plate are not distributed uniformly across the surface of the dielectric material due to the difference in the area of the conductors. In figure IV.7, an experiment is presented to investigate the possibility of the motor's pressure on the dielectric material being a contributing factor to the observed adhesion between the PVC film and the aluminum plate.

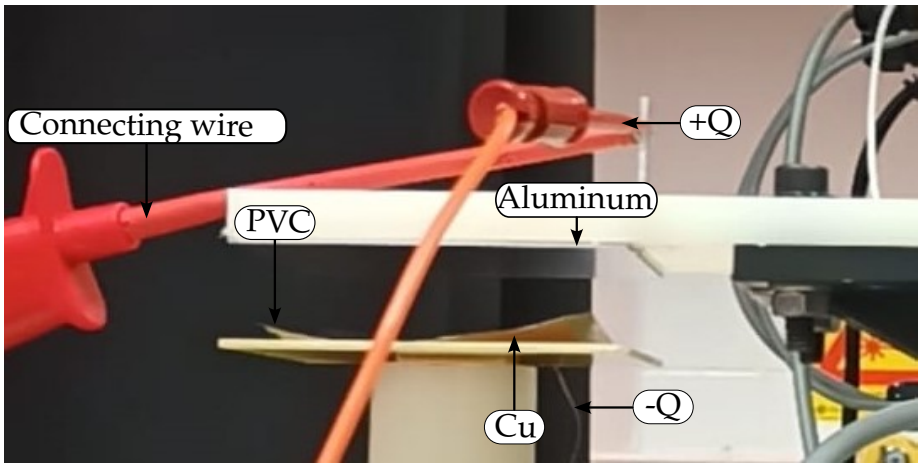

(a)

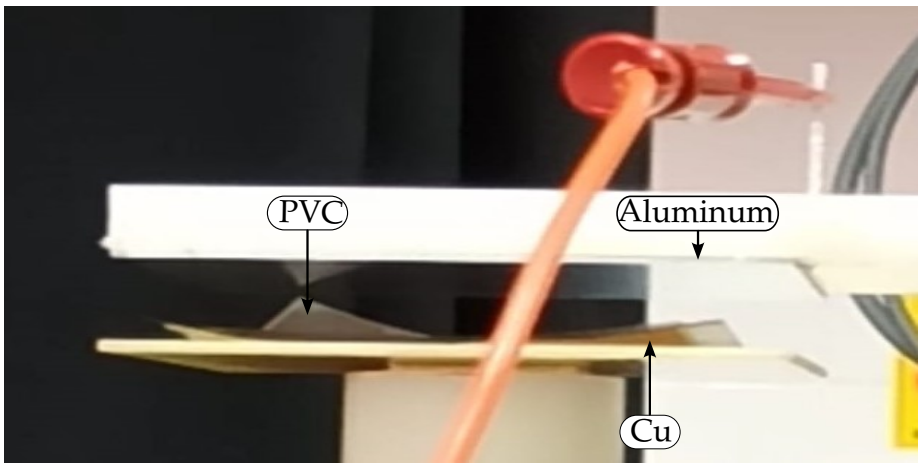

(b)

Figure IV.7: A connecting wire forms a short circuit (a) and after removing the short circuit (b).

In (a), a connecting wire (short circuit) across the system cuts off the current through the plates and then the aluminum plate is moved plate to approach the PVC-Cu sample. The results of this experiment show no effect of attraction.

In (b), the connecting wire (short circuit) is removed and the aluminum plate is moved closer to the PVC-Cu sample. The results show a slight force that attracts the PVC film towards the aluminum plate.

Although the motor's pressure on the dielectric material may be a factor in the observed adhesion between the PVC film and the aluminum plate. However, the adhesion is primarily influenced by the pressure induced by electric forces between the plates, taking into account the previous experiments.

2 Experimental mechanism and configurations

2.1 Laser-Ultrasonics setup

Figure IV.8 illustrates the setup used to generate acoustic waves, employing a frequency-doubled Nd:YAG laser with a 10 ns Q-switch that produces 532 nm wavelength pulses of a frequency at $f = 10$ Hz. By using a cylindrical lens, these laser pulses are shaped into a linear source of approximately 6 mm in length and 0.2 mm in width. The energy of each pulse is kept below 5 mJ to remain within the thermoelastic regime, which is conducive to optimal acoustic energy production perpendicular to the line source and generated from this line midpoint for surface acoustic waves.

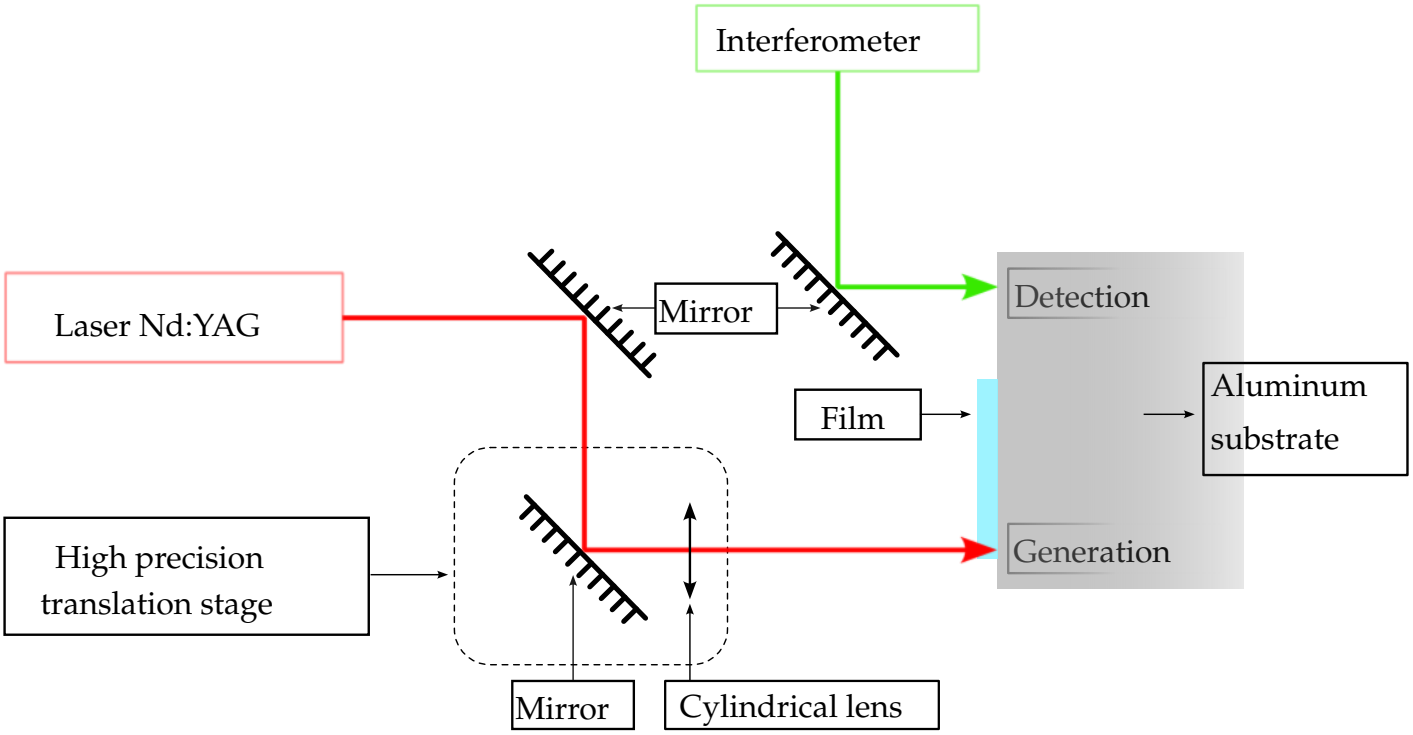

Figure IV.8: Laser-Ultasonics experimental setup.

The detection of the normal displacements of surface acoustic waves is performed using a Mach-Zehnder interferometer, which operates within the frequency spectrum of 200 kHz to 45 MHz. To optimize the signal-to-noise ratio, a low-pass filter with a 4 MHz cutoff is employed and the signal processing includes the averaging of 16 consecutive signals, i.e 16 laser-pulses. Surface acoustic waves propagate through the interface between the PVC film and the Al substrate and are detected

on the aluminum substrate's surface.

2.2 Methodology of the experiments

The generated surface acoustic wave propagates between the PVC film and the aluminum substrate and is affected by their elastic characteristics at a certain adhesion level creating dispersion in the signal. Figure IV.9 illustrates the two different configurations of the experimental methods, each has a specific purpose.

To obtain information about the film's adhesion, the generated linear source is located on the substrate's surface as a first configuration, enabling the surface acoustic wave to propagate across the entire width of the film. The film's transparency also allows the generation at the interface as the second configuration, facilitating the extraction of the dispersion curves from signals generated at the interface. The detection point of the interferometer is fixed at the substrate's surface in both cases.

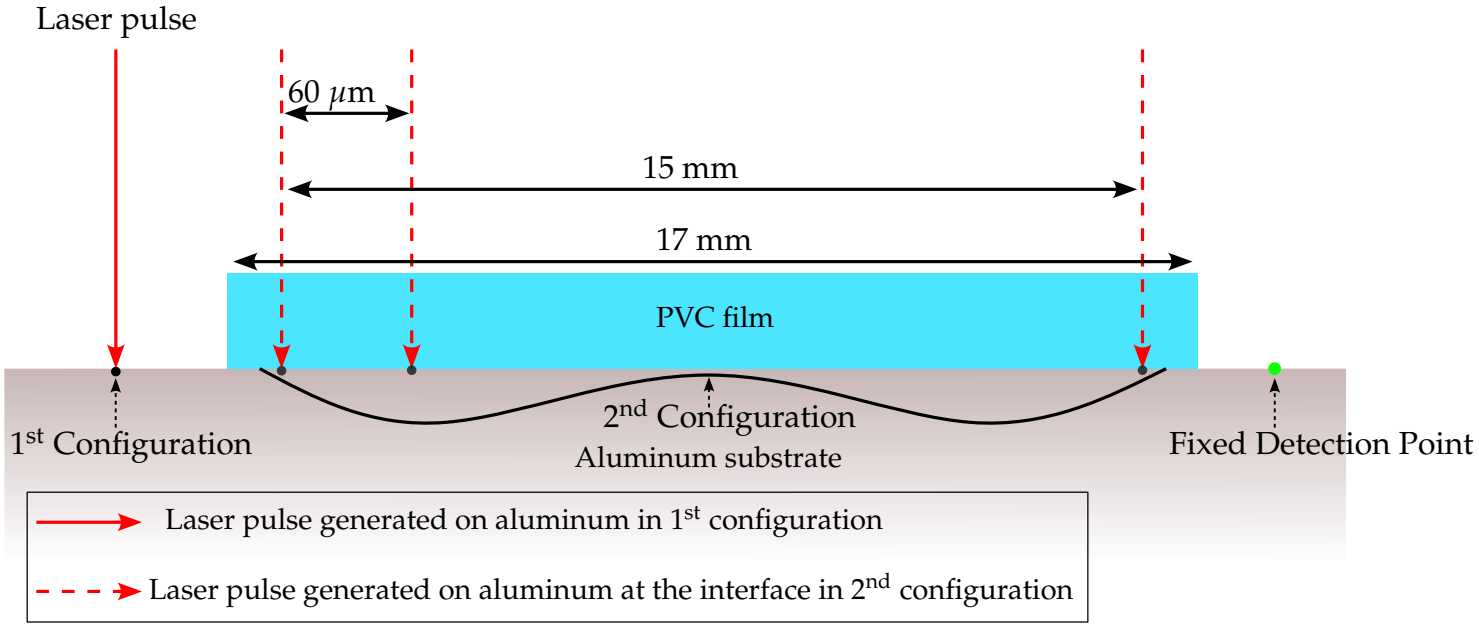

Figure IV.9: Experimental configurations.

3 Influence of the point source EA device on film adhesion

The previous test was composed of a copper conductor that was glued at the surface of the dielectric. It is known that the surface acoustic waves are sensitive to the adhesion condition as well as the thickness of the film, hence, it is quite complicated to use this EA device system to study adhesion using ultrasonics. Therefore, a non-contact EA pad system is included in the experiment and different dielectric materials are tested to check their adhesion response to this EA pad by generating and detecting surface acoustic waves.

3.1 Introducing the electric field point source

The sample consists of a PVC layer with a width of 17 mm, a height of 4 cm and a thickness of 215 ± 5 μm. This layer is placed on top of an aluminum square block, which has dimensions of 9.8 cm in width and length and height of 4.4 cm. Figure IV.10 (a) depicts the EA pad used, with thirteen sharp tips pointed electrodes connected to a Direct Current (DC) voltage generator. The experiment focuses on the interaction of a single electrode tip with the sample to characterize the EA pad's adhesive effect, the other tip sources of the pad are covered with an insulating layer, as illustrated in (b).

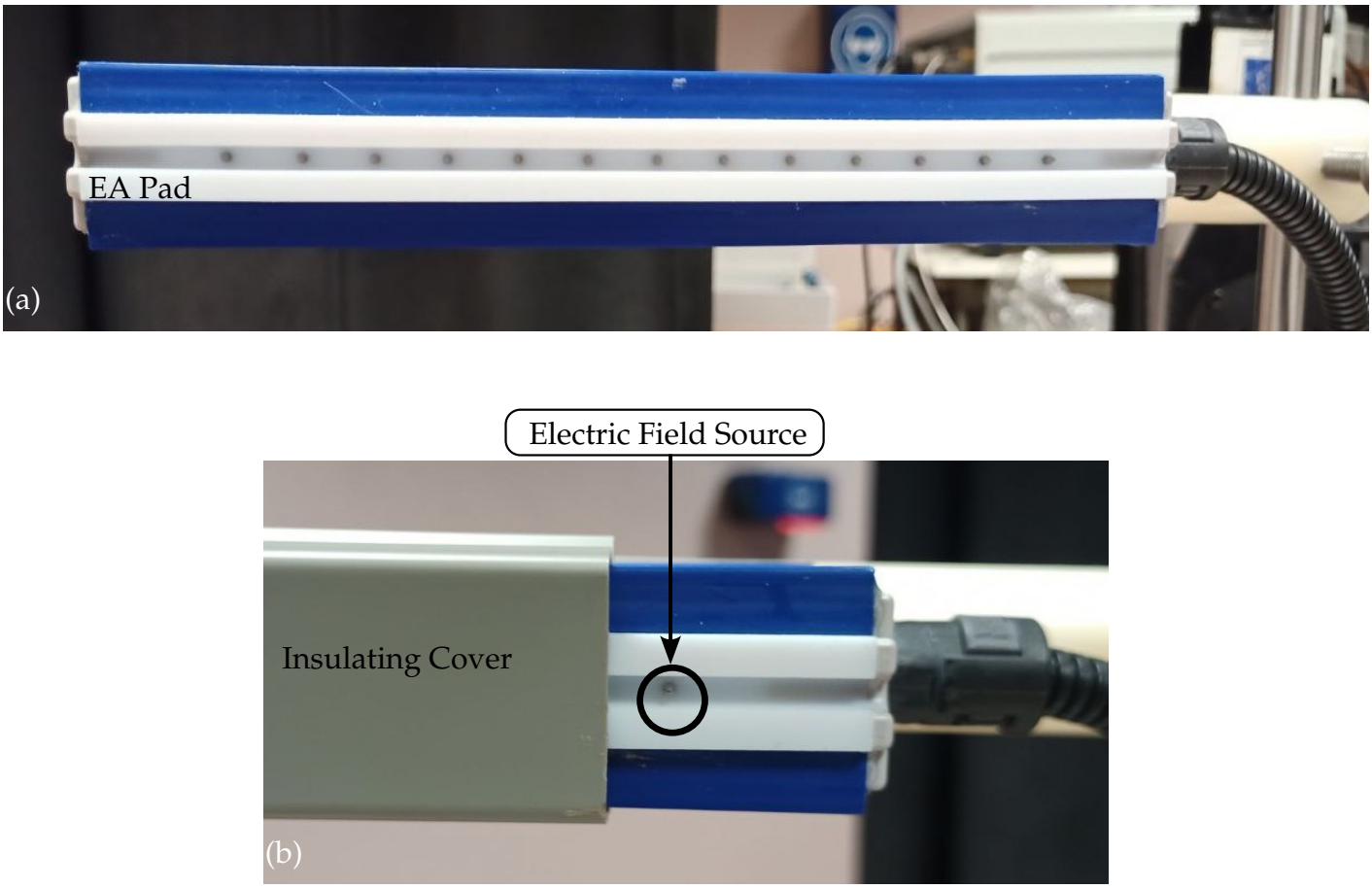

Figure IV.10: (a) 13 tip sources of the EA pad. (b) A single tip source is exposed to the sample.

3.2 Effect of the EA pad on different films

In this section, we aim to indicate the materials that can be affected by the source of the electric field by generating and detecting surface acoustic waves. This is achieved using the setup of the first configuration, where the wave travels through the entire interface.

The sharp tip faces the middle of the sample, positioned 2 cm away from the aluminum surface. The three dielectrics of polypropylene, polyethylene terephthalate and polyvinyl chloride of thicknesses 50 μm, 100 μm and 215 μm respectively, are placed facing the electric field source. It is necessary to select an initial voltage value at which the dielectrics can be weakly attracted to the substrate. Therefore, a voltage of 3.4 kV is selected at which the dielectrics are slightly affected and attached to the aluminum block. At this voltage level, the dielectrics are easily repositioned or slid.

This setup is illustrated in figure IV.11.

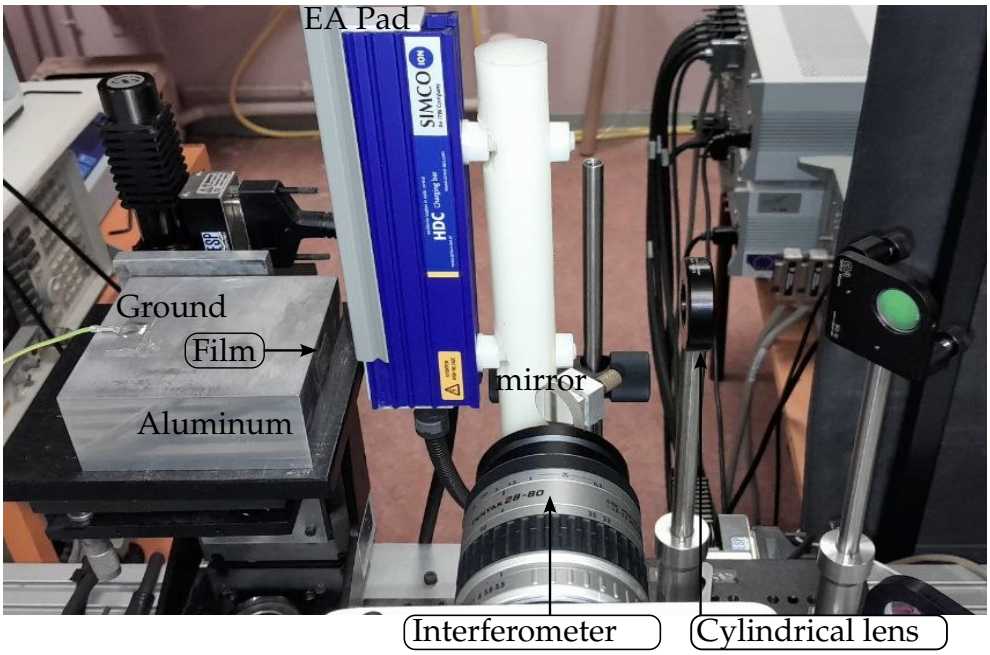

Figure IV.11: Setup of the experiment for testing the effect of electro-adhesion on SAW wave propagation for different dielectrics.

The results in figure IV.11, demonstrate the impact of EA source at a voltage of $U = 20$ kV on different films. Among these, the polyvinyl chloride shows a notable response. The dielectrics used in the experiment have the same dimensions of 17 mm width and 4 cm length.

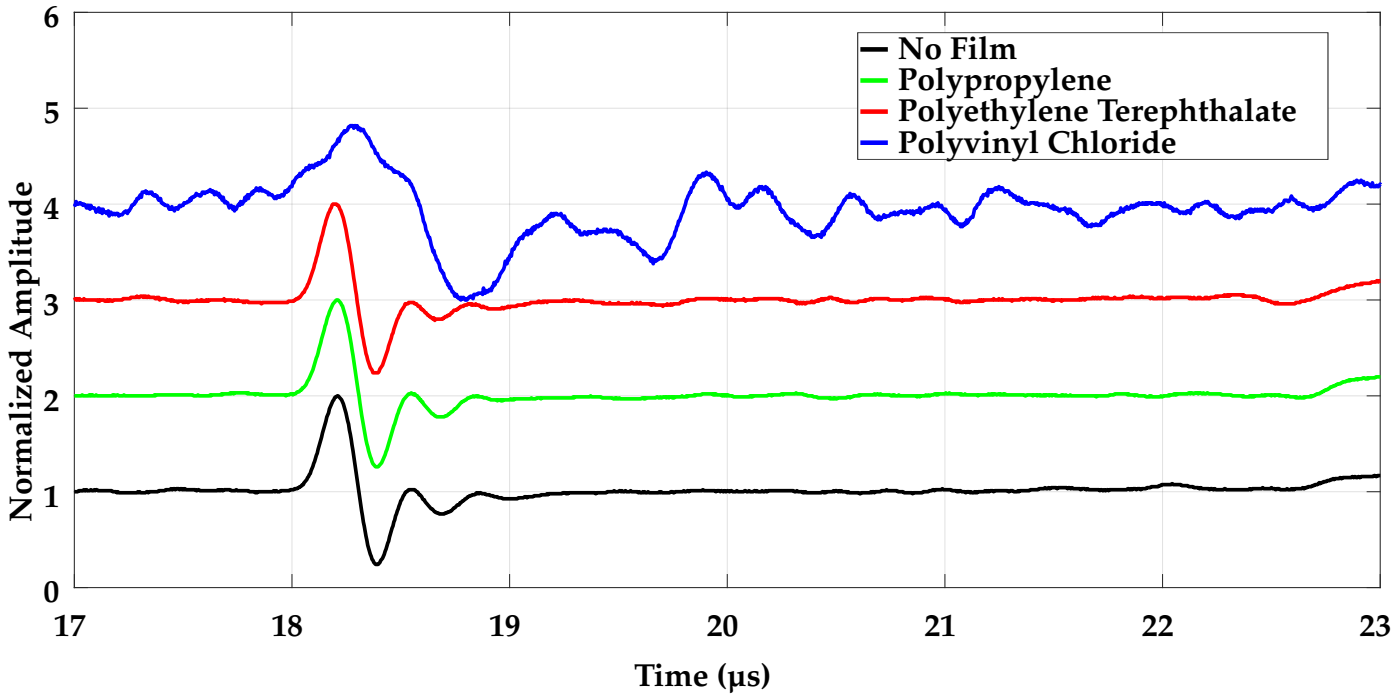

Figure IV.12: Effect of electro-adhesion on different dielectrics.

3.3 Electro-Adhesion pattern of PVC film on Al substrate from a point source

The PVC film is positioned on the aluminum substrate without an intermediate adhesive layer. The smoothed aluminum surface facilitates the attachment of the PVC when pressure is applied, predicting Van der Waals forces as the adhesive forces [8], which become stronger as the surfaces approach each other [9, 10]. The electric field source is generated by the tip source as a non-contact EA pad to enhance this pressure, thereby improving the adhesion via electric forces between the PVC film and the conductive substrate.

Figure IV.13 shows the electro-adhesion source tip positioned two centimeters from the central area of the PVC film. This source is maintained at a constant voltage for a certain adhesion level, while the conductive aluminum substrate is connected to the ground, resulting in a potential difference.

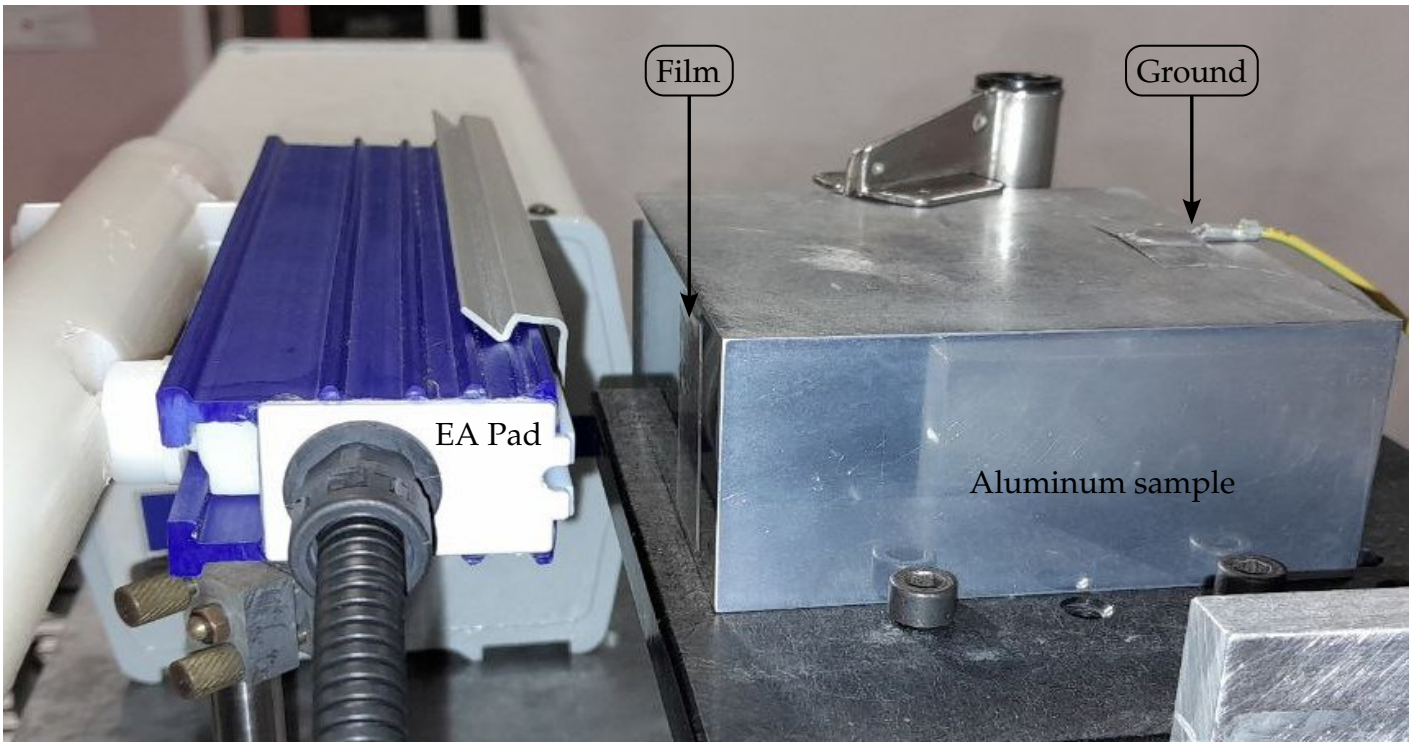

Figure IV.13: One tip source fixed at 2 cm from the aluminum substrate.

The DC generator is capable of producing voltages ranging from $0 \leq U \leq 30$ kV, inducing a charge Q to the tip electrode. The resultant potential difference creates dipoles at the sample interface, leading to electric pressure due to the electric field induced by the charge Q.

The EA system is positioned in a horizontal plane that is above the horizontal plane used for the Laser. Besides, the sample is placed on a computer-controlled motorized table. This setup allows the sample to be moved upward facing the EA pad to apply the voltage and then repositioned to its initial location for the generation and detection of acoustic waves.

The film must be carefully positioned on the aluminum surface without applying external pressure. It should then be exposed to a low voltage that allows the film to contact the substrate for a sufficient duration. The effect on the SAW should be evaluated before gradually increasing the voltage to higher values.

Following the initial observation of the EA effect at 3.6 kV acoustic waves are generated every 5 minutes after the voltage application. The dispersion of these waves becomes consistent after 90 minutes. Therefore, the voltage values are applied for 90 minutes to reach a stable adhesion effect.

These EA effects can be observed under a specific image acquisition device and the results for each adhesion level are displayed in figure IV.14.

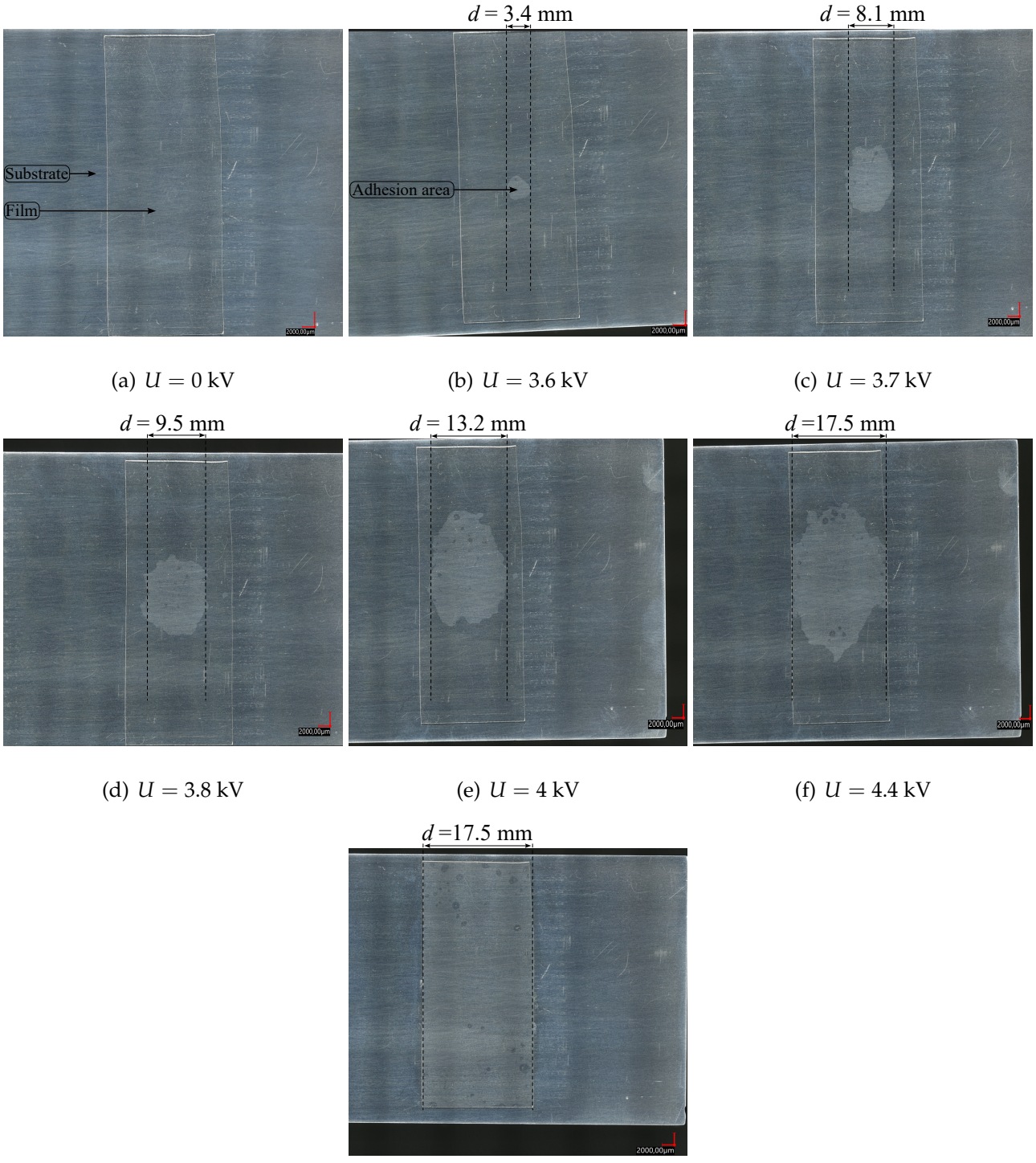

(a) $U = 0$ kV (b) $U = 3.6$ kV (c) $U = 3.7$ kV

(d) $U = 3.8$ kV (e) $U = 4$ kV (f) $U = 4.4$ kV

(g) $U = 6.3$ kV

Figure IV.14: Effect of the electric field source level on the adhesion of PVC film to the Al substrate.

Initially, the film is placed on the substrate for 2 hours to examine its natural adhesion properties without any external pressure. The result of this experiment is illustrated in figure IV.14 (a). Then the voltage U is increased incrementally by 0.1 kV starting from 3.6 kV. The EA effect progressively increased at 3.8 kV. At voltages of 3.9 kV and 4.0 kV, the film displays wider adhesion areas. Full adhesion along the horizontal plane is achieved at 4.4 kV and when the voltage reaches 6.3 kV, the entire surface of the film adheres to the substrate.

4 Characterization of the adhesion patterns via surface acoustic waves

In this section, we analyze the impact of electro-adhesion on the propagation of surface acoustic waves for each adhesion level. Initially, the laser pulse is directed onto the substrate's surface using the first experimental configuration. Subsequently, the second experimental method is used to obtain the dispersion curves, which illustrate their evolution with changes in the adhesion level. Next, the inverse problem is solved to estimate the adhesion strength assuming uniform adhesion of a specific pattern. Finally, the estimated adhesion parameters are integrated into a finite element model to simulate the interaction of surface acoustic waves to the adhesion pattern observed experimentally.

4.1 Analysis of the surface acoustic wave signals at different adhesion levels

Table IV.2 summarizes the previously obtained results at different voltages which led to the identification of seven distinct adhesion levels.

Adhesion Level	Level 1	Level 2	Level 3	Level 4	Level 5	Level 6	Level 7
Voltage U (kV)	0	3.6	3.7	3.8	4	4.4	6.3

Table IV.2: Adhesion levels corresponding to their voltages.

The length between the excitation point and the detection point is approximately 5.1 cm. Hence,

a post-trigger of 17 μs is selected and the arrival time of the signal is recorded at 18.2 μs, with a precision of $\pm$ 0.002 μs. A time frame of 6 μs is chosen to capture the entire signal at higher adhesion levels.

The detected signals are illustrated in figure IV.15, demonstrating that a larger adhesion area correlates with increased signal dispersion. This effect is previously predicted by finite element modeling, as a wider adhesion zone at the interface leads to increase the dispersion of the signal.

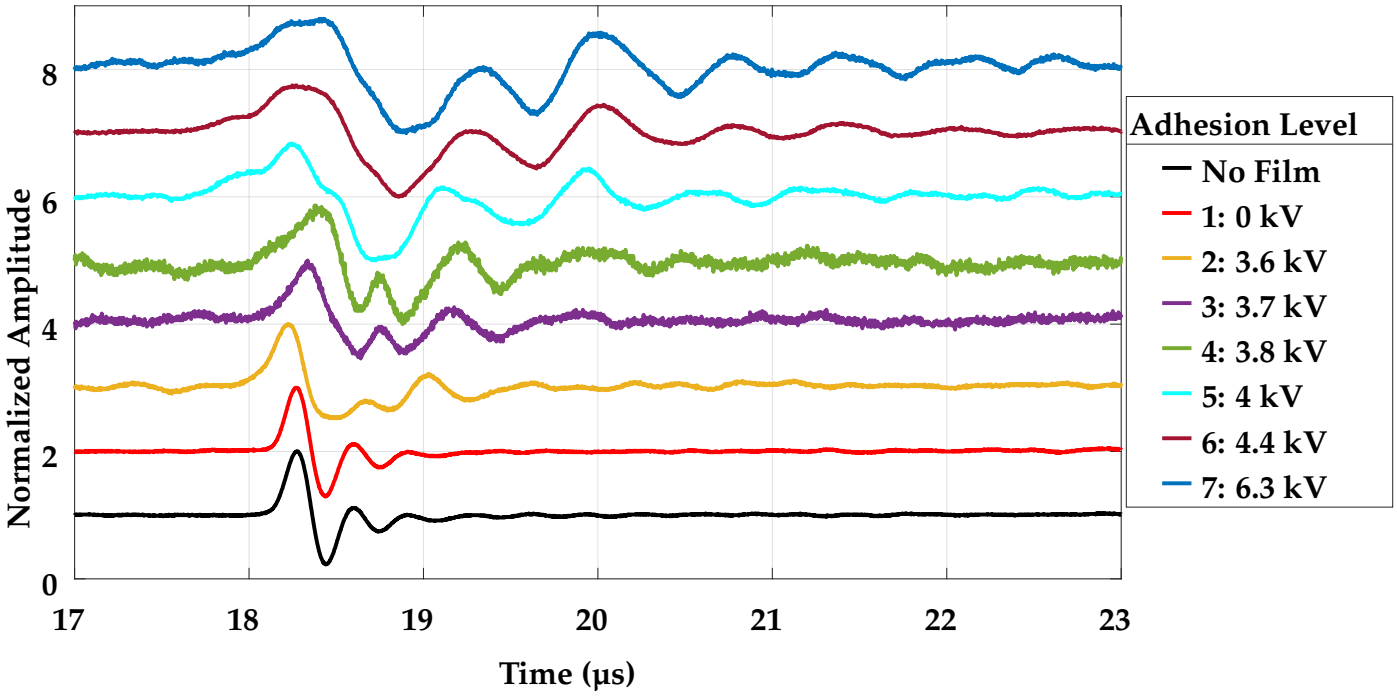

Figure IV.15: Influence of adhesion levels on the signal illustrating surface acoustic wave propagation.

At the initial adhesion level, the surface displacement signal shows no dispersion and is comparable to the signal when the film is absent, indicating complete detachment and no interaction with the film. At the second level of adhesion, the signal begins to show slight dispersion, due to the minimal area of adhesion. At adhesion level three, the dispersion in the signal increases and it further continues at level four due to a larger area being affected by the electric field. The film is nearly fully adhered by adhesion level five, resulting in significantly higher dispersion, comparable to that observed at level six, where the film is completely adhered. The dispersion remains consistent at adhesion level seven, suggesting that the maximum adhesion strength is reached at level six. Thus,

as the voltage increases, the adhesion surface progressively expands until the film is fully adhered.

The signals are analyzed in the time-frequency domain using the continuous wavelet transform, using the same mother wavelet in Chapter III. To better track the progression of surface acoustic wave dispersion in the frequency-time domain of the signal, with the temporal resolution selected by a sampling period of $T_s = 2$ ns.

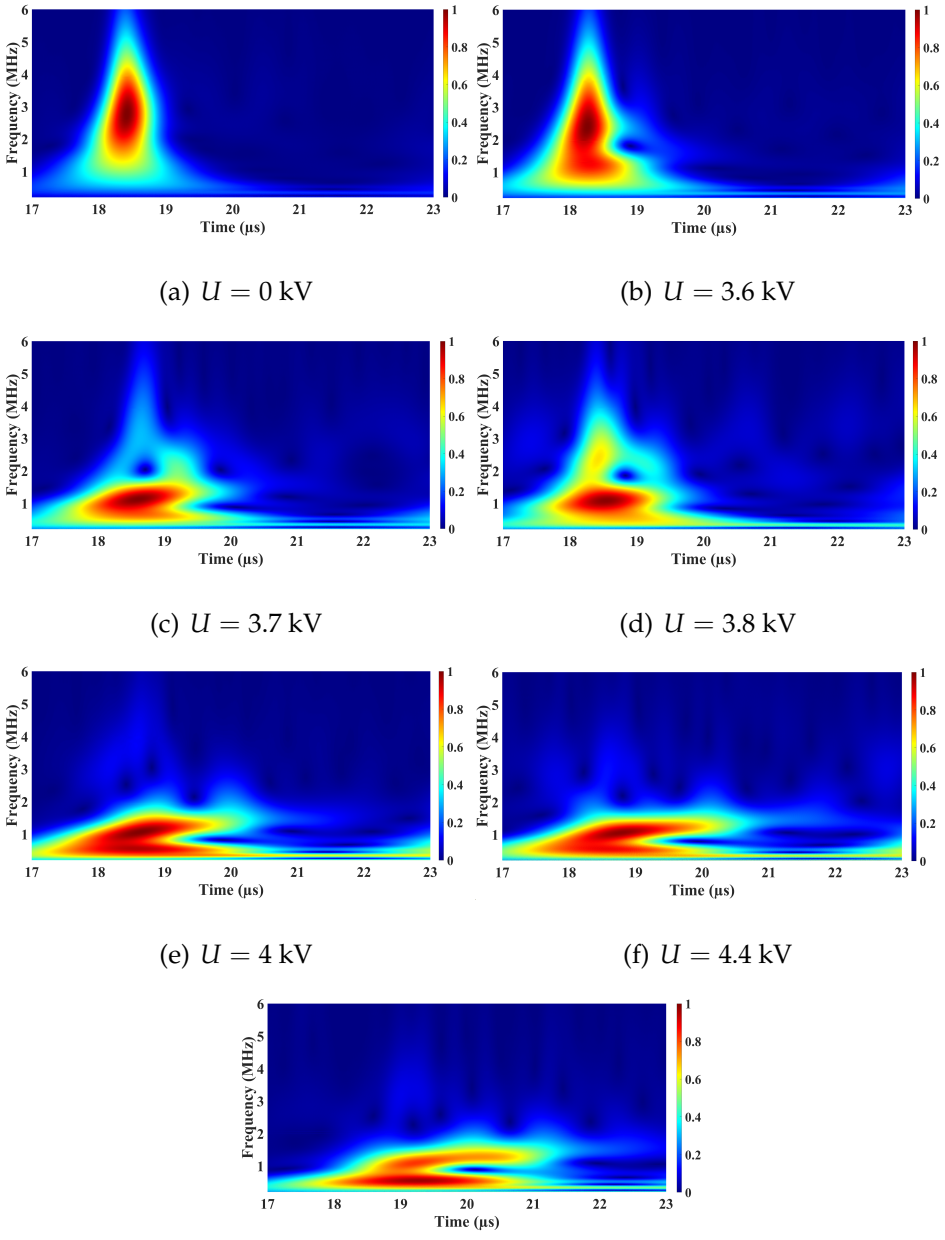

(a) $U = 0$ kV (b) $U = 3.6$ kV

(c) $U = 3.7$ kV (d) $U = 3.8$ kV

(e) $U = 4$ kV (f) $U = 4.4$ kV

(g) $U = 6.3$ kV

Figure IV.16: Continuous wavelet transform of SAW signals corresponding to each adhesion level.

Figure IV.16 illustrates the normalized spectral amplitude distribution as a function of the time arrival of the surface modes across adhesion levels, with color intensity indicating the spectral amplitude at any specific time. Regions of red color denote high signal amplitudes, while the yellow-blue colors represent weaker amplitudes.

The analysis shows that as the adhesion zone increases, there is a shift towards a lower frequency range over time. This pattern suggests that electro-adhesion influences multiple wave modes. Therefore, these modes reach the detection point at different arrival times. Conversely, at the initial adhesion level, the frequencies are detected simultaneously.

This first configuration experiment allows the detection of the changes in the dispersion of surface acoustic waves due to electro-adhesion. The subsequent section will further investigate these changes, presenting the dispersion curves from the second configuration experiment for each level of adhesion.

4.2 Influence of adhesion level on surface acoustic wave dispersion curves

To obtain the dispersion curves, the pulsed laser is directed at 251 distinct points, spaced by 60 μm, along the interface between the PVC layer and the substrate (thanks to the transparent PVC film), covering a total distance of 15 mm. Using the same signal processing method as in the FEM study, dispersion curves are presented in the wavenumber-frequency domain. Thus, the phase velocity value for each frequency is calculated by identifying the peak amplitudes of each wave mode and then a polynomial fitting is applied to plot the average value of the curves. The resulting dispersion curves are illustrated in figure IV.17.

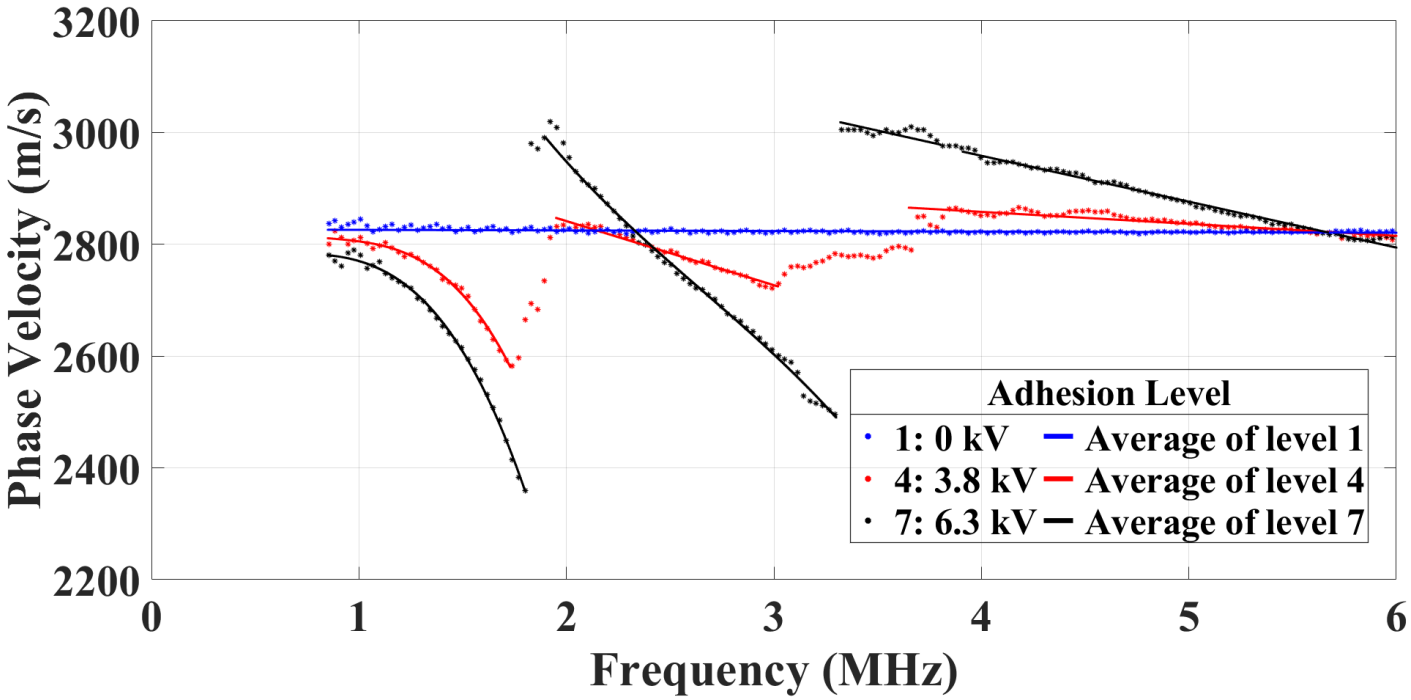

Figure IV.17: Influence of electro-adhesion level on the surface modes dispersion curves.

The curves in figure IV.17 confirm the predicted behavior of surface modes in the loading case according to the elastic properties of the PVC film and the aluminum substrate. At adhesion level 1, the surface acoustic wave exhibits a non-dispersive nature, as indicated by a constant value of the phase velocity as a function of frequency representing weak adhesion. By adhesion level 4, the surface modes appear, with shifting towards the strong contact condition seen at adhesion level 7, where the film is completely bonded to the substrate. These results confirm the influence of the progressive increase of PVC adhesion to the substrate with higher electric field intensity.

To solve the inverse problem by matching the theoretical and experimental results, a homogeneous adhesion strength at the interface should be considered, given that the theoretical model does not include changes in adhesion area characteristics. Therefore, the next section presents solving an inverse problem for adhesion level 7, where adhesion is considered uniform.

4.3 Evaluation of the uniform adhesion strength

In this section, the inverse problem is solved for adhesion level 7, where the film is fully adhered to the substrate, making it possible to consider a homogeneous case relative to perfect contact conditions discussed in the FEM models.

The dispersion curves are calculated at selected values of K_n and K_t to follow a suitable methodology. The method begins by setting a value for K_n and varying the value of K_t, based on the theoretical study of their impact in Chapter II on the dispersion curves.

The difference in phase velocity between the average curves of the experimental results and theoretical predictions is calculated for each mode, from which the Mean Absolute Error (MAE) can be computed at the resulting dispersion curves of the indicated K_n and K_t values. The curves obtained at the high-frequency range ($\geq$ 3.5 MHz) force the observation of modes 4, 5 and 6 for low K_t value. The average of the MAE is approximated for the 5 modes considered after calculating the error for each mode at certain values of K_n and K_t. The aim is to find the lowest average MAE of the five modes for a specific pair of K_n and K_t values, which can provide a practical estimation determining the strength of adhesion level 7.

As previously shown in Chapter II the modes are affected differently in studying the influence of K_n and K_t separately, making it challenging to find exact values of the normal and tangential stiffnesses when solving the inverse problem. However, this method is a good approach to study the adhesion strength of the interface and the values obtained will be then included in the FEM to approach the characterization of the non-uniform adhesion levels obtained in the experiment. Moreover, we also aim to find a slope of the modes that go along with the ones in the experiment.

Initially, and referring to the study of the influence of the adhesion parameters on the dispersion curves, K_n is fixed at 10^{14} N/m^3 and K_t is tested at three different levels: 10^{13} N/m^3, 5×10^{13} N/m^3 and 10^{14} N/m^3. Figure IV.18 displays the dispersion curves at these values. The mean absolute error is calculated by taking the ranges of frequencies at which the modes exist in both the experimental and the theoretical velocities.

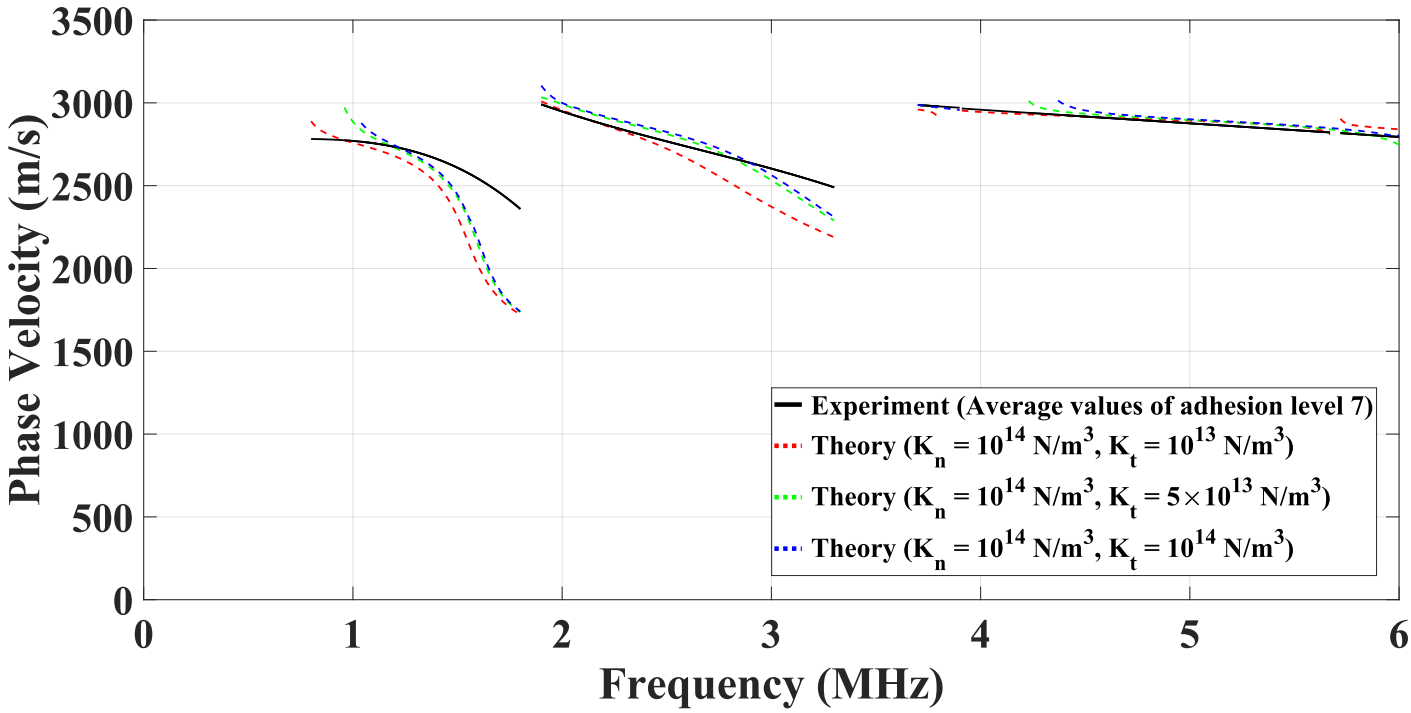

Figure IV.18: Dispersion curves for K_n fixed at 10^{14} N/m^3 and K_t varies at 10^{13} N/m^3, 5×10^{13} N/m^3 and 10^{14} N/m^3.

At $K_t = 10^{13}$ N/m^3 (red dashed curves) the results show a good slope alignment for the first and the second modes, then as K_t increases up to $K_t = 10^{14}$ N/m^3 (blue dashed curves) the curves are shifted to the higher frequency range of the experiments that do not fit well with the experimental one. This is also the case for the higher frequency modes at which $K_t = 10^{13}$ N/m^3 shows a better alignment with the frequency range of the experiment compared with the other values of K_t.

Table IV.3 summarizes the mean absolute error for this evaluation. The computations are approximated and the lowest average of the MAE is at $K_n = 10^{14}$ N/m^3 and $K_t = 10^{13}$ N/m^3. Next, this value of K_t is fixed and K_n will be studied to find an approximated average value of the MAE.

Mean absolute error (m/s) at $K_n = 10^{14}$ N/m^3			
Modes	$K_t = 10^{13}$ N/m^3	$K_t = 5 \times 10^{13}$ N/m^3	$K_t = 10^{14}$ N/m^3
mode 2	220	253	230
mode 3	112	59	61
mode 4	39	7	15
mode 5	13	36	45
mode 6	52	-	-
Average	87	89	88

Table IV.3: MAE for each mode at fixed $K_n = 10^{14}$ N/m^3 with their corresponding average value of each K_t case.

The results are not significantly different, and the lowest average MAE is found at $K_t = 10^{13}$ N/m^3 of 87 m/s which is then selected and fixed for the next analysis when K_n is varied at the values: 5×10^{14} N/m^3 and 5×10^{15} N/m^3. Table IV.4 summarizes the mean absolute error for this evaluation.

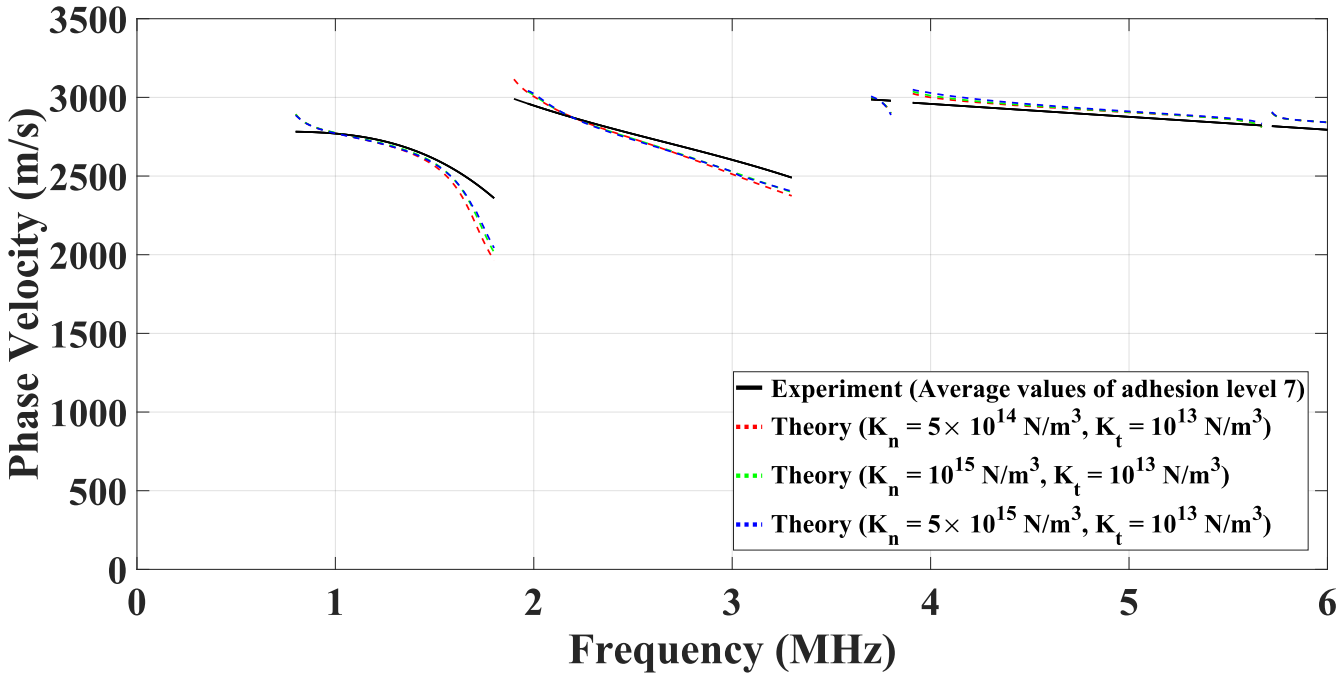

Figure IV.19: Dispersion curves for K_t fixed at 10^{13} N/m^3 and K_n varies at 5×10^{14} N/m^3, 10^{15} N/m^3 and 5×10^{15} N/m^3.

Figure IV.19 shows the dispersion curves for varying values of K_n with K_t fixed at 10^{13} N/m^3. The experimental data is represented by solid black lines, while theoretical predictions are indicated by dashed colored lines. At $K_n = 5 \times 10^{14}$ N/m^3 (red dashed curves), the slope alignment for the lower frequencies of the modes is reasonable, but deviations are observed at higher frequencies. Increasing K_n to 10^{15} N/m^3 (green dashed curves) shows an improved fit with the experimental data for both lower and higher modes, suggesting this value provides a more accurate representation of the experimental conditions. Moreover, at $K_n = 5 \times 10^{15}$ N/m^3 (blue dashed curves), the theoretical curves shift towards the experimental ones at higher frequencies of modes 2 and 3, but for the higher modes there is not significant shifting at these parameter variations.

Table IV.4 summarizes the mean absolute error (MAE) for each mode across different K_n values. The results indicate that the lowest average MAE is achieved at $K_n = 5 \times 10^{15}$ N/m^3 and $K_t = 10^{13}$ N/m^3, with an average MAE of 46 m/s. This pair of K_n and K_t provides the best alignment with the experimental data, as shown by the dispersion curves overlapping at the same frequency ranges of the modes and the MAE values. Therefore, $K_n = 5 \times 10^{15}$ N/m^3 and $K_t = 10^{13}$ N/m^3 are considered the optimal values for approximate modeling in this study.

Mean absolute error (m/s) at $K_t = 10^{13}$ N/m^3			
Modes	$K_n = 5 \times 10^{14}$ N/m^3	$K_n = 10^{15}$ N/m^3	$K_n = 5 \times 10^{15}$ N/m^3
mode 2	75	59	58
mode 3	57	54	52
mode 4	25	28	26
mode 5	29	39	40
mode 6	56	56	52
Average	48	47	46

Table IV.4: MAE for each mode at fixed $K_t = 10^{13}$ N/m^3 with the average value for each K_n case.

Figure IV.20 illustrates the theoretical dispersion curves at $K_n = 5 \times 10^{15}$ N/m^3 and $K_t = 10^{13}$ N/m^3.

This is necessary to compare the curves with the perfect contact condition.

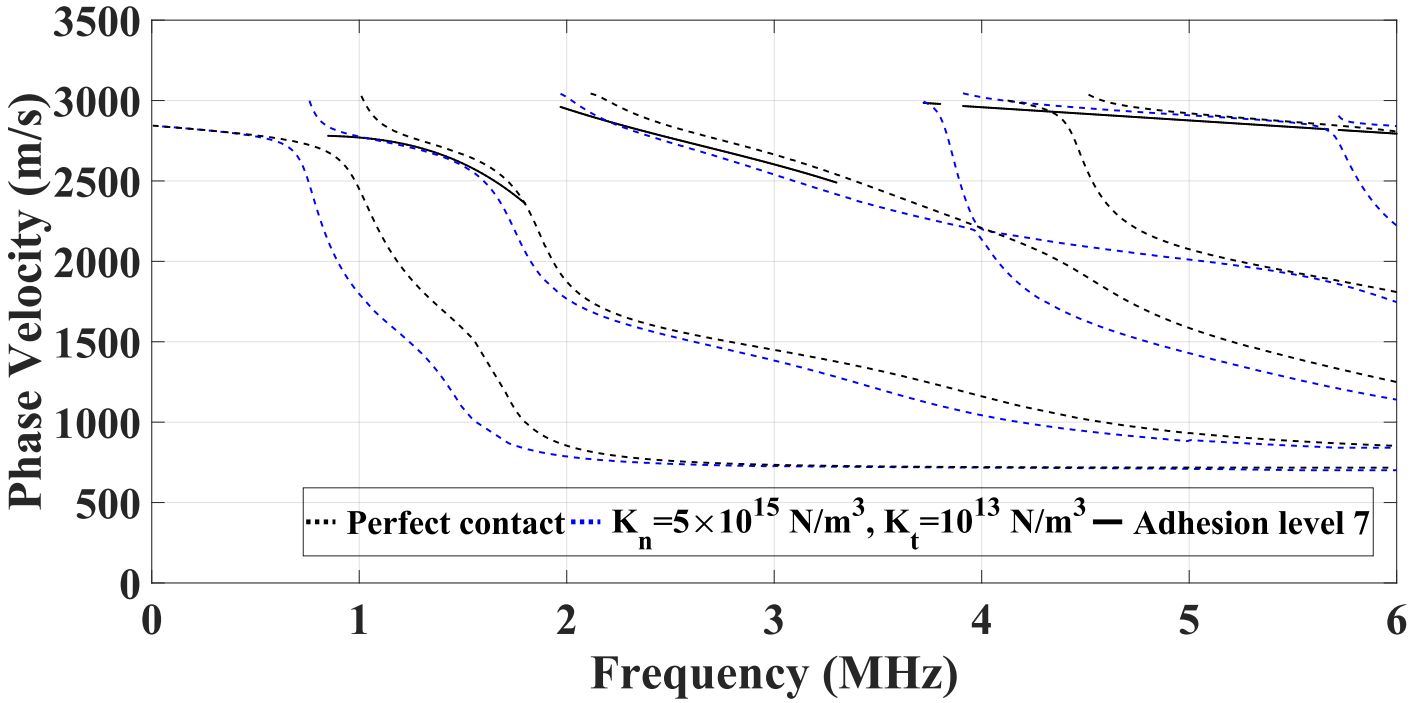

Figure IV.20: Dispersion curves at $K_n = 5 \times 10^{15}$ N/m^3 and $K_t = 10^{13}$ N/m^3, compared to the perfect contact condition with respect to adhesion level 7.

This comparison provides an analysis of the uniform adhesion strength (adhesion level 7), the experimental curves are close to the perfect contact condition. This value suggests that the experimental dispersion curves at adhesion level 7 correspond to a high adhesion strength, consistent with the theoretical analysis in Chapter II.

4.4 Finite Element Model of the interaction of surface acoustic waves with the non-uniform adhesion interface

Experimentally, we observe that the electro-adhesion effect pattern varies with different voltage levels and is non-uniform across the interface at levels 2, 3, 4, 5 and 6. This variability suggests that the EA effect does not distribute evenly, potentially due to uneven surfaces or varying electrical properties at different points of contact. To provide a deeper understanding of how this non-uniformity affects the system's behavior, we introduce a finite element model in this section. This model sim-

ulates the dispersion curves that represent the experimentally measured adhesion length d. The simulation aims to model the experimental conditions by varying the adhesion zone d according to the adhesion levels.

In the previous section, we solved an inverse problem with the parameters $K_n = 5 \times 10^{15}$ N/m^3 and $K_t = 10^{13}$ N/m^3. Referring to the dispersion curves analyzed in Chapter III, which examine the non-uniform adhesion interface, these K_n and K_t values are included to represent the perfect contact conditions for homogeneous adhesion. Consequently, the mechanical properties of the intermediate layer (Poisson's ratio and Young's modulus), should be equivalent to these K_n and K_t values.

Therefore from equation 3.1, $\nu_0 = 0.498$ and $E_0 = 2.997$ MPa. The following figures IV.21, IV.22, IV.23, IV.24, IV.25 display the dispersion curves of the simulations for each adhesion level.

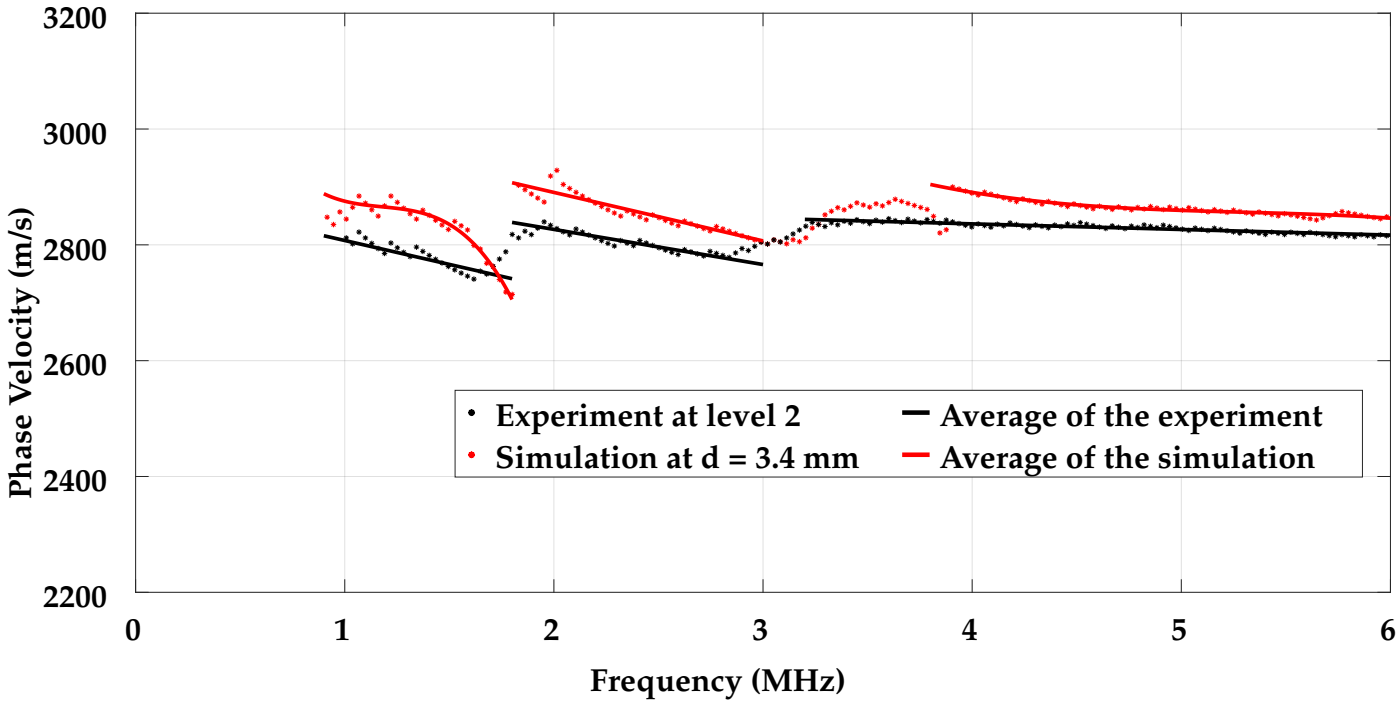

Figure IV.21: Simulated dispersion curves at $d = 3.4$ mm and the experimental dispersion curves of level 2.

Figure IV.21 compares simulated and experimental dispersion curves at $d = 3.4$ mm. In the low-frequency range (0-2 MHz) and in the mid-frequency range (2-3 MHz) the second and third Rayleigh modes for both the experimental and simulated results show a slight decrease in phase velocity.

In the high-frequency range (3-6 MHz), phase velocities for the fourth and fifth Rayleigh modes are almost constant in the experimental results which can be due to the filter used (4 MHz) for the interferometer. However, these modes remain comparable with the simulated modes, indicating a good representation of the SAW interaction with the structure in the model.

Additionally, the mean absolute error for each polynomial mode was evaluated. The results show that Mode 2 has a MAE of 61 m/s, mode 3 of 55 m/s, and mode 4 of 35 m/s with an average value of 50 m/s.

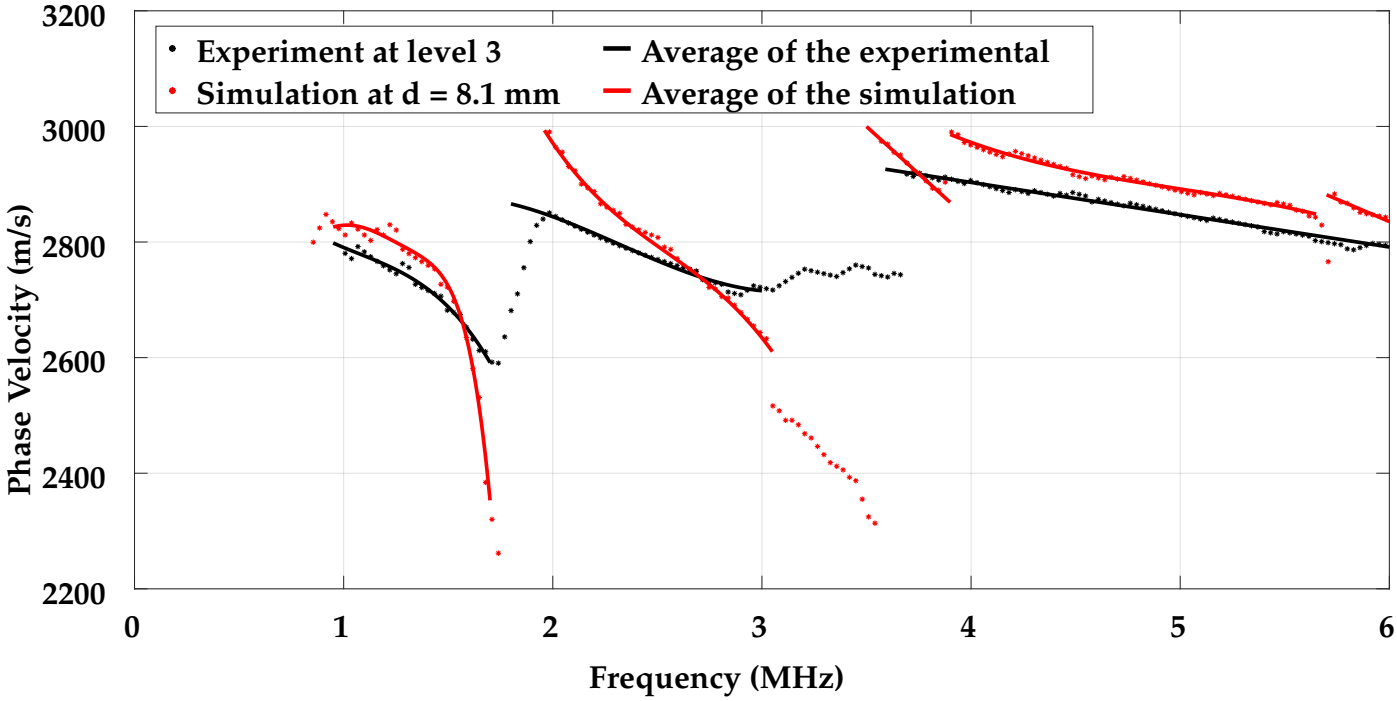

Figure IV.22: Simulated dispersion curves at $d = 8.1$ mm and the experimental dispersion curves of level 3.

Figure IV.22 presents the simulated and experimental dispersion curves at $d = 8.1$ mm. In the low-frequency range (0-2 MHz), the second Rayleigh mode shows a significant decrease in the phase velocity for both the experimental and simulated curves, indicative of loading case mode behavior. In the mid-frequency range (2-3 MHz), the experimental data displays a slight slope change in the phase velocity of the third Rayleigh mode in comparison with the previous results, while the simulated results show higher slope modification, possibly due to differences in boundary conditions. In the high-frequency range (3-6 MHz), the simulated curves obtained for the fourth and fifth Rayleigh

modes are separated from the previous result. Although the experimental phase velocities remain almost constant, the slope of the curve shows a decrease in the phase velocities as a function of frequency that is comparable to the modes in the simulation.

The mean absolute error (MAE) for each mode was also evaluated. The results show that Mode 2 has a MAE of 52 m/s, mode 3 of 42 m/s, mode 4 of 50 m/s and mode 5 of 59 m/s with an average value of 51 m/s.

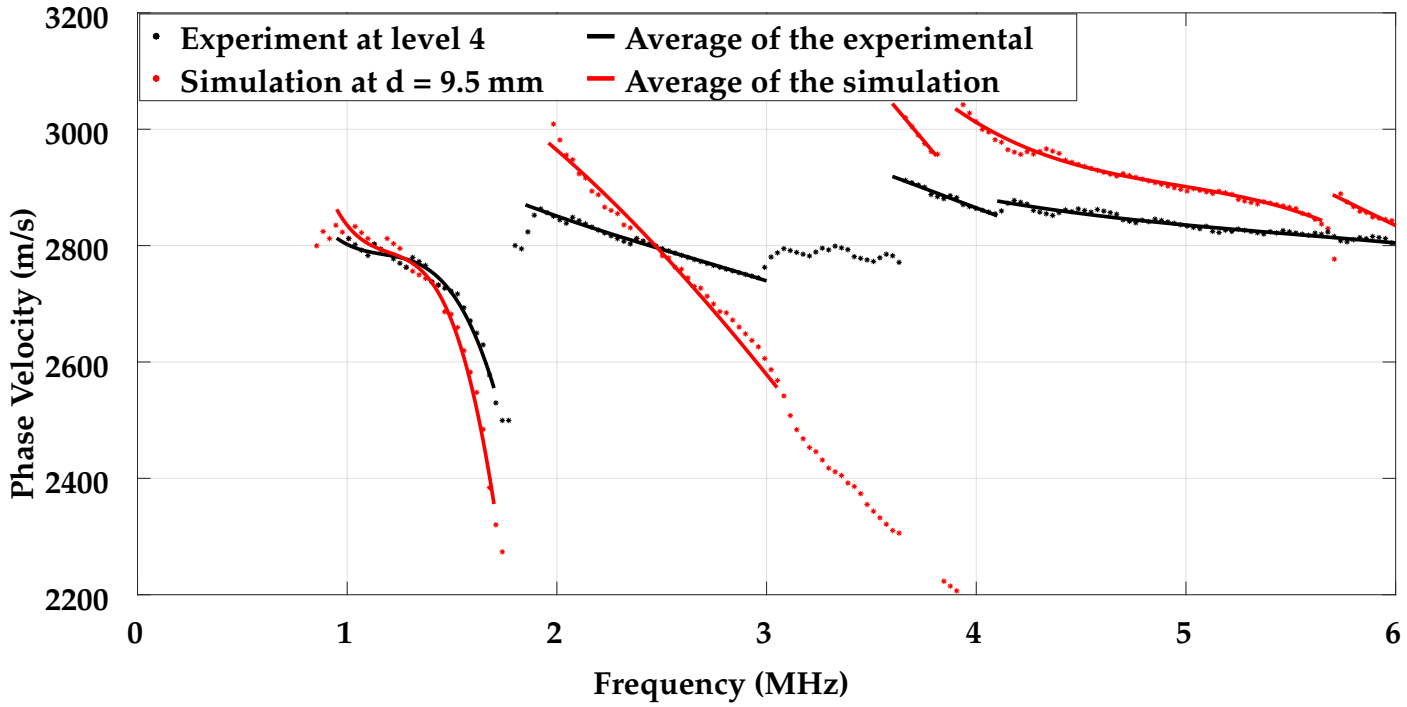

Figure IV.23: Simulated dispersion curves at $d = 9.5$ mm and the experimental dispersion curves of level 4.

Figure IV.23 shows the simulated and experimental dispersion curves at $d = 9.5$ mm. In the low-frequency range (0-2 MHz), the second Rayleigh mode simulated well illustrates the experimental one. The mid-frequency range (2-3 MHz) shows a modification in the third Rayleigh mode phase velocity for both the experimental and simulated results with respect to the previous curves. In the high-frequency range (3-6 MHz), the simulation displays a higher influence of the adhesion area on the fourth and fifth Rayleigh modes. On the other hand, the experimental curves demonstrate stabilization of phase velocity with lower influence.

The mean absolute error (MAE) for each mode was also evaluated. The results show that Mode 2

has a MAE of 42 m/s, mode 3 of 75 m/s, mode 4 of 39 m/s and mode 5 of 25 m/s with an average value of 45 m/s.

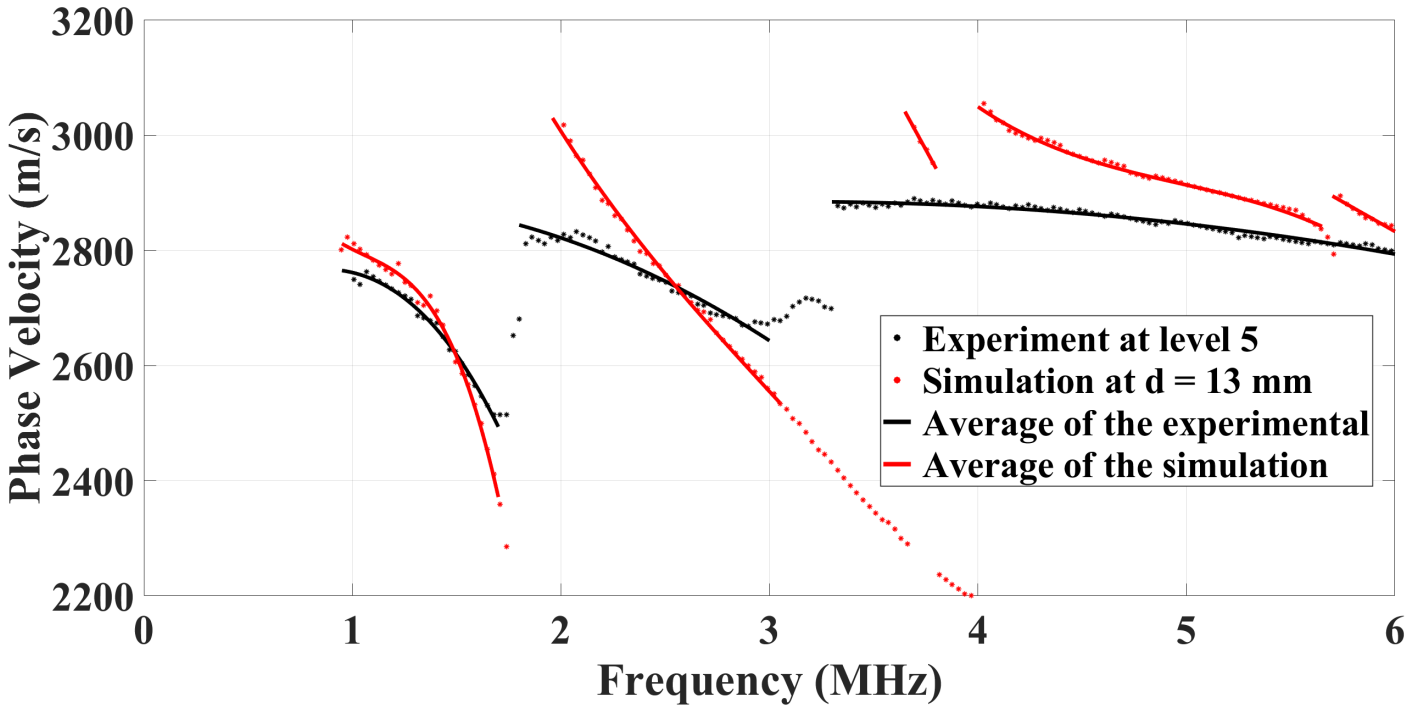

Figure IV.24: Simulated dispersion curves at $d = 13$ mm and the experimental dispersion curves of level 5.

Figure IV.24 shows the simulated and experimental dispersion curves at $d = 13$ mm. In the low-frequency range (0-2 MHz), the second Rayleigh mode from the simulation demonstrates the experimental observations. The mid and high-frequency range (2-6 MHz) displays a similar influence to the previous one in the third, fourth and fifth Rayleigh modes for both the experimental and simulated data.

The mean absolute error for each mode was also evaluated. The results show that Mode 2 has a MAE of 37 m/s, mode 3 of 57 m/s, mode 4 of 84 m/s and mode 5 of 61 m/s with an average value of 60 m/s.

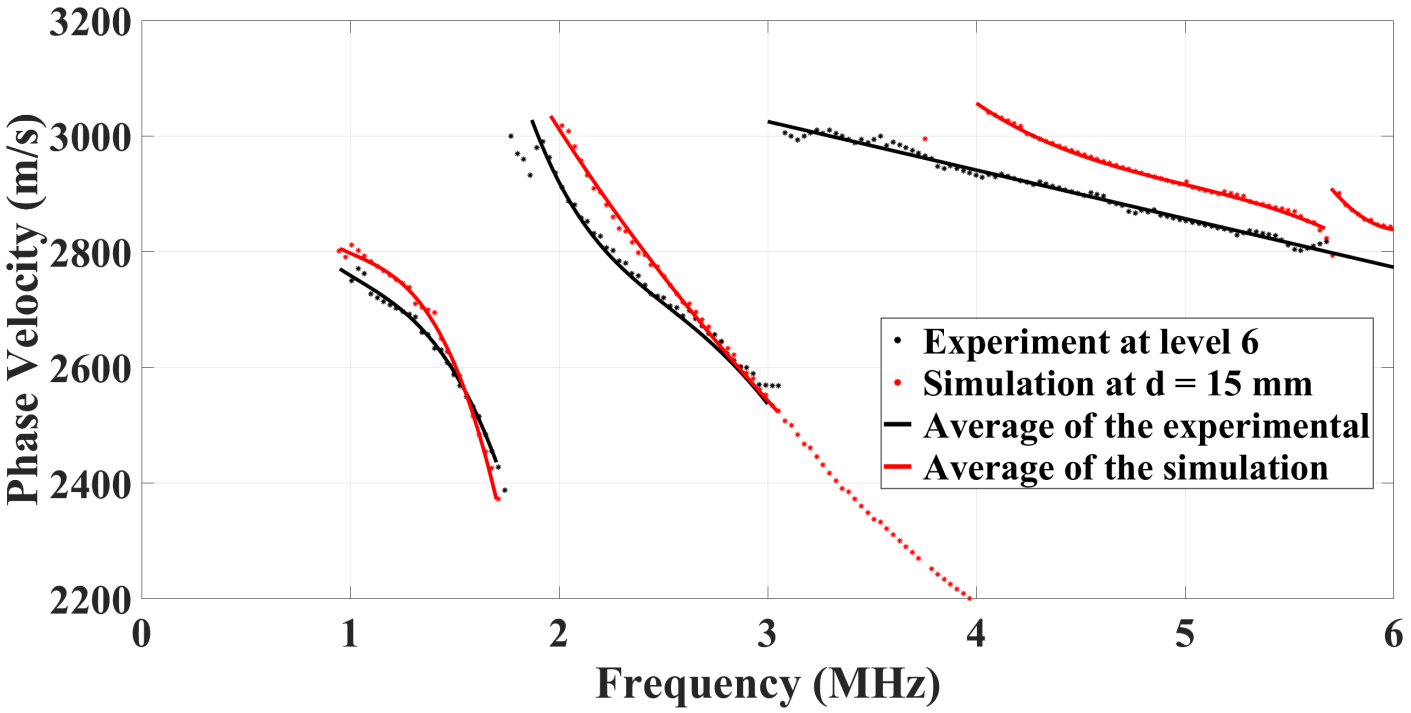

Figure IV.25: Simulated dispersion curves at $d = 15$ mm and the experimental dispersion curves of level 6.

Figure IV.25 displays the simulated and experimental dispersion curves at $d = 15$ mm. In the low-frequency range (0-2 MHz), the second Rayleigh mode in the simulation closely aligns with the experimental curve. The mid-frequency range (2-3 MHz) shows significant changes in the third Rayleigh mode for the experimental curve and is well demonstrated in the third Rayleigh mode obtained in the simulation. In the high-frequency range (3-6 MHz), the simulated data indicates a significant influence of the adhesion area on the fourth and fifth Rayleigh modes, while the experimental data shows consistency of phase velocity in these modes, however, the influence of the adhesion area on these modes are still observed by the loading case dispersion behavior of the surface modes.

The mean absolute error for each mode was also evaluated. The results show that Mode 2 has a MAE of 35 m/s, mode 3 of 28 m/s, mode 4 of 38 m/s and mode 5 of 80 m/s with an average value of 45 m/s.

As mentioned in Chapter III, the first mode shows low resolution, hence the curves are presented starting with the second mode. The results of mode 2 show coherence with the simulation with

a slight error that could be due to the approximation made for solving the inverse problem in the previous section and the error in selecting the value of d. However, mode 3 is coherent for levels 2 and 6 while for levels 3, 4 and 5, the mode arrives in the same interval of frequency, but it has a different slope.

The dispersion curves in the simulation started by showing the influence of weak non-uniform adhesion influence (average adhesion strength at $d = 3.4$ mm) and by increasing the adhesion area towards ($d = 15$ mm) the dispersion curves show convergence towards the curves of the case of the $K_n = 5 \times 10^{15}$ N/m^3, $K_t = 10^{13}$ N/m^3, $\nu_0 = 0.498$ and $E_0 = 2.997$ MPa in the uniform case. The general behavior of SAW propagation of the loading case is well obtained in both the experimental and simulated results. The results indicated high sensitivity of the second and third modes to the adhesion quality in the experiment. However, for the fourth and fifth modes, the sensitivity is observed in the simulation, but due to some experimental limitations, this sensitivity is weakly observed although it is still comparable to the simulation.

This study performed the inverse problem solution through both theoretical (numerical) calculations and the finite element method. The numerical calculations focused on a uniform adhesion interface, while the FEM not only simulated the effect of the uniform adhesion case but also effectively demonstrated what could be detected and observed experimentally. Moreover, the FEM allowed us to simulate the influence of non-uniform adhesion on the propagation and dispersion of surface acoustic waves in a layered structure.

Conclusion

In this chapter, we introduced the principles of electro-adhesion and the use of a non-contact EA pad to achieve varied levels of adhesion. These levels were in the form of a non-uniform adhesion strength at the interface, enabling the observation of adhesion patterns for different voltages.

Two investigation methods were included considering Laser-Ultrasonics each with a specific aim, the first is to analyze the frequency distribution of the signals through the interface and the second is to extract the dispersion curves for each adhesion level.

The detected signals showed that when the adhesion area increases the signal has a larger wavelength, hence the frequency spectrum shifts towards lower frequency. These results were coherent with the simulated signals in the study of non-uniform adhesion quality where the continuous wavelet transform analysis is investigated.

At adhesion level 7, a homogeneous pattern was considered at the interface, therefore the inverse problem was solved for this level to obtain values of stiffnesses $K_n = 5 \times 10^{15}$ N/m^3 and $K_t = 10^{13}$ N/m^3. These parameters were then included in the finite element simulations to model the experimental adhesion levels for the non-uniform adhesion. The measured adhesion distance is then simulated and the dispersion curves were obtained for each level. The results showed coherence with the modes at the frequency intervals as well as the average value of the mean absolute error.

Bibliography of Chapter IV

[1] Pandey Rajagopalan et al. "Advancement of Electroadhesion Technology for Intelligent and Self-Reliant Robotic Applications". In: *Advanced Intelligent Systems* 4.7 (2022), p. 2200064.

[2] Leah K Borden, Ankit Gargava, and Srinivasa R Raghavan. "Reversible electroadhesion of hydrogels to animal tissues for suture-less repair of cuts or tears". In: *Nature Communications* 12.1 (2021), p. 4419.

[3] Vito Cacucciolo, Herbert Shea, and Giuseppe Carbone. "Peeling in electroadhesion soft grippers". In: *Extreme Mechanics Letters* 50 (2022), p. 101529.

[4] Jianglong Guo et al. "Optimization and experimental verification of coplanar interdigital electroadhesives". In: *Journal of Physics D: Applied Physics* 49.41 (2016), p. 415304.

[5] Wei Liu, Xinfeng Tang, and Jeff Sharp. "Low-temperature solid state reaction synthesis and thermoelectric properties of high-performance and low-cost Sb-doped Mg2Si0. 6Sn0. 4". In: *Journal of Physics D: Applied Physics* 43.8 (2010), p. 085406.

[6] Jianglong Guo, Jinsong Leng, and Jonathan Rossiter. "Electroadhesion technologies for robotics: A comprehensive review". In: *IEEE Transactions on Robotics* 36.2 (2019), pp. 313–327.

[7] AA Bahgat, SM Sayyah, and HS Shalabi. "Electrical Properties of Pure PVC". In: *Science and Technology of Polymers and Advanced Materials: Emerging Technologies and Business Opportunities* (1998), pp. 421–428.

[8] Sylvain Schaller and Herbert Shea. "Measuring electro-adhesion pressure before and after contact". In: *Scientific Reports* 13.1 (2023), p. 11768.

[9] KL Mittal. "Adhesion aspects of metallization of organic polymer surfaces". In: *Journal of vacuum science and technology* 13.1 (1976), pp. 19–25.

[10] Frank W DelRio et al. "The role of van der Waals forces in adhesion of micromachined surfaces". In: *Nature materials* 4.8 (2005), pp. 629–634.

General Conclusion

In conclusion, we have introduced the importance of studying the properties of thin films, focusing on the adhesion quality and surface acoustic wave sensitivity to the elastic parameters in a layered structure. We have used Laser-Ultrasonics as a non-contact, non-destructive testing technique to investigate an electro-adhesion effect on surface acoustic waves.

In Chapter I, we provided an overview of different deposition techniques and their advantages. Additionally, we outlined the theories of adhesion and its characterization using both destructive and non-destructive testing methods, focusing on electro-adhesion as a novel method to control interface quality using an electric field generator. The principles of the mechanism of Laser-Ultrasonics in thermoelastic and ablation regimes, as well as the interferometry mechanism used in the experiments, were then discussed. Finally, the measured elastic parameters of the materials used experimentally were presented.

Although electro-adhesion has been used in many applications with pads of plate electrodes, the thickness of these electrodes makes it challenging to characterize adhesion using acoustic waves due to their sensitivity to the thickness of the layered material. Additionally, the elastic properties of these plates affect the propagation of the surface acoustic waves. Therefore, we used a non-contact EA device that can modify the adhesion quality without any mechanical contact with the structure.

In Chapter II, the theoretical multi-layered model explained the derivation of the surface modes dispersion relation. This model relates the elastic parameters of the materials of a thin film perfectly adhered to a substrate to surface modes dispersion curves in three cases: loading, stiffening and intermediate. These cases predict the behavior of the generated surface waves according to the pa-

rameters of PVC and aluminum. Indeed the experimentally obtained dispersion curves showed a loading case as expected in the model.

The theoretical adhesion parameters K_n and K_t were also considered in previous studies. These parameters are important in characterizing the adhesion strength by fitting the experimental dispersion curves with the theoretical ones as an inverse problem. Additionally, studying the evolution of the dispersion curves with respect to the variation of these parameters clarifies the experimental results.

In Chapter III, a finite element method was included to simulate the interaction between the surface waves with a PVC layered adhered to aluminum substrate in uniform and non-uniform adhesion cases as the mathematical model only considers a uniform adhesion strength. However not all the levels obtained experimentally were considered uniform. These models were important in both cases to study the influence of K_n and K_t parameters in the uniform case and the influence of the adhesion area by varying the adhesion distance.

In Chapter IV, the results of the EA device demonstrated the influence of electro-adhesion achieved through the use of sharp tip electrodes that create a potential difference with the conductor aluminum substrate to generate adhesion levels. Moreover, we have presented the challenges of including this device along with the lasers in the experimental setup. This setup was explained with an Nd:YAG pulsed laser doubled in frequency used for generating acoustic waves and a Mach-Zehnder heterodyne interferometer for detecting the normal displacements of the surface wave.

Seven adhesion levels were obtained with well-observed patterns under an image acquisition device. These levels were considered non-uniform adhesion depending on the zones affected by the electric field. However, adhesion level 7 (the highest level) was identified as uniform due to the presence of the entire film in the range of the effective electric field.

The experimental methodologies are divided into two configurations. In the first one, surface waves were generated and detected on the substrate allowing their propagation through the entire film and showing the impact of the adhesion quality on a single Rayleigh wave. In the second one, the generation of the surface waves is localized at the interface of the sample, providing acquisi-

tions with signal processing methods to obtain the dispersion curves of the surface modes. These configurations were well clarified in the thesis.

The estimated values of K_n and K_t solved by the inverse problem on adhesion level 7 were included and fixed in the simulation, thus the adhesion length was varied according to the measured ones. Finally, these simulations validated the interactions obtained experimentally for each adhesion pattern using the dispersion curves.

Overall, we successfully reached the aim of this work by applying the Laser-Ultrasonics method as a non-destructive testing technique to characterize a new method of inducing adhesion levels by an electric field source. This method generated levels of adhesion of a non-uniform pattern. Therefore, models and numerical methods were calculated and developed to analyze the impact of adhesion on acoustic wave propagation. The use of the finite element model was important in simulating the interaction of surface acoustic waves with thin film interfaces, providing an understanding of how variations in adhesion area affect wave dispersion.

This work opens future research studies for the characterization of the adhesion strength/area using specific parameters depending on the adhesion theory (diffusion, mechanical interlocking, chemical reactions). Moreover, the optimization of controlling the non-contact electro-adhesion using the non destructive testing methods to detect defects and interactions of other materials.

Moreover, a multiphysics modeling problem would be interesting in modeling the generation of the adhesion levels from an electric field source and their influence on surface acoustic waves in a three-dimensional model.

Abstract

This thesis focuses on material adhesion, which is often crucial to the reliability of coating technologies. More precisely, the adhesion quality of a polyvinyl chloride film to an aluminum substrate is evaluated by Laser-Ultrasonics. Indeed, this non-contact and non-destructive method allows to excite surface acoustic waves (SAW) in layer-on-substrate structures, whose propagation can be sensitive to adhesion. Experimentally, these guided waves are excited by a frequency-doubled Nd:YAG laser and detected via a Mach-Zehnder heterodyne interferometer.

To avoid coating thickness variations that would interfere with acoustic wave propagation, It is preferable not to consider an intermediate adhesive layer. Therefore, for the first time, we are using an electro-adhesion device that allows the adhesion level of the dielectric layer to the substrate to be modified by simple voltage adjustments.

A program has been developed to obtain the Rayleigh modes dispersion curves considering the effect of normal and tangential stiffnesses. In addition, finite element method is implemented to simulate SAW propagation under varied adhesion conditions. The results clearly show the sensitivity of these waves to electrostatically induced variations in the quality of film adhesion only.

Keywords: Laser-Ultrasonics, Surface Acoustic Waves, Rayleigh modes, Electro-Adhesion, Non Destructive Testing, Finite Element Modeling.

Résumé

Cette thèse porte sur l'adhésion des matériaux qui est souvent cruciale pour la fiabilité des technologies associées aux revêtements. Plus précisément, la qualité de l'adhésion d'un film en chlorure de polyvinyle à un substrat d'aluminium est évaluée par Ultrasons-Laser. En effet, cette méthode sans contact et non destructive permet d'exciter des ondes acoustiques de surface (SAW) dans les structures du type couche sur substrat dont la propagation peut être sensible à l'adhésion. Expérimentalement, ces ondes guidées sont excitées par un laser Nd:YAG doublé en fréquence et détectées par un interféromètre hétérodyne de type Mach-Zehnder.

Pour éviter des variations d'épaisseur du revêtement qui interféreraient avec la propagation des ondes acoustiques, il apparaît préférable de ne pas utiliser de couche adhésive intermédiaire. C'est pourquoi nous utilisons pour la première fois un dispositif d'électro-adhésion permettant de modifier le niveau d'adhérence de la couche diélectrique au substrat par de simples ajustements de tension.

Un programme a été développé afin d'obtenir les courbes de dispersion des modes de Rayleigh en tenant compte de l'effet des rigidités normales et tangentielles. En outre, la méthode des éléments finis est mise en œuvre pour simuler la propagation des SAW dans des conditions d'adhérence variées. Les résultats montrent clairement la sensibilité de ces ondes aux seules variations de la qualité d'adhérence du film induites électrostatiquement.

Mots-clés: Ultrasons-Laser, Ondes Acoustiques de Surface, Modes de Rayleigh, Electro-Adhésion, Contrôle Non Destructif, Modélisation par éléments finis.